Part III:
Impact of harmonic inflow oscillations and active actuation

This page is intentionally left blank

Chapter 6

Impact of harmonic inflow oscillations on the size and dynamics of the separated flow over a bump

Part of this section has been published in Marbona, Rodríguez, Martínez-Cava, and Valero (2024). Impact of harmonic inflow variations on the size and dynamics of the separated flow over a bump. Phys. Rev. Fluids, 9, 053901.

In a multi-stage turbine configuration, the flow dynamics on the suction side of low-pressure turbine (LPT) blades are further complicated by the inherent unsteadiness. This is due to the periodic passage of wakes shed by upstream blade stages, which disturb the flow conditions in downstream passages. These disturbances trigger the formation of strong vortical structures that pull fluid from the downstream recirculation region, temporarily reducing the extent of flow separation. Over time, the separation bubble regenerates and grows until it stabilizes or is again influenced by the next incoming wake. As a result, the transition to turbulence is driven by a combination of periodic free-stream flow fluctuations and the inherent instabilities within the separated flow (Hodson and Howell, 2005).

Wake-induced transition is highly sensitive to the combined effects of the adverse pressure gradient, as well as the intensity, temporal variability, and frequency of inflow free-stream fluctuations. Numerous studies have explored how the wake-passing period influences the length of the separated flow region. These studies have modeled the periodic wake passage either as a localized inlet velocity deficit in both space and time (Coull and Hodson, 2011; Gungor et al., 2012; Karaca and Gungor, 2016; Volino, 2012) or as a harmonic variation in the cross-sectional inlet conditions (Lou and Hourmouziadis, 2000; Wissink and Rodi, 2003; Wissink, 2006). Despite differences between the two modeling approaches, their results are qualitatively consistent regarding the effects of wake-passing frequency and intensity on the flow.

A dimensionless frequency F, commonly referred to as the reduced frequency, is defined using the characteristic free-stream velocity U and a streamwise length L. It is expressed as a representative of the extent of the adverse pressure gradient region in the absence of wakes

at which $F = f_{in}L/U$, where f_{in} is the dimensional wake-passing frequency. The reduced frequency represents the ratio of the convective time scale to the period of the imposed free-stream variations. Ambiguity arises in the practical characterization of F: First, the length of the steady-flow separated region depends on the specific problem and is typically determined *a posteriori*. Alternatively, other definitions of L are commonly used in the literature, such as the length of the low-pressure turbine (LPT) blade or flat plate employed in experiments (e.g. Coull and Hodson (2011), Lou and Hourmouziadis (2000), and Wissink (2006)), as these can be measured more precisely. Second, under unsteady inflow conditions, both the free-stream velocity and the streamwise pressure gradients vary continuously, often deviating significantly from their steady-flow counterparts. Due to these uncertainties, the focus in discussions of the physics is often on the order of magnitude of F rather than its precise value.

Wake-passing reduced frequencies F close to but slightly lower than 1 are representative of aero-engine LPTs (Coull and Hodson, 2011). For low F, the wake passing period is long compared with the characteristic times of both the KH-related vortex shedding and the regeneration of the separation bubble; the impact on the time-average separated flow and aerodynamic performance is expected to be comparatively weak. For F above 1, successive wakes pass by the separated flow region before the separation bubble has time to fully regenerate, which leads to significantly shorter time-averaged bubbles. These observations agree with investigations on active flow control of separated flows by means of periodic excitation using wall suction and blowing or geometries with moving parts, reviewed by Greenblatt and Wygnanski (2000), which conclude that the forcing frequency that minimises the size of the separated flow is $F \sim 1$. Interestingly, this frequency is typically lower than that of the KH instability and scales with the global length of the separated flow rather than with the local properties of the separated boundary layer.

The chapter studies the separated flow formed over a wall-mounted bump geometry that reproduces some characteristics of the suction side of a LPT blade under periodic fluctuations of the inflow stream. Similar geometries have been employed in the past both experimentally and numerically to study the fundamental physics of separated flow and possible means for flow control (Bernard et al., 2003; Marquillie and Ehrenstein, 2003; Passaggia et al., 2012; Pescini et al., 2017; Saavedra and Paniagua, 2018, 2021; Seifert and Pack, 2002). Direct numerical simulations are performed for ten different inflow conditions. The first case is the steady inflow in Chapter 3.1.

The other cases study different scenarios of wake-induced transition. The large-scale action of passing wakes is modeled as a harmonic fluctuation of inflow conditions (total pressure and bulk velocity) in a manner analogous to references (Lou and Hourmouziadis, 2000; Wissink and Rodi, 2003; Wissink, 2006). Lou and Hourmouziadis (2000) present results for a single value of the reduced frequency lying in the limit $F \ll 1$. Wissink and Rodi (2003) considers four cases with $F \sim 1 - 6$ and oscillations of the inflow velocity up to 20% of the mean value. Although the four cases simulated by Wissink and Rodi (2003) and Wissink (2006) qualitatively recover the same flow dynamics, they are clearly different from those in the experiments of Lou and Hourmouziadis (2000), emphasizing the existence of different dynamical scenarios depending on F and possibly on the amplitude of the harmonic inflow oscillations. The main objective

of the present work is to unveil and fully characterize the possible physical scenarios and their impact on the size of the separated flow. To cover the parametric space, a matrix of nine cases is defined with three frequencies and three fluctuation amplitudes. Here, three different scenarios are expected to be identified.

The remainder of the chapter is organized as follows. Section 6.1 describes the harmonic inflow boundary conditions with other setups as in Chapter 3.1. Section 6.2 presents and discusses the results. A qualitative description of the flowfield evolution and mean flow properties are given in Sections 6.2.1 and 6.2.2. The triple decomposition proposed by Hussain and Reynolds (1970) is applied to separate flow components that are coherent (in-phase) with the inflow oscillation from those occurring randomly. Section 6.2.3 describes the phase-averaged fields for three representative cases. The phase-averaged data provides information on the impact of the inflow oscillation over the length of the separated flow and how it evolves over the inflow period, which is discussed in Section 6.3. Section 6.4 presents the flow component that is incoherent (i.e. uncorrelated) with the inflow oscillation. Monitoring this component sheds light on the vortex dynamics that ultimately govern the behaviour of the separated flow. Section 6.5 presents frequency spectra at different probe locations. Section 6.6 provides a mode decomposition analysis of the weakest, intermediate, and strongest inflow oscillations using the OVMD technique. In combination, these analyses show that the separated flow subject to inflow oscillations can present three different scenarios regarding the flow dynamics and their impact on the length of the separated flow region. These scenarios are thus fully characterized in Section 6.7 and discussed in Section 6.7, along with their connection with active flow control strategies.

6.1 Harmonic inflow boundary condition and setup

The details computational mesh and boundary conditions are as in Sections 3.1.1 and 3.1.2 of Chapter 3. In the *harmonic inflow* cases, a periodic variation of the total pressure at the inlet is imposed, while the total temperature remains constant as in the steady inflow case. The total pressure at the inlet is defined as

$$p_t\left(t^*\right) = p_{t,steady}\ \left(1 + A_{in}\ \sin(2\pi f^*_{in}(t^* - t^*_0))\right) \tag{6.1}$$

where $p_{t,steady}$ is the total pressure of the steady inflow case ($p_{t,steady} = 105,319$ Pa), A_{in} is the amplitude of the harmonic oscillation, f^*_{in} is a dimensionless frequency, t^* is a dimensionless time and t^*_0 is a reference instant. Dimensionless velocity, time, and frequency are as defined in Chapter 3.

Note that the definition of f^* is not the same as the reduced frequency F discussed earlier. The definition of F is based on the representative length of the separated flow region, which is not known *a priori*. In addition, the specification of f^* based on the unit length simplifies data temporal sampling and subsequent analyzes. Nine cases with harmonic inflow variation are considered, comprising three amplitudes ($A_{in} = 0.01, 0.05$ and 0.1) and three different frequencies ($f^*_{in} = 0.5, 1$ and 2).

6.2 Instantaneous, mean, and phase-averaged flow field results

Table 6.1 summarizes the different simulations performed in this work, comprising the reference case that features a steady inflow and nine cases in which the inflow has a harmonic component of different frequency f^*_{in} and amplitude A_{in}. All the harmonic inflow cases use the same timestep $\Delta t^* = 2 \times 10^{-5}$. The initial transient, different for each case but comprising several flow-through times, was discarded and the following simulation sampling time $t^*_{data} = 50$ was collected for the subsequent analysis.

Table 6.1: Summary of the cases simulated, including the definition of the inlet pressure condition, the characterization of time-averaged and phase-dependent values of the reference streamwise velocity, and the length of the recirculation region L_s.

Δt^*	CFL_{max}	t^*_{data}	A_{in}	f^*_{in}	$\bar{u}^*_{@Ref}$	$\Delta u^*_{@Ref}$	L_s [m]	ΔL_s [m]
3×10^{-5}	0.9	72.3	-	-	1.11	-	0.2782	-
2×10^{-5}	0.7	50	0.01	0.5	1.1025	0.0293	0.2782	0
	0.7	50	0.01	1	1.1078	0.0301	0.2780	-0.0002
	0.7	50	0.01	2	1.1072	0.0282	0.2625	-0.0157
	0.7	50	0.05	0.5	1.1030	0.1467	0.2727	-0.0055
	0.7	50	0.05	1	1.1022	0.1467	0.2600	-0.0182
	0.7	50	0.05	2	1.1008	0.1401	0.1966	-0.0816
	0.8	50	0.1	0.5	1.0872	0.2929	0.2575	-0.0207
	0.8	50	0.1	1	1.0840	0.2961	0.2323	-0.0459
	0.8	50	0.1	2	1.0871	0.2772	0.1536	-0.1246

The harmonic change of the inlet total pressure leads to a periodic acceleration and deceleration of the bulk flow. Due to the relatively long upstream extension of the domain, the inflow changes reach the bump with a delay. A reference point located just upstream of the bump (see Fig. 3.9 and Table 3.3) is used to characterize the changes in bulk flow in the bump region. Figure 6.1 shows the total pressure and the evolution of the streamwise velocity at the reference point for case $A_{in} = 0.1$, $f^*_{in} = 2$. The total pressure at this point is used to define the phase of oscillation ϕ in the analysis performed in the rest of the paper. The phase $\phi = 0°$ is chosen as the time in which the total pressure is at its mean value and has maximum positive derivative (i.e. maximum acceleration); $\phi = 90°$ and $270°$ correspond respectively to the maximum and minimum values of the total pressure.

The streamwise velocity also exhibits a sinusoidal behaviour, with the mean value u_{mean} remaining the same as for the steady inflow case. A small delay T^*_d exists between the maxima and minima of total pressure and streamwise velocity, stemming from flow inertia. Table 6.1 shows the normalized amplitude of the streamwise velocity fluctuation, $\Delta u^* = (u_{max} - u_{min})/(2U_{Ref})$. This value is linearly proportional to A_{in} and the normalized streamwise

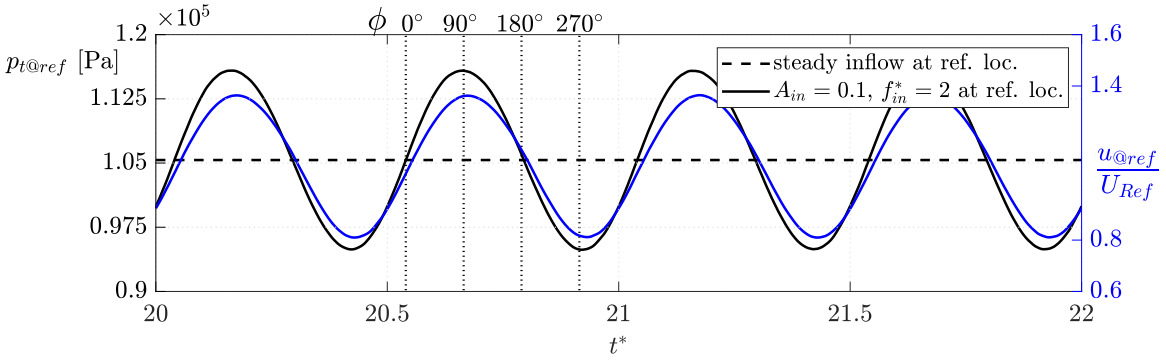

Figure 6.1: Evolution of total pressure and streamwise velocity at the reference point.

velocity at the reference point can be approximated by

$$u^*(t) \approx \bar{u}^* + \Delta u^* \sin(2\pi f^*_{in}(t^* + T^*_d)). \tag{6.2}$$

Table 6.1 also shows the mean value of the streamwise length of the flow recirculation region L_s, and its relative change with respect to the steady inflow case, $\Delta L_s = L_s - L_{s,steady}$ for each one of the cases with harmonic oscillation inflow. As opposed to Δu^*, ΔL_s is not proportional to A_{in}, indicating that essentially non-linear dynamics govern the separated flow and its reattachment. The non-linearity is associated with the complex vortex dynamics originated in the separated flow region and the impact of the flow acceleration and deceleration upon them, which will be studied in the next sections.

6.2.1 Instantaneous flow fields

Figures 6.2 and 6.3 show the sequence of instantaneous three-dimensional visualizations of the vortical structures using the Q-criterion Jeong and Hussain (1995) for two extreme cases, namely ($A_{in} = 0.01$, $f^*_{in} = 0.5$) and ($A_{in} = 0.1$, $f^*_{in} = 2$) (see supplementary movies 1 and 2). The isosurfaces, corresponding to the arbitrary value $Q = 1000$, are colored using the streamwise velocity. Figures 6.4 and 6.5 show the respective spanwise vorticity fields at the mid-spanwise plane. In addition to dimensionless time, each subfigure also indicates the corresponding phase ϕ. The three-dimensional visualizations show that the flow is fully two-dimensional upstream of the bump summit, even in the presence of vortices in the upstream part of the bump. This rules out the presence of Görtler (Marxen et al., 2009) and centrifugal global instabilities (Duck et al., 2000; Rodríguez et al., 2013) and ensures that the flow remains laminar and two-dimensional at separation in all cases.

The first case ($A_{in} = 0.01$, $f^*_{in} = 0.5$) corresponds to the weakest inflow oscillations, i.e. lowest inflow frequency and amplitude, and results in a mean recirculation length virtually identical to that of the steady case. For this case, Fig. 6.4 shows a continuous shedding of KH vortices from the separated shear layer followed by a fast transition to turbulence and recirculation of vortical structures, qualitatively identical to the steady case (cf. Fig. 3.3). However, careful observation of the separated shear layer upstream of the vortices shows some differences

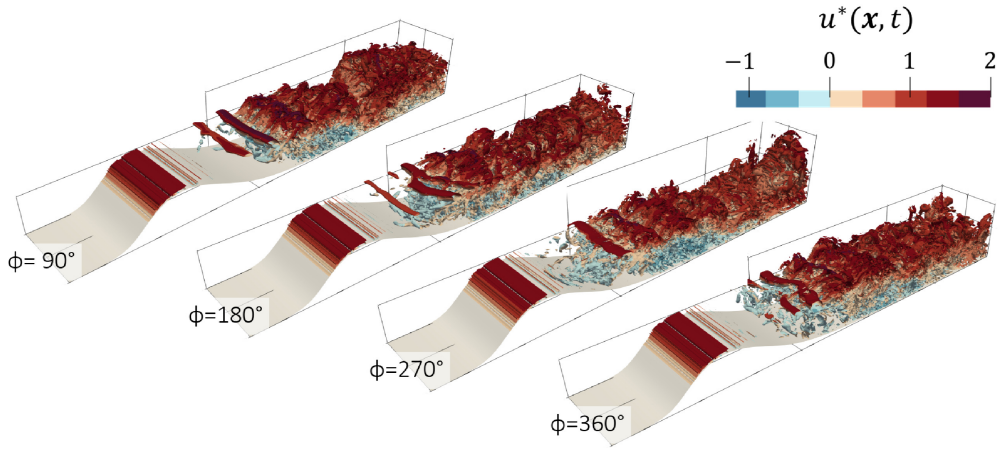

Figure 6.2: $Q(+)$ isosurface coloured by streamwise velocity. $A_{in} = 0.01$ and $f^*_{in} = 0.5$.

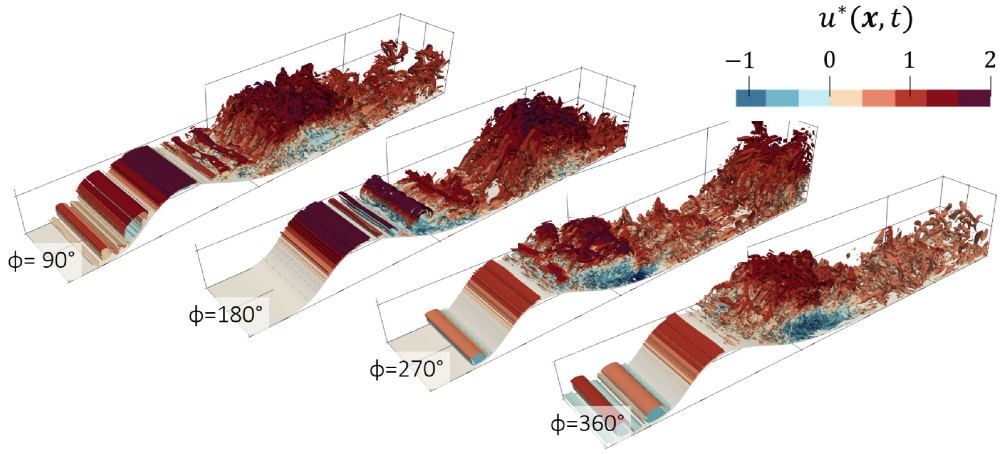

Figure 6.3: $Q(+)$ isosurface coloured by streamwise velocity. $A_{in} = 0.1$ and $f^*_{in} = 2$.

that gradually become more relevant for cases with increasing A_{in} and f^*_{in}. For $\phi = 0°$ the reference total pressure starts to increase above its mean value, exerting an acceleration of the flow along the channel. Due to the increased mass and momentum fluxes, the separated shear layer is pushed towards the bump wall. As the flow is accelerated, the high vorticity region associated with the laminar-turbulent transition is also pushed towards the wall. The maximum inflow pressure occurs at $\phi = 90°$, closely followed by the inflow bulk velocity. For ϕ between 90° and 270° the reference pressure is reduced up to its minimum value, imposing a gradual deceleration of the bulk flow. The separated shear layer moves away from the wall; the high-vorticity region seems to detach from the wall and the apparent recirculation region extends farther in the streamwise direction. Finally, when $\phi > 270°$ the flow gradually re-accelerates closing the period.

The second case ($A_{in} = 0.1$, $f^*_{in} = 2$) corresponds to the strongest inflow oscillation, i.e. the largest inflow oscillation frequency and amplitude, and results in a substantial reduction of the mean recirculation region ($\Delta L_s / L_{s,steady} \approx -44\%$). For this case, Fig. 6.5 does not show

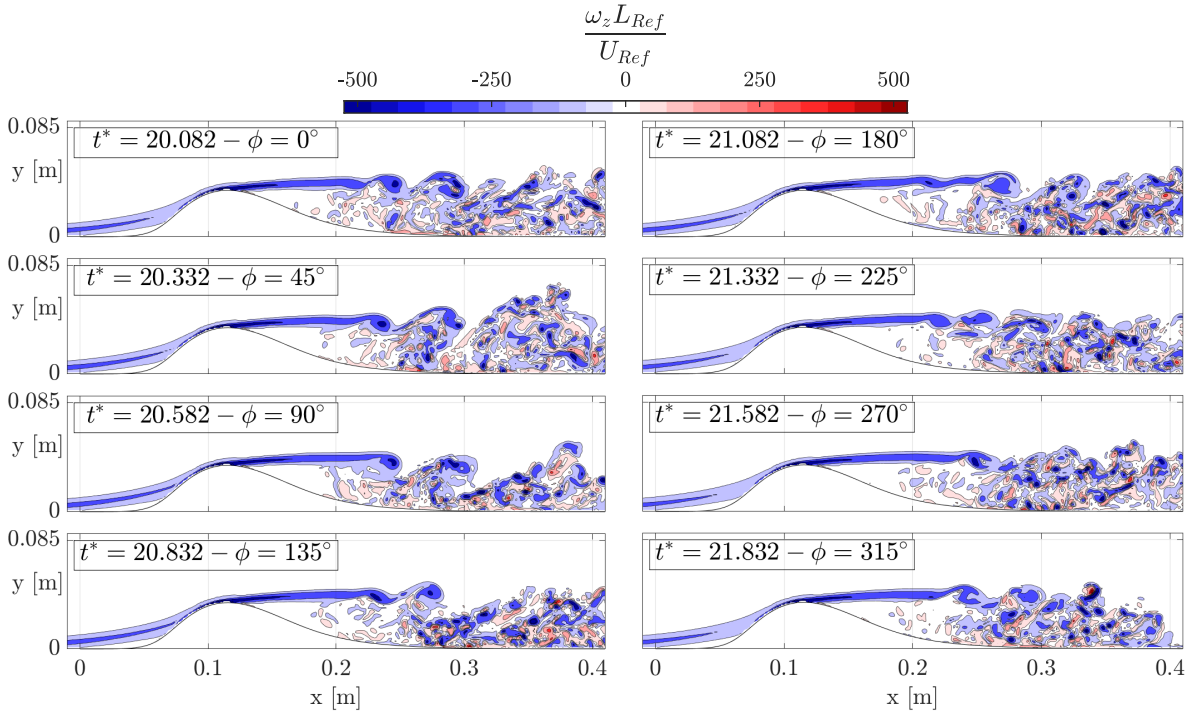

Figure 6.4: Instantaneous spanwise vorticity. $A_{in} = 0.01$ and $f^*_{in} = 0.5$.

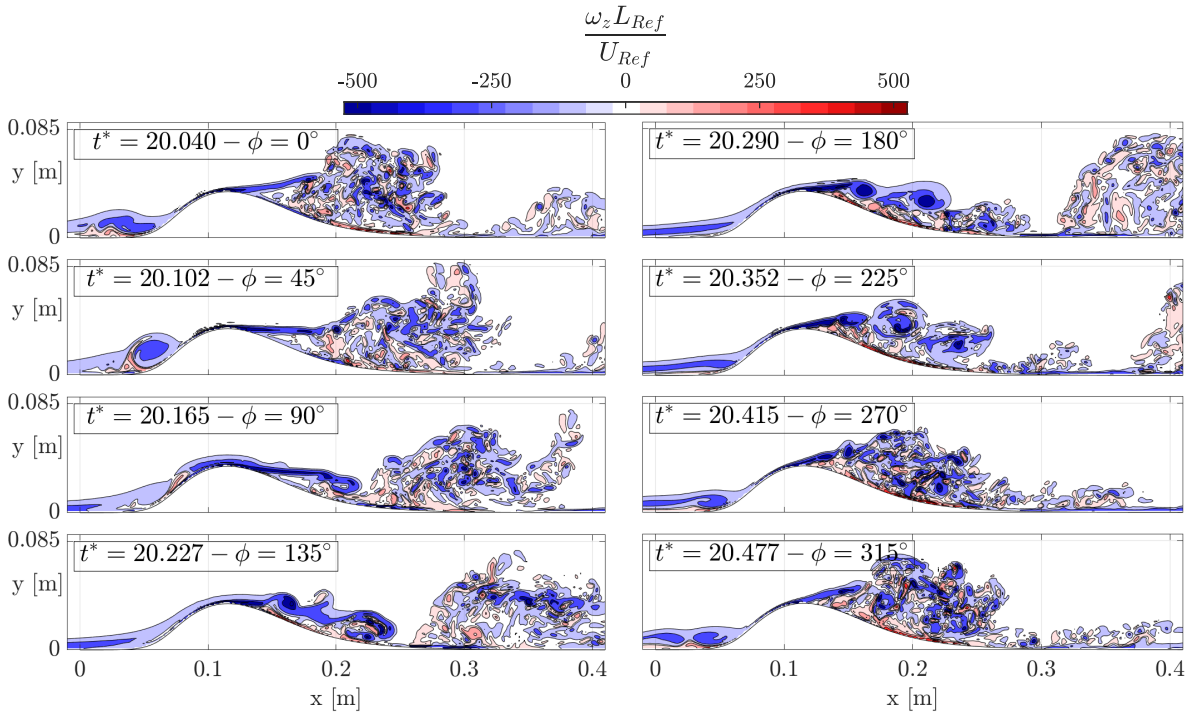

Figure 6.5: Instantaneous spanwise vorticity. $A_{in} = 0.1$ and $f^*_{in} = 2$.

a periodic shedding of KH vortices from the separated shear layer, but rather the formation and release of a big vortex cluster following the harmonic change in the inflow conditions.

These observations suggest that two closely related but different physical mechanisms are at play when the inflow has a harmonic time dependence with relatively small A_{in} and f^*_{in}. First, the periodic acceleration-deceleration of the bulk flow modifies the angle of the separated shear layer through changes in the intensity of the streamwise pressure gradient. The location of the separation point is nearly unaffected by this. Second, the periodic vertical motion of the shear layer can impact its hydrodynamic instability properties and the ensuing dynamics of the KH vortices and the laminar-turbulent transition. As will be quantified later, the frequency of the KH vortex shedding is distinctly separated from the frequency of the inflow changes. On the other hand, for relatively large A_{in} and f^*_{in}, the organized shedding of KH vortices from the separated shear layer is replaced by a periodic formation and ejection of large vortex clusters that is driven by the bulk flow acceleration and deceleration. Intermediate cases are expected to show a transition from one behaviour to the other, as will be detailed in the following sections.

With the aim of isolating the shedding of KH vortices from the bulk flow oscillations imposed by the inlet frequency, the triple decomposition proposed by Hussain and Reynolds (1970) is applied. This decomposition takes the form

$$q(\boldsymbol{x},t) = \bar{q}(\boldsymbol{x}) + \tilde{q}(\boldsymbol{x},t) + q'(\boldsymbol{x},t), \tag{6.3}$$

where $\bar{q}$ stands for the mean (time-averaged) flow, $\tilde{q}$ is the oscillatory component coherent with the inflow oscillation and q' is the incoherent component. The term "coherent" refers to flow fluctuations that occur in phase with the harmonic changes of the total pressure at the reference point. As such, the mean plus coherent components are gathered together in the phase-averaged flow

$$\langle q(\boldsymbol{x},\phi)\rangle = \frac{1}{N}\sum_{n=0}^{N} q\left(\boldsymbol{x}, t_\phi + \frac{n}{f^*_{in}}\right), \tag{6.4}$$

where t_ϕ is the time used as the phase reference, f^*_{in} is the inlet frequency and N is the number of periods used in the averaging. The incoherent part of the flow is computed as $q'(\boldsymbol{x},t) = q(\boldsymbol{x},t) - \langle q(\boldsymbol{x},t)\rangle$. The same dimensionless time-lapse was used in the averaging for the three frequencies f^*_{in}, resulting in $N = 25$ for $f^*_{in} = 0.5$, $N = 50$ for $f^*_{in} = 1$ and $N = 100$ for $f^*_{in} = 2$.

6.2.2 Mean flow fields

Figure 6.6 shows the mean (time-averaged) component of the streamwise velocity field $\bar{u}$ for the steady inflow case, the former two extreme cases of inflow oscillations ($A_{in} = 0.01$, $f^*_{in} = 0.5$) and ($A_{in} = 0.1$, $f^*_{in} = 2$), and the intermediate case ($A_{in} = 0.05$, $f^*_{in} = 1$). The thick black lines correspond to the time-averaged separation streamline. These results illustrate how the mean extent of the separated flow is only slightly reduced when the intensity of the inflow oscillations is mild but reduced considerably for the strongest inflow oscillations. The peak reversed flow exceeds 20% of the reference velocity for the steady inflow case, and is increased

up to nearly 50% for ($A_{in} = 0.1$,f^*_{in}=2). Such intense reversed flow values suggest that, in all cases, a self-excited vortex shedding is possible originating from an absolute Kelvin-Helmholtz instability (Avanci et al., 2019; Hammond and Redekopp, 1998).

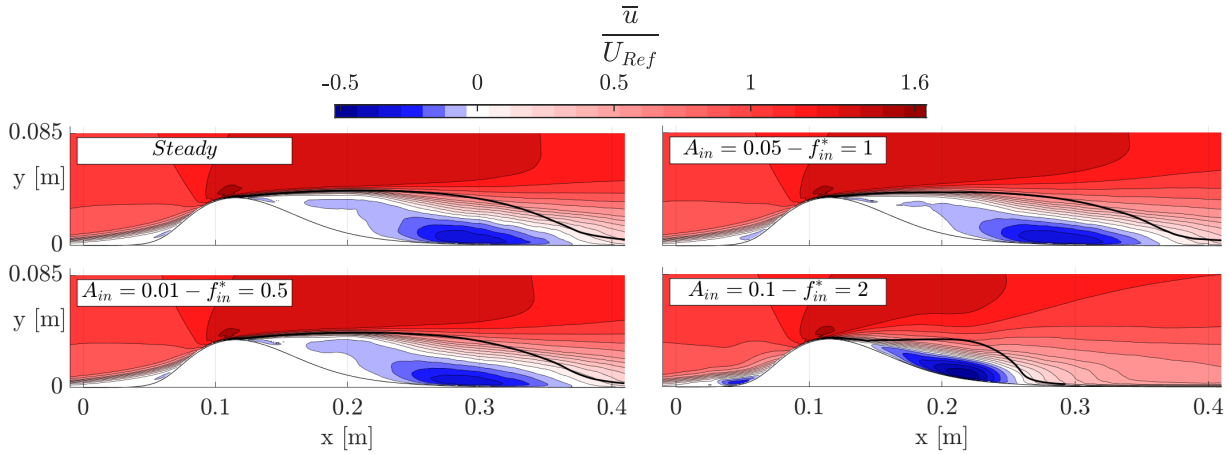

Figure 6.6: Time-averaged streamwise velocity field - harmonic inflow

Figure 6.7 shows the root-mean-square (r.m.s.) of all flow fluctuations (phase-averaged plus incoherent components, central column) and of the incoherent component alone (right column). The r.m.s. of the incoherent component shows intense fluctuations in the downstream part of the recirculation region, with its peak roughly coincident with the streamwise coordinate of the peak reversed flow and located on the separation streamline, which are typical features of laminar separation bubbles. For the case with strongest inflow oscillations, this peak is displaced inside of the separation streamline, indicating that the flow fluctuations that are uncorrelated with the inflow oscillations are contained in the recirculation region. This will be discussed in more detail in Section 6.4. The r.m.s. of the complete fluctuations are identical to those for the incoherent component for the steady- and weak-inflow oscillation cases. A gradual departure appears as the amplitude of the inflow oscillation increases, as the relative intensity of the coherent component increases and becomes dominant. These fluctuations, then concentrated on the separation shear layer, upstream of the peak of the incoherent fluctuations, are associated with phase-averaged changes in the shape and size of the recirculation region. These changes are discussed in the next section.

In addition to the main recirculation region that is formed downstream of the bump, a smaller recirculation appears upstream of it, analogous to those appearing in forward-facing steps (e.g. Bowen and Lindley (1977)). While the appearance of this upstream recirculation is not caused by the inflow oscillations, vortices are periodically released for the cases with larger A_{in} that can interact with the main recirculation region. However, self-excited vortex shedding does not happen in the upstream recirculation, which also remains two-dimensional as shown in Figs. 6.2 and 6.3.

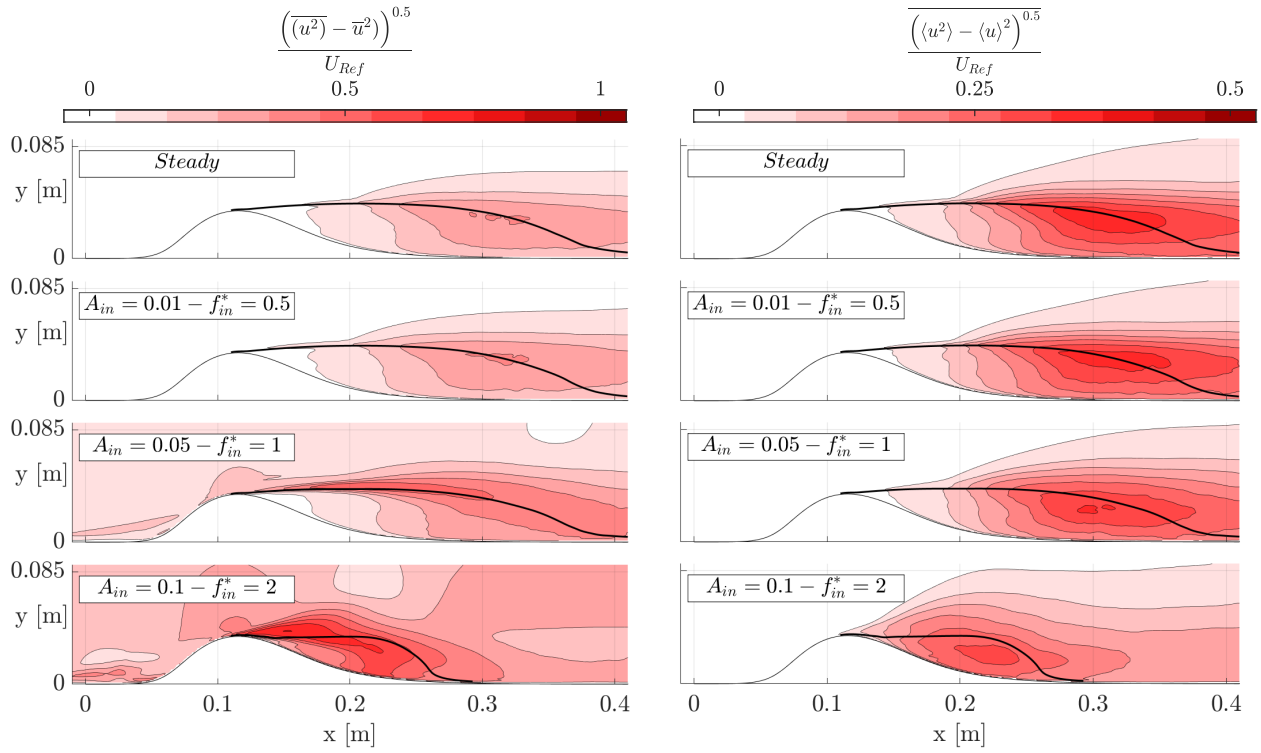

Figure 6.7: Root-mean-square (left) and root-mean-square of the incoherent component (right) of streamwise velocity field - harmonic inflow

6.2.3 Phase-averaged flow fields

Figures 6.8 to 6.10 show the evolution of the phase-averaged spanwise vorticity fields at the midspan plane for the three representative unsteady inflow cases. The thick black lines in the figures approximate the separation streamline at each phase. This line is computed by neglecting the spanwise velocity component in the phase-averaged flow and integrating $dx/\langle u\rangle = dy/\langle v\rangle$ starting at the approximate location of the separation point.

For the case with the weakest inflow oscillation ($A_{in} = 0.01$, $f^*_{in} = 0.5$, Fig. 6.8), phase averaging successfully isolates the shear layer motion that is coherent with the inflow changes from the KH vortex shedding: the periodic motion of the shear layer towards and apart from the wall is captured in the phase-averaged field, but no imprint of individual vortices or details of the subsequent transition are captured. Instead, the phase-averaged shear layer seems to diffuse as it evolves downstream, occupying the space where vortical structures are identified in the instantaneous flow. This region extends from the separated shear layer to the wall and presents a noticeable patch of positive vorticity adjacent to the wall for all phases; the latter is the imprint of vortical structures that are recirculated in the separation bubble.

The intermediate case ($A_{in} = 0.05$, $f^*_{in} = 1$, Fig. 6.9) shows more clearly the vertical flapping motion of the shear layer. In contrast to the previous case, the positive vorticity region apparently disappears for phase angles corresponding to the bulk flow acceleration ($\phi \approx 0°$ in the figure) and becomes more intense around the peak deceleration ($\phi \approx 180°$) where the

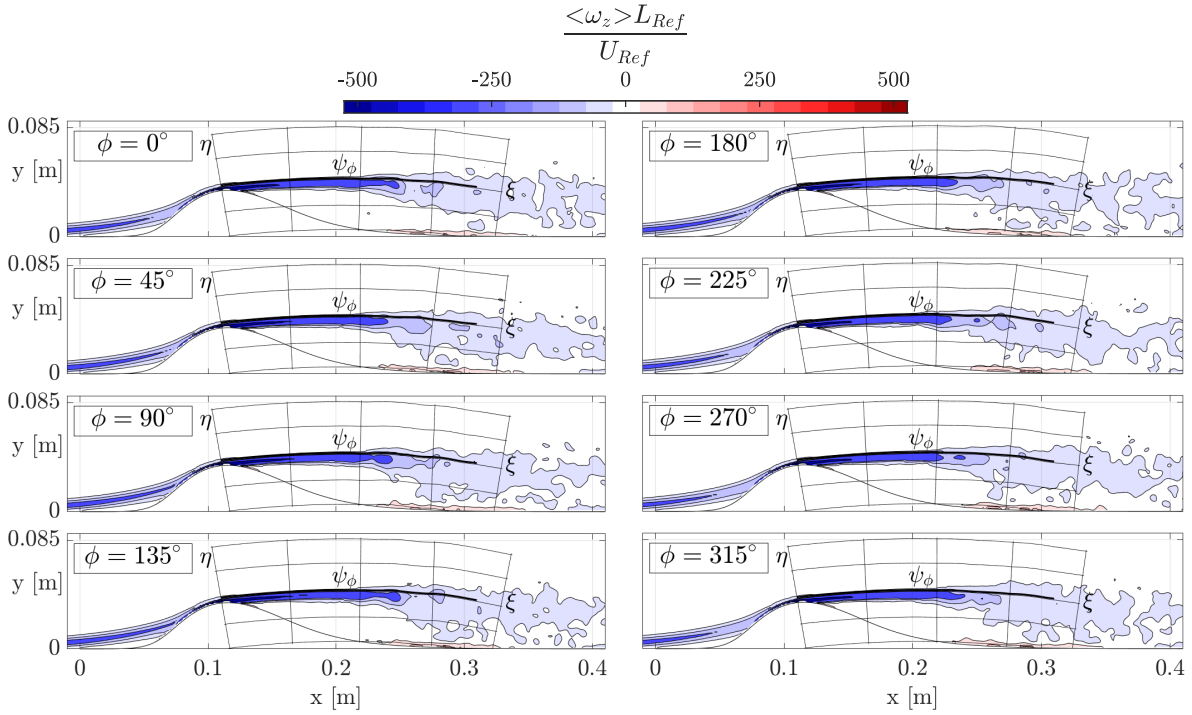

Figure 6.8: Phase-averaged spanwise vorticity. $A_{in} = 0.01$ and $f^*_{in} = 0.5$.

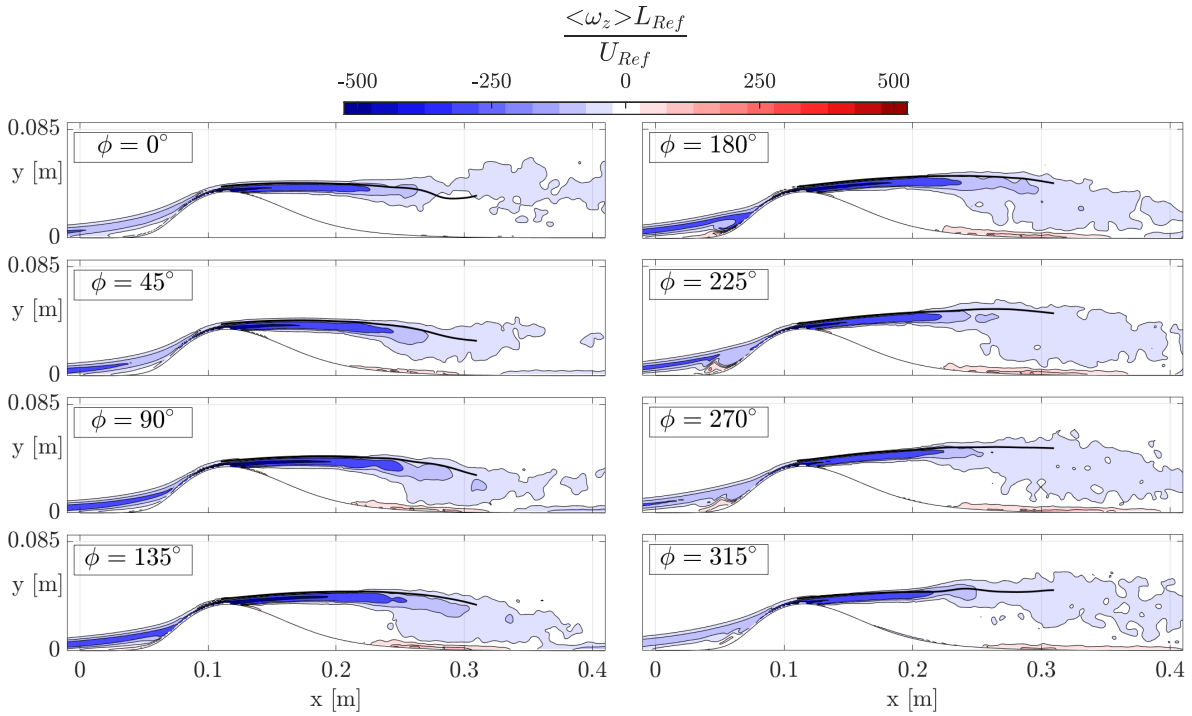

Figure 6.9: Phase-averaged spanwise vorticity. $A_{in} = 0.05$ and $f^*_{in} = 1$.

wall-normal extension of the recirculation region is larger.

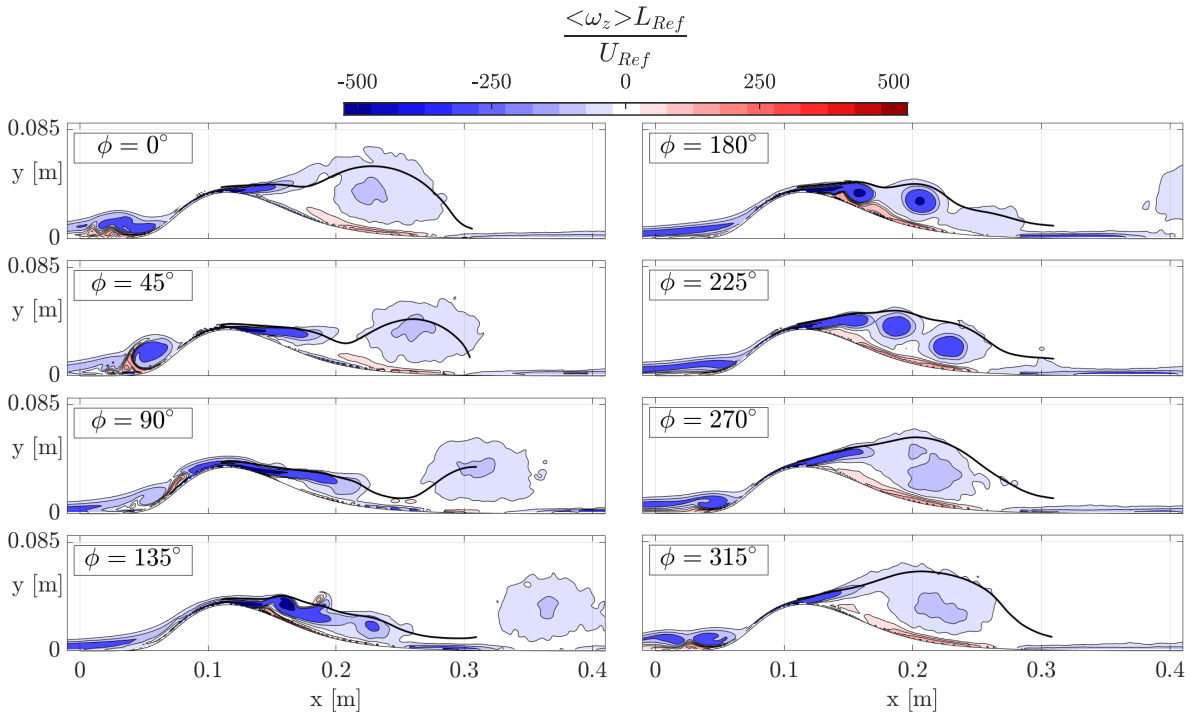

Figure 6.10: Phase-averaged spanwise vorticity. $A_{in} = 0.1$ and $f^*_{in} = 2$.

Finally, Fig. 6.10 shows the phase-averaged vorticity for the case with strongest inflow oscillations ($A_{in} = 0.1$, $f^*_{in} = 2$). The phase-averaged field recovers the periodic formation and release of large patches of spanwise vorticity, coherent with the harmonic change of the bulk velocity. Phase $\phi = 270°$ corresponds approximately to the conditions of minimum bulk velocity; for this phase, a vortex of size comparable to the bump is clearly defined downstream of the bump summit. As the flow re-accelerates, the vortex is released ($\phi \approx 0°$) and advected downstream pushing the separation shear layer towards the wall, sensibly reducing the length of the separated flow region. Concurrently with this, a smaller two-dimensional vortex is formed upstream of the bump for $270° \leq \phi \leq 45°$, which is shed at $\phi \approx 45°$ and reaches the bump summit at $\phi \approx 90°$. This vortex interacts with the separated shear layer giving rise to two coherent vortices ($\phi \approx 180°$) that subsequently break down into smaller structures, as shown in the instantaneous flow visualization of Fig. 6.5. However, the phase-averaged field does not capture the evolution of these vortices after $\phi \approx 225°$, indicating that their dynamics are chaotic and not reproduced from cycle to cycle. Comparing the instantaneous and phase-averaged fields (respectively Figs. 6.5 and 6.10), it is observed that the vortical structures originated by the upstream vortex are completely entrapped in the recirculation region and contribute to its re-generation.

6.3 Impact of the inflow conditions on streamwise acceleration and length of the separated flow

The phase-averaged fields provide relevant information regarding the impact of the harmonic inflow changes on the streamwise flow acceleration and deceleration and the resulting length of the separated flow region.

In order to quantify the phase-dependent streamwise acceleration, the dimensionless parameter

$$\langle K\left(\boldsymbol{x},\phi\right)\rangle = \left\langle \frac{\nu}{u^3\left(\boldsymbol{x},\phi\right)}\left(\frac{\partial u\left(\boldsymbol{x},\phi\right)}{\partial t} + u\left(\boldsymbol{x},\phi\right)\frac{\partial u\left(\boldsymbol{x},\phi\right)}{\partial x}\right)\right\rangle \tag{6.5}$$

is used, that can be further divided into two contributions: the contribution from the local flow acceleration

$$\left\langle K_{\partial u/\partial t}\left(\boldsymbol{x},\phi\right)\right\rangle = \left\langle \frac{\nu}{u^3\left(\boldsymbol{x},\phi\right)}\frac{\partial u\left(\boldsymbol{x},\phi\right)}{\partial t}\right\rangle \tag{6.6}$$

and the convective acceleration

$$\left\langle K_{\partial u/\partial x}\left(\boldsymbol{x},\phi\right)\right\rangle = \left\langle \frac{\nu}{u^2\left(\boldsymbol{x},\phi\right)}\frac{\partial u\left(\boldsymbol{x},\phi\right)}{\partial x}\right\rangle. \tag{6.7}$$

This parameter was introduced by P. R. Spalart (1986a) as a pressure gradient parameter in studies of flow relaminarization under favorable pressure gradients ($K > 0$) but it is also used to quantify the flow deceleration associated with an adverse pressure gradient ($K < 0$) (Ambrogi et al., 2022; Dellacasagrande et al., 2020; Saavedra and Paniagua, 2018; Suzen et al., 2003) in boundary layer flows. In the ideal scenario of a boundary layer that is unbounded on the wall-normal direction, the free-stream value of the streamwise velocity would be used and Bernoulli's equation would relate it directly to the streamwise pressure gradient. In the geometry used herein, the upper wall of the channel prevents using this definition. As an approximation to the free-stream velocity, the streamwise velocity at the plane $y = 0.1$ m is used, which corresponds approximately to the midpoint between the bump summit and the upper wall. The streamwise velocity on this plane is expected to be less affected by the instantaneous vortical structures and viscous effects on the separated flow region, though the irrotational flow is strictly not attained. Figure 6.11 shows the spatio-temporal evolution of the phase-averaged acceleration parameter $\langle K\rangle$, for the three representative cases of harmonic inflow oscillation. The steady inflow case is also shown for comparison.

For the same cases, Fig. 6.12 shows the temporal evolution of the dimensionless streamwise skin friction at the mid-span plane, defined as

$$Cf\left(\boldsymbol{x},\phi\right) = \frac{\langle\tau_w(\boldsymbol{x},\phi)\rangle}{p_t\left(\boldsymbol{x}_{ref},\phi\right) - p\left(\boldsymbol{x}_{ref},\phi\right)}, \tag{6.8}$$

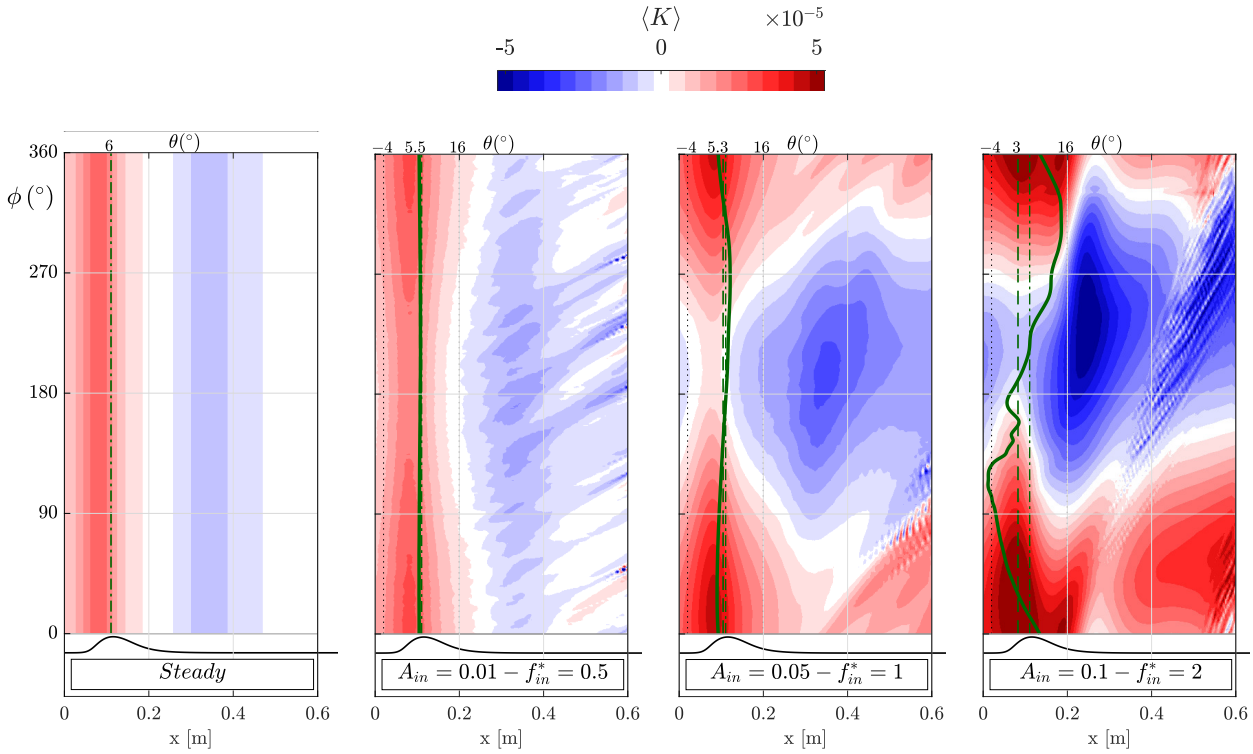

Figure 6.11: Contours: Phase-averaged streamwise acceleration parameter at $y = 0.1$ m. Green lines: angle of the streamline at the separation point Γ corresponding to the phase-averaged component (solid line), the mean component (dashed) and the steady inflow case (dashed-dotted)

where $\boldsymbol{x}_{ref}$ corresponds to the location of the reference point (cf. Table 3.3). The phase-averaged location of the separation and reattachment point are also shown in the figure, illustrating the streamwise length of the main recirculation region.

The steady inflow case shows the flow acceleration-then-deceleration distribution generated by the bump. The minimum K value is obtained at $x \approx 0.35$ m, which is coincident with the location of minimum Cf. The time-averaged reattachment occurs a short distance downstream and can be identified as the coordinate where the skin friction changes from negative to positive. The streamwise acceleration parameter is still negative at reattachment, illustrating that the reattachment originated from unsteady flow entrainment rather than the action of a streamwise flow acceleration. Case ($A_{in} = 0.01$, $f^*_{in} = 0.5$) shows the same features as the steady inflow case, with a small amplitude modulation that follows the inlet frequency.

The cases with increasingly stronger/faster inflow oscillations exhibit a pattern of phase-dependent deceleration-acceleration localized in the reattachment region that is repeated with each period. For the intermediate case ($A_{in} = 0.05$, $f^*_{in} = 1$), the minimum value of $\langle K \rangle$ occurs for $\phi \approx 180°$, coincident with the peak bulk flow deceleration. As the flow re-accelerates for $\phi > 270°$, the region of negative $\langle K \rangle$ is displaced downstream and reduced in size. Then, for the peak acceleration phase $\phi = 0°$, $\langle K \rangle$ is positive around the time-averaged reattachment point. This evolution of $\langle K \rangle$ is followed by the Cf distribution. At $\phi = 0°$, the reattachment

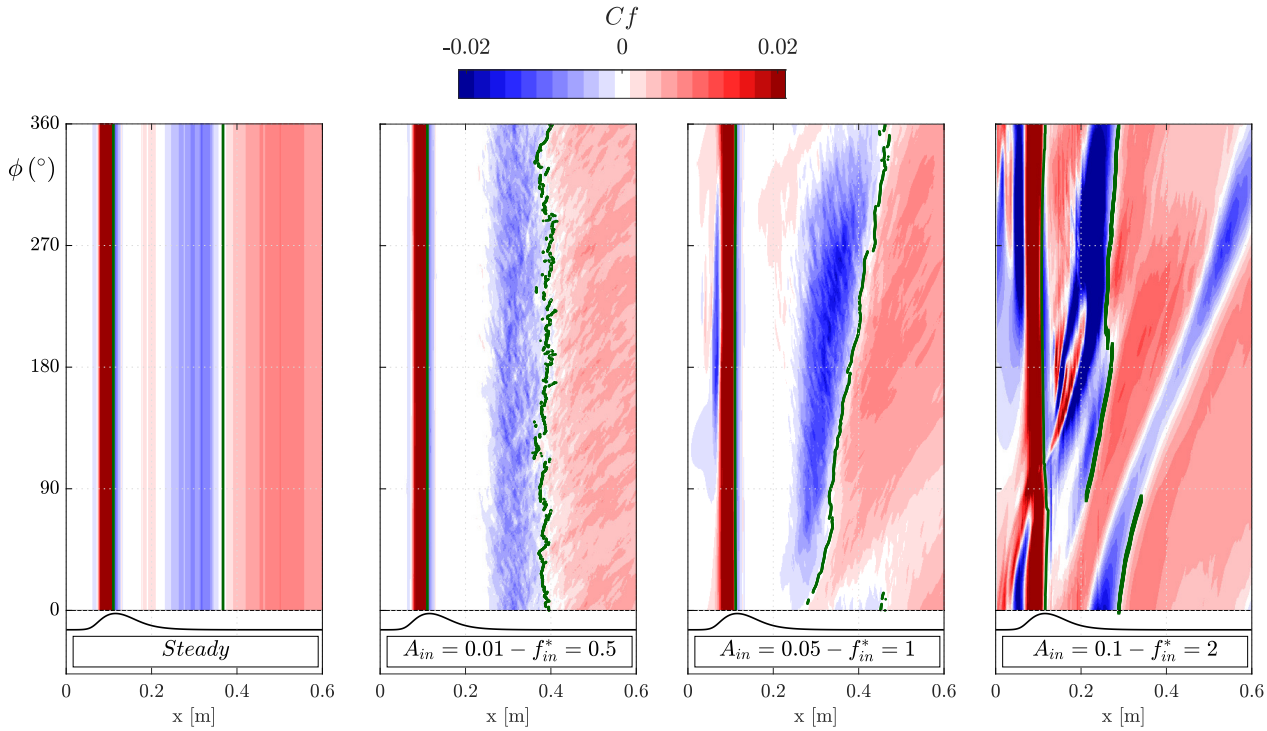

Figure 6.12: Phase-averaged skin friction at the mid-span of the bump surface. Left: $A_{in} = 0.01$, $f^*_{in} = 0.5$. Center: $A_{in} = 0.05$, $f^*_{in} = 1$. Right: $A_{in} = 0.1$, $f^*_{in} = 2$. The location of the phase-averaged separation and reattachment points is shown as a green dot for each discrete phase value

point is located around $x = 0.25$ m; reattachment moves downstream gradually for increasing ϕ, resulting in a longer recirculation bubble. During the flow re-acceleration, a new region of positive skin friction is formed upstream of the region of minimum Cf, implying that a large coherent vortical structure has been released and a new one is being formed.

Finally, the case ($A_{in} = 0.1$, $f^*_{in} = 2$) shows new distinct features both in the acceleration parameter and the skin friction. For relatively elevated values of A_{in} and f^*_{in} the local flow acceleration $\langle K_{\partial u/\partial t} \rangle$ becomes comparable to the convective one. In consequence, $\langle K \rangle$ is alternatively positive or negative during about half of the period. The peak deceleration is now displaced to the later phase $\phi \approx 275°$. However, its peak magnitude is increased substantially with respect to the case ($A_{in} = 0.05$, $f^*_{in} = 1$), and as a result the same negative values of $\langle K \rangle$ are reached before in the period. For instance, case ($A_{in} = 0.05$, $f^*_{in} = 1$) presents the minimum $\langle K \rangle$ value -24.74×10^{-6} at ϕ slightly above 180°, while this value is attained in case ($A_{in} = 0.1$, $f^*_{in} = 2$) already at $\phi = 135°$. The intense periodic acceleration-deceleration influences the Cf distribution notably, involving the formation of multiple recirculation regions that are related to the advection of the coherent vortex clusters shown in Fig. 6.10. Cross-comparison of the streamwise acceleration and skin friction (cf. Fig. 6.11 and 6.12) suggests that the formation and release of the large vortical structures in the coherent flow component are associated to surpassing a threshold negative value of the acceleration parameter $\langle K \rangle$. The reasons for this will be further discussed in later sections.

Figure 6.11 also shows the angle of the separation streamline with the x-direction at the separation point corresponding to the phase-averaged flow, the mean flow and the steady inflow case. Under steady flow conditions, a direct relation exists between the streamwise pressure gradient (K), the gradient of the wall shear ($\partial Cf/\partial x$) and the separation angle Γ (Lighthill, 1963):

$$\tan\Gamma = -B\left(\frac{\partial Cf}{\partial x}\Big/ K\right)_s, \tag{6.9}$$

where B is a dimensionless constant and the subscript s refers to the separation point. This dependence of Γ on K and Cf together with the complex dependence of the latter on the harmonic inflow oscillations anticipates that the separation angle has a strongly nonlinear behavior. The steady inflow case presents a mean angle $\Gamma \approx 6$ deg. Following the periodic changes in $\langle K\rangle$, the shear layer moves towards and apart the wall which translates in a reduction or increase of the streamline angle at separation. For increasingly stronger inflow oscillations, the mean separation angle is reduced and its oscillation amplitude increased. In line with the phase-averaged oscillations of the separated shear layer already discussed, the separation angle oscillations become substantial for the strongest inflow oscillation case ($A_{in} = 0.1$, $f^*_{in} = 2$) and a phase-delay appears between the extreme values of $\langle K\rangle$ (positive or negative) and the angle.

The streamwise length of the recirculation bubble L_s is computed at each phase ϕ as the distance between the separation point near the bump summit and the first reattachment point downstream, that are highlighted as green dots in Fig. 6.12. Due to the fine discretization of ϕ, the black dots visually form nearly continuous lines. Figure 6.13 shows the probability density function (PDF) of $\langle L_s\rangle$ for all the simulated cases. The time-averaged length for each case and the time-averaged length for the steady inflow case are also shown. Table 6.1 tabulates the numeric values. Cases with relatively low values of A_{in} and f^*_{in} (towards the upper left panels of the figure) show that the recirculation length remains close to that of the steady inflow case with a very narrow distribution range. As A_{in} or f^*_{in} are increased individually (e.g., $A_{in} = 0.05$, $f^*_{in} = 1$), the PDF becomes significantly broader, indicating large changes in $\langle L_s\rangle$ over the period. The time-averaged recirculation length is reduced in all cases, but the distribution is not centered around it and the length at some phases can be substantially longer or shorter than $L_{s,steady}$. This intense temporal variation of $\langle L_s\rangle$ is expected to be associated with periodic changes in the aerodynamic forces exerted on the bump, which may be highly undesirable in the practical scenario of a low-pressure turbine (Curtis et al., 1997). Finally, the cases with larger values of A_{in} and f^*_{in} (towards the bottom right panels of Fig. 6.13, and particularly $A_{in} = 0.1$, $f^*_{in} = 2$) present a PDF which is again centered on the mean L_s value. This value is remarkably reduced with respect to $L_{s,steady}$. Notably, the PDF tail falls to zero for recirculation lengths below $L_{s,steady}$, implying that the separation length is reduced for all phases, including those in which the bulk flow is decelerated. This is also relevant in practical scenarios, as the detrimental effects of flow separation would be consistently reduced with respect to the steady inflow case.

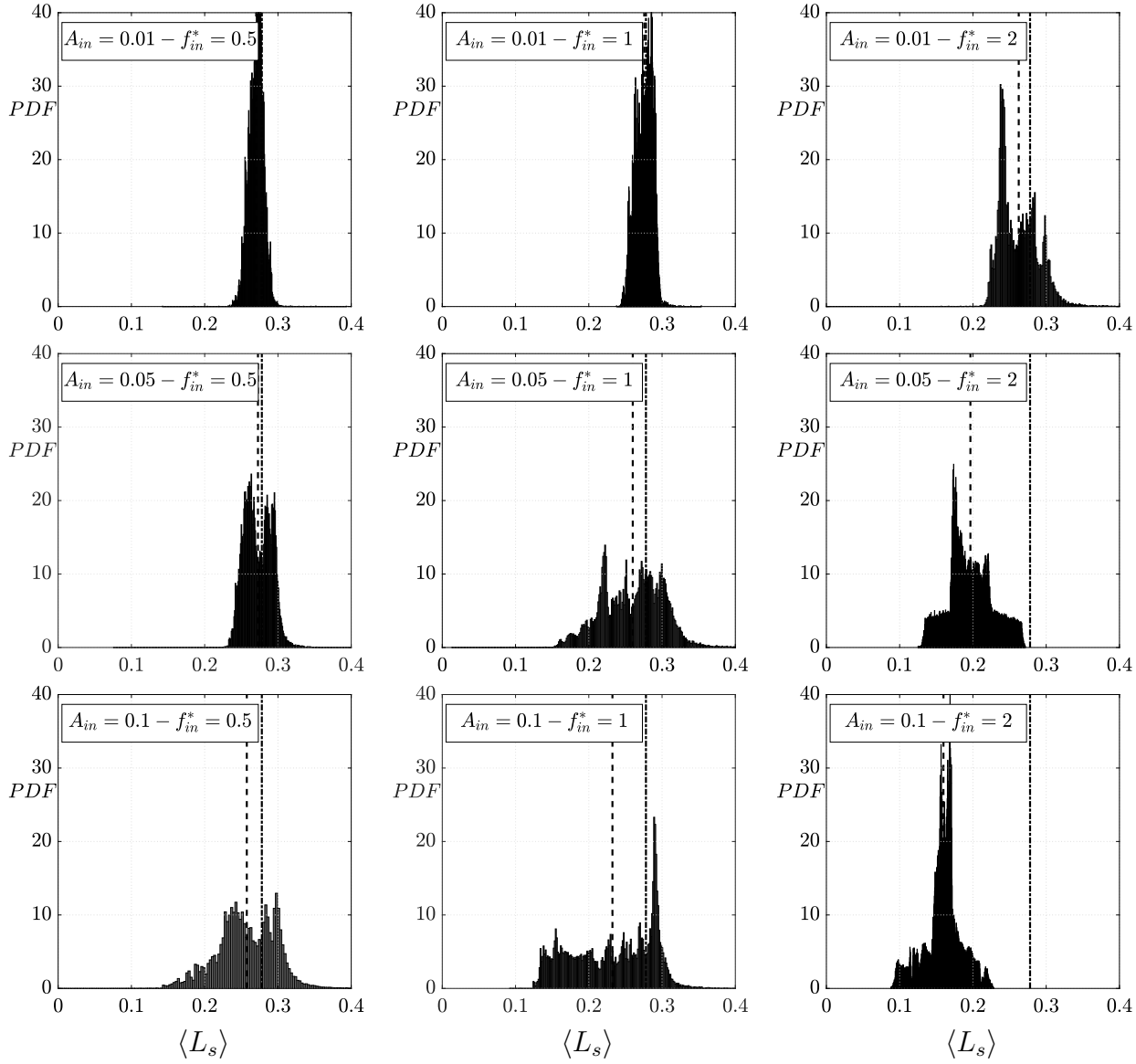

Figure 6.13: Probability density function of the phase-averaged recirculation bubble length $\langle L_s \rangle$. (- - -) time-averaged value; (-·-·-) time-averaged for the steady inflow case, $L_{s,steady}$.

6.4 Incoherent vorticity and vortex dynamics

The phase-averaged results in the previous section illustrate the overall dynamics of the shear layer and the behaviour of the separated flow on account of the harmonic inflow changes. The length of the recirculation region and the impact of the inflow oscillation frequency and amplitude are, in turn, a consequence of changes in the vortex dynamics induced by the transient changes in the streamwise acceleration. For comparatively low values of A_{in} and f^*_{in}, vortex rolls are formed at the separated shear layer resulting from the KH instability, which initiates the laminar-to-turbulent transition. The spread of the shear layer, entrainment of fluid into the recirculation region and ultimately flow reattachment are governed by the

complex dynamics of these vortices. These processes are not captured by the phase-averaged fields, which only recover their consequences.

For low f^*_{in}, the characteristic period in which the shear-layer motion occurs is much longer than the characteristic time for the formation and advection of the vortices, as will be shown below. In consequence, the vortex dynamics are completely recovered in the incoherent flow component q' of the triple decomposition. The vortices are formed and initially move along the separated shear layer, whose motion is captured by the phase-averaged component. To separate the vortex dynamics from the shear-layer motion, the following procedure is adopted. First, an orthogonal curvilinear coordinate system (ξ, η) is defined, as shown in Fig. 6.8. The line $\eta = 0$ corresponds to the phase-averaged separation streamline and ξ is the curvilinear coordinate measured along it. Then, an inverse transformation is performed to map the curvilinear-coordinates grid points to cartesian coordinates with the streamline as the centerline axis. Details of the inverse transformation process are described by Legleiter and Kyriakidis (2006).

This shear-layer fitted system of coordinates is inspired by the one used by Himeno et al. (2021) to study the vortex dynamics along the steady shear layer formed within a slat cove. In the present case, the curvilinear coordinates depend on the phase angle, following the motion of the phase-averaged separation streamline. Figure 6.14 shows the total (left column), the phase-averaged (middle column) and the incoherent (right column) components of the spanwise vorticity in the curvilinear mesh, for the case representative of the weaker inflow oscillations ($A_{in} = 0.01$, $f^*_{in} = 0.5$). Note that the phase-averaged separation streamline corresponds to the horizontal line $\eta = 0$, and the bump wall is mapped to a curve line with $\eta < 0$ whose geometry changes with the phase.

The incoherent component portrays a complex arrangement of vortices typical of a transitional shear layer (Diwan and Ramesh, 2009; Marquillie and Ehrenstein, 2003; Marxen et al., 2013; McAuliffe and Yaras, 2009). The process is initiated with the formation of organized pockets of spanwise vorticity in the initial part of the shear layer. These vortices grow in amplitude as they travel downstream along $\eta = 0$, soon reaching non-linear amplitudes and then interacting and merging with the recirculating vortical structures adjacent to the wall.

To visualize the spatio-temporal dynamics of these vortices, the incoherent spanwise vorticity ω'_z at $\eta = 0$ is plotted in the (ξ, t^*) plane for the steady inflow case and the three cases representative of harmonic inflow in Fig. 6.15. Note that ω'_z is a disturbance superimposed upon the phase-averaged flow and consequently its positive and negative values do not directly imply vortical structures rotating both in clockwise and counter-clockwise directions.

The steady inflow case shows the continuous formation of vortical structures of similar amplitude and apparent shedding frequency that propagate downstream at a nearly constant speed along the mean shear layer. With the choice of contour levels used, they become observable around $\xi = 0.1$ m, which for the steady case corresponds to $x \approx 0.2$ m. Case ($A_{in} = 0.01$, $f^*_{in} = 0.5$) presents a very similar picture, but the location where the vortical structures are first seen now oscillates very mildly following the inflow phase; bulk flow deceleration displaces the observable incoherent vorticity upstream and *vice versa*. The modulation of the vortex shedding location is increased by increasing either A_{in} or f^*_{in}.

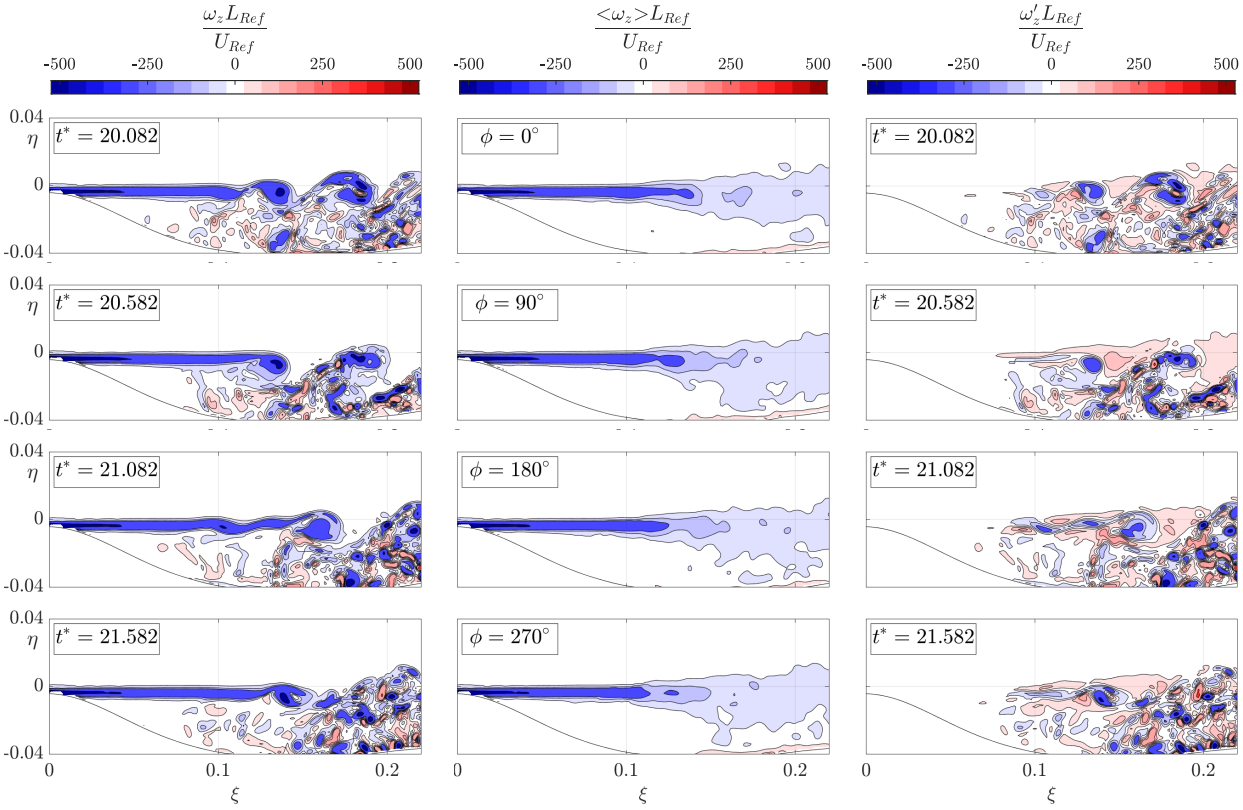

Figure 6.14: Triple decomposition of spanwise vorticity. $A_{in} = 0.01$ and $f^*_{in} = 0.5$.

The intermediate case ($A_{in} = 0.05$, $f^*_{in} = 1$) presents an additional feature for certain regions of the (ξ, ϕ) plane. As in the previous cases, regular periodic positive and negative streaks of vorticity are visible, with their initial ξ location following the inflow fluctuation phase. However, for a certain phase range (between $\phi = 3\pi/2 = 270°$ and $\phi = 2\pi = 360°$) this pattern is replaced by a "wedge" of distinct behaviour, as schematized in the corresponding panel of Fig. 6.15. The wedge originates at the phase $\phi \approx 3\pi/2$, for which ω'_z reaches observable amplitudes sensibly upstream than for the preceding phases. From this point, two rays depart at different downstream speeds that enclose a region where the vorticity presents a disorganized behaviour.

The wedge's origin is coincident with the phase of minimum bulk velocity. This is interpreted in the following manner: during most of the inflow period, the vortex dynamics follow the same qualitative picture as for the lower A_{in} and f^*_{in} cases, characterized by a regular formation of KH vortices for which the shedding location follows the inflow phase. At some instant during the phase-average deceleration ($90° < \phi < 270°$), the streamwise deceleration parameter $\langle K \rangle$ surpasses a threshold value in the region neighbouring the reattachment point. As a result, the KH vortices and other shear layer eddies are not released from the rear part of the reversed flow region but are entrapped in the recirculation region and initiate the formation of a large cluster of vortical structures. Immediately following the beginning of the acceleration phase, the large vortex cluster is released, similar to the shedding of leading-edge vortices in oscillating airfoils (e.g. Lind and Jones (2016)).

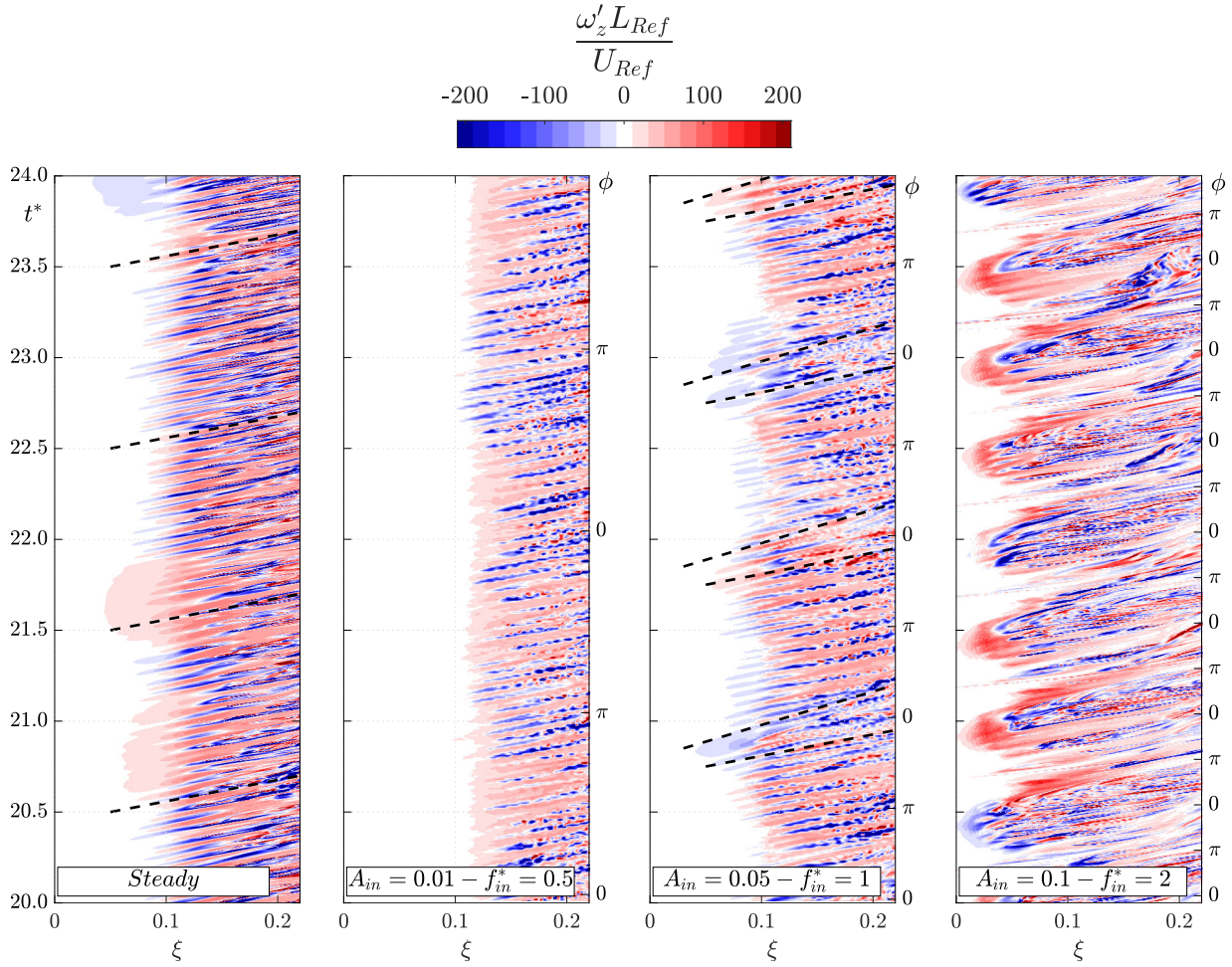

Figure 6.15: Incoherent spanwise vorticity at $\eta = 0$ for the steady inflow case and the three representative cases with harmonic inflow.

The vortex cluster is advected downstream during the initial part of the acceleration phase and subsequently, the regular shedding of KH vortices resumes. In the visualization of the phase-average flow for this case (Fig. 6.9) a large vortex cannot be clearly discerned, but the presence of the vortex lump can be inferred by the changes in the streamline curvature between $\phi = 315°$ and $360°$ and by the emergence of a region with positive Cf within the main recirculation, prior to its release, in Fig. 6.12. The formation and release of a large vortex cluster is more easily observed by visualizing the complete flowfield (without separating phase-averaged and incoherent components), as done in Fig. 6.16.

Finally, the incoherent vorticity for the case ($A_{in} = 0.1$, $f^*_{in} = 2$) does not present a regular shedding of KH vortices akin to the steady or low inflow frequency cases. Instead, it is characterized by the continuous appearance of wedges, corresponding to the periodic formation and shedding of large vortex clusters following the inflow changes. With the large vortex cluster being recovered in the phase-averaged flow (Fig. 6.10), the incoherent component consists of smaller size eddies that are trapped and evolve inside the recirculation region during the deceleration part of the period and are convected downstream when the vortex

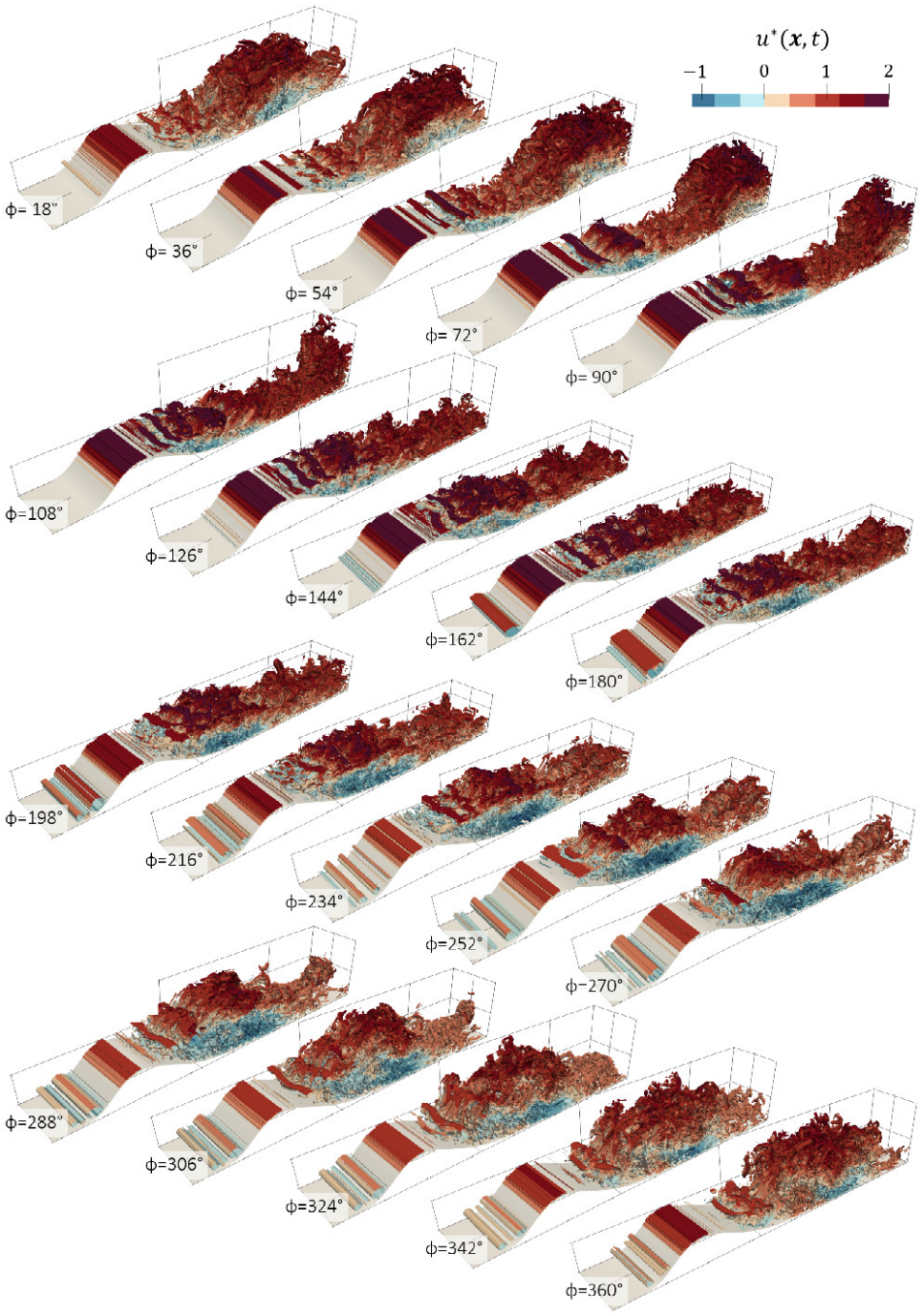

Figure 6.16: $Q(+)$ isosurface coloured by streamwise velocity. $A_{in} = 0.1$ and $f^*_{in} = 1$.

cluster is released. Owing to their chaotic nature, these structures are not repeated from cycle to cycle and hence are not coherent with the inflow changes, but their presence in the ω'_z field allows the location and tracking of the coherent vortex clusters.

6.5 Frequency spectra

Frequency spectra are studied in this section to further the characterization of the impact of the inflow oscillations on the separated flow dynamics. The procedure for the calculation of the power spectral densities (PSD) for the steady inflow case is described in Section 3.1.3. For the harmonic inflow cases, the procedure is adapted to account for the periodic nature of the data. The sampling parameters are summarized in Table 6.2. To allow for comparisons, the same averaging period is used for all cases, corresponding to the lowest of the inflow frequencies, $\Delta f^* = 0.5$. Thus, the averaging is done over segments comprising one inflow period for $f^*_{in} = 0.5$, two periods for $f^*_{in} = 1$ and four periods for $f^*_{in} = 2$. For all cases, the PSD is averaged over 25 segments of length $1/\Delta f^* = 1/0.5 = 2$.

Table 6.2: Temporal sampling parameters: N_s: total number of snapshots; Δt^*_s: time-step between snapshots used in the analysis; N_{ss}: number of snapshots per segment.

f^*_{in}	N_s	Δt^*_s	N_{ss}	Overlap
steady	2 410 000	3×10^{-5}	66 666	50%
0.5	50 000	1×10^{-3}	2000	0%
1	50 000	1×10^{-3}	2000	0%
2	100 000	5×10^{-4}	4000	0%

Figure 6.17 shows the spectra of the streamwise and wall-normal velocity components at Probe 4 (see Fig. 3.9 and Table 3.3). For the steady inflow case, this probe is located just outside of the separated shear layer at the streamwise location where the first KH vortices are formed. The spectra for the steady inflow and the weak inflow oscillation ($A_{in} = 0.01$, $f^*_{in} = 0.5$) cases are identical, presenting a narrowband peak at frequencies $f^* = 15 - 21$ with a maximum at $f^* \approx 18$ at early stage of separation. As shown in Fig. 3.10, this frequency corresponds to KH instability and follows accurately the scaling proposed by Diwan and Ramesh (2009). The intermediate case ($A_{in} = 0.05$, $f^*_{in} = 1$) also exhibits the narrowband peak corresponding to the KH vortices; the peak amplitude and frequency remain comparable to that of the steady forcing case, but the sidebands are broader. However, new peaks appear for the inflow frequency and its harmonics. The f^*_{in} peak has an amplitude that is two orders of magnitude larger than the peak KH frequency. The spectra for the case with the strongest inflow oscillation ($A_{in} = 0.1$, $f^*_{in} = 2$) also contain the peaks corresponding to the inflow frequency and its harmonics. However, the narrowband peak corresponding to KH vortices is not observable in this case. The amplitude for all frequencies is increased above those corresponding to KH vortices. In consequence, KH vortices could still exist but be shadowed by other, more energetic, fluctuations.

To shed light on the last point, the PSD of the incoherent spanwise vorticity ω'_z is calculated at a location at the shear layer corresponding to $\xi = 0.12$ for all the cases simulated and shown in Fig. 6.18. Left, centre and right subfigures correspond to the lower, intermediate and higher amplitude of the inlet oscillation A_{in}, respectively. For each of them, the three frequencies are shown. The spectra for the steady inflow case are also shown in the three figures for reference.

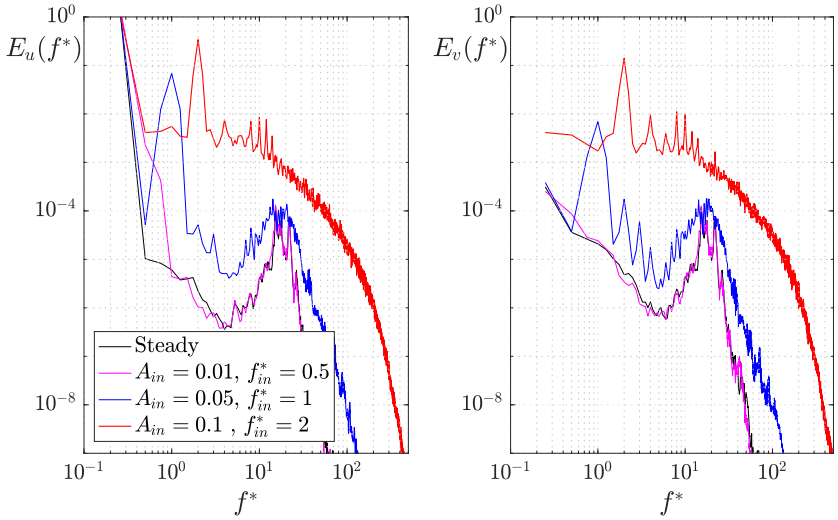

Figure 6.17: Power spectral density of the streamwise and wall normal velocity at Probe 4, $(x, y) = (0.2, 0.05)$.

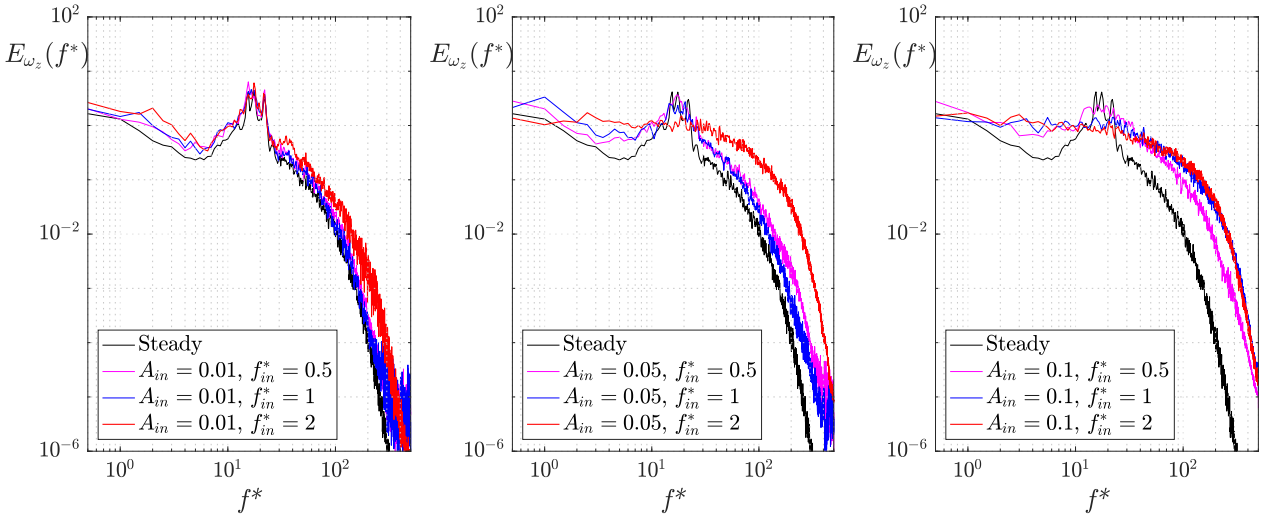

Figure 6.18: Power spectral density of the incoherent spanwise vorticity ω'_z at the shear layer, $\xi = 0.12$.

The spectra for the lower A_{in} cases (Fig. 6.18, left) are qualitatively identical, being dominated by KH vortices. Roughly the same amplitudes are obtained for the frequencies associated with the KH vortices for the three values of f^*_{in}, while the higher frequency range, corresponding to the turbulent cascade, is found to be slightly more energetic with increasing f^*_{in}. Conversely, the spectral for the intermediate A_{in} (Fig. 6.18, middle) shows qualitative changes that occur gradually as the inflow frequency f^*_{in} is increased. The amplitude of the KH narrowband peak is reduced while it is increased for all the other frequencies. For the largest inflow frequency, $f^*_{in} = 2$, the KH peak is not present anymore and the amplitude at the corresponding frequency is lower than for the cases with KH vortices. This shows that the regular KH vortex shedding is not shadowed by more energetic fluctuations, but rather eliminated. Individual KH vortices are still formed in the initial part of the separated shear layer, but in an irregular manner,

and they are not released from the recirculation bubble but trapped within it and quickly distorted by their interaction with the fine-grained turbulence. Finally, the spectral for the largest A_{in} (Fig. 6.18, right) follows the same trend as the intermediate A_{in} ones.

The changes observed in the PSD with increasing A_{in} and f^*_{in} are consistent with the vortex dynamics discussed in Section 6.4. As the large vortex cluster is formed, most of the vortical structures present in the separated shear layer get trapped in the recirculation region instead of being shed and advected downstream. Non-linear interactions between the recirculating structures lead to their merging and progressive breakdown into smaller structures, which leads to a more energetic and flatter spectral. In turn, the recirculation of random eddies of diverse scales prevents the formation of well-defined KH vortices in the separated shear layer.

6.6 Mode decomposition of oscillatory components

This section analyzes the results by decomposing the transient flow fields using Orthogonalized Variational Mode Decomposition (OVMD), with the aim of isolating phenomena that are coherent with the inflow oscillations. The data used are extracted and down-sampled from the simulations and consist of streamwise and wall-normal velocity snapshots spanning $x \in [-0.05, 0.45]$ and $y \in [0, 0.106]$ at the midspan of the domain, discretized into 191 and 37 data points, respectively. The sampling frequency, $f^*_s = 250 \times f^*_{in}$, exceeds the highest inflow frequency by two orders of magnitude and the KH shedding frequency by one order of magnitude.

The multivariate oscillatory component data coherent with the inflow frequency is defined as

$$\tilde{\mathbf{q}}(\phi) = \langle \mathbf{q} \rangle - \overline{\mathbf{q}}, \tag{6.10}$$

where $\langle \mathbf{q} \rangle$ represents the phase-averaged vector field, Eq. 6.4, comprising the spatial topology of both streamwise and wall-normal velocities, and $\overline{\mathbf{q}}$ denotes its time average. Consequently, the oscillatory flow component that is coherent with the inflow frequency, $\tilde{\mathbf{q}}(\phi)$, consists of 250 snapshots of $191 \times 37 = 7067$ pixels per velocity field (for a total of 14134 channels per snapshot, following the terminology introduced in Chapter 5). To improve the quality of the initial and final parts of the time series, the data have been symmetrically extended by padding segments from the beginning and end, resulting in a total of four periods of oscillation.

Multivariate POVMD is performed for the weakest, intermediate, and strongest inflow oscillations, representing each of the scenarios mentioned earlier. The intermediate case selected corresponds to $A_{\text{in}} = 0.1$ and $f^*_{\text{in}} = 1$. Each resulting mode, denoted by $\tilde{M}$ to avoid confusion with the Mach number M, comprises a temporal coefficient c and a spatial topology (ψ), as explained in Chapter 5. The decomposed modes include the spatial topologies for streamwise ψ_u and wall-normal velocity ψ_v. For brevity, the spatial topology is represented using the spanwise vorticity field ψ_{ω_z}, expressed by Eq. (5.24).

6.6.1 Weakest inflow oscillation: $A_{in} = 0.01,\ f^*_{in} = 0.5$

The energy ratios of the modes and their first fourteen dominant components are presented in Figs. 6.19-6.21. The energy ratio quantifies the total energy of the streamwise and wall-normal velocities of the modes relative to the input snapshots. It is defined as

$$E^*_i = \frac{c_i^2}{\|\tilde{\mathbf{q}}\|_F^2}, \tag{6.11}$$

where c_i is the temporal coefficient of mode-i and $\|\cdot\|_F^2$ denotes the squared Frobenius norm.

The energy of the fluctuation component $\tilde{\mathbf{q}}$, accounts for only approximately 0.2% of the total energy of the streamwise and wall-normal velocity, $\|\mathbf{q}\|_F^2$. The time-averaged component accounts for 97% of the energy, while the incoherent component $\mathbf{q}'$ represents approximately 2.8%. Most of the dynamics do not correlate with the inflow frequency, suggesting that the general behavior is qualitatively similar to the steady inflow case. Of this 0.2% energy, approximately 62% is distributed across fourteen modes, Fig. 6.19.

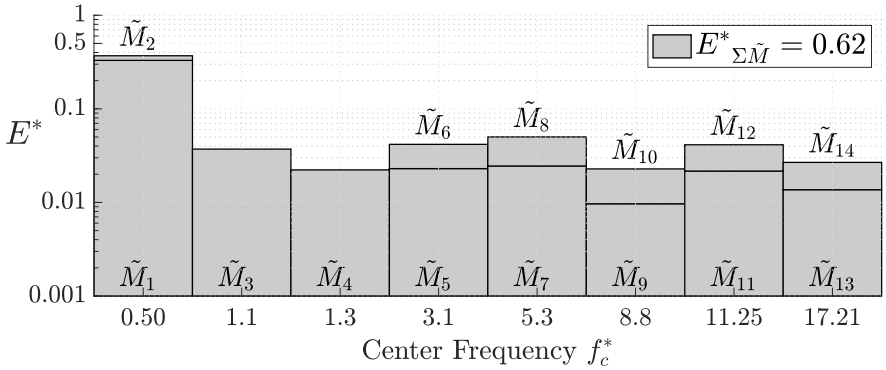

Figure 6.19: Energy ratio of modes for the weakest inflow fluctuation - $A_{in} = 0.01,\ f^*_{in} = 0.5$

The phase-averaged dynamics are predominantly characterized by a periodic vertical motion of the separated shear layer, represented by modes 1 and 2 in Fig. 6.20. Together, these modes account for approximately 40% of the phase-averaged fluctuation energy. The coupling of these modes and their division into two components arise from the phase lag between spatial locations, as described in Chapter 5. The movement of the separated shear layer is relatively weak, does not generate harmonics, and does not produce vortices as a result of its vertical motion.

The contribution of other modes is significantly smaller compared to modes 1 and 2. Modes 3 to 6 lack a distinctive vortical structure. This lack of coherence likely results from the phase-averaging process, which forces these modes to merge into certain frequencies.

The presence of Kelvin-Helmholtz (KH) vortices is evident in modes 13 and 14 (Fig. 6.21). However, these modes do not correspond to the actual KH vortices, as most of the data is in the incoherent component. Several modes with intermediate frequencies (modes 7 and 8, as well as modes 11 and 12) are generated, which might represent the nonlinear behavior of the fundamental KH vortices downstream and/or the inverse energy cascade (Biferale et al., 2012).

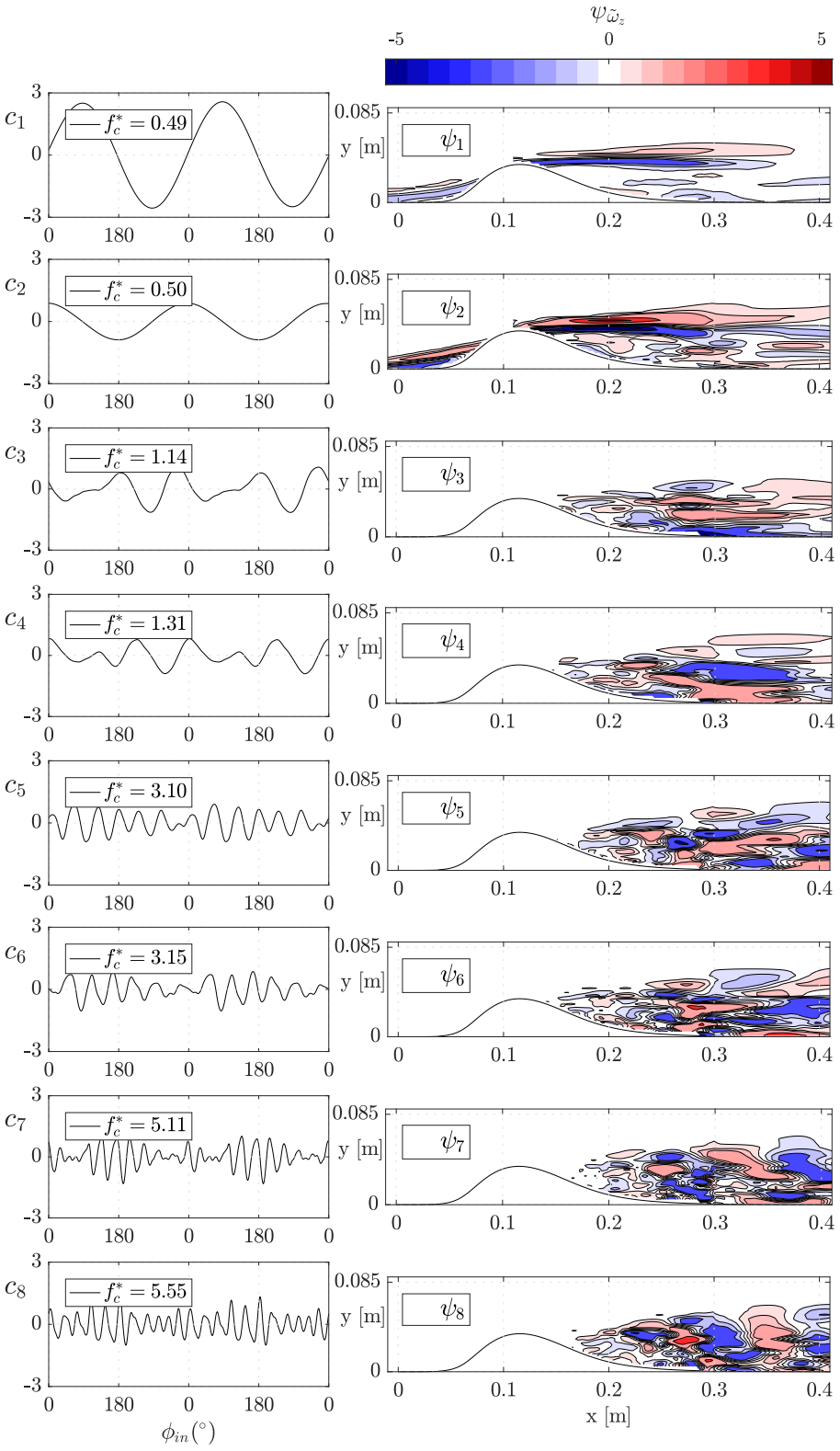

Figure 6.20: OVMD modes 1-8, represented by spanwise vorticity, for the Bump with $A_{in} = 0.01$, $f_{in}^* = 0.5$

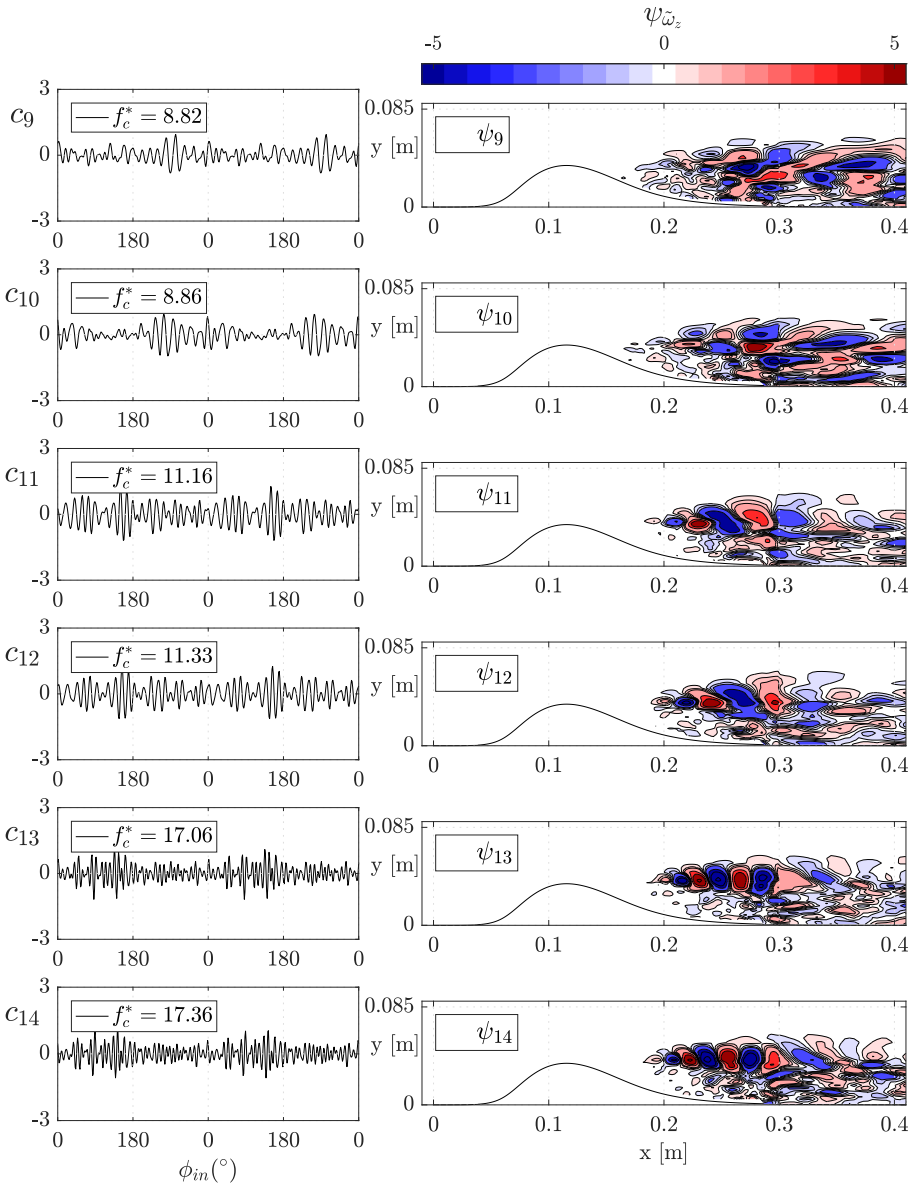

Figure 6.21: OVMD modes 9-14, represented by spanwise vorticity, for the Bump with $A_{in} = 0.01,\ f_{in}^* = 0.5$

6.6.2 Intermediate inflow oscillation: $A_{in} = 0.1,\ f_{in}^* = 1$

For the intermediate case selected, $A_{in} = 0.1,\ f_{in}^* = 1$, the energy ratios of the modes and the first twelve dominant modes are shown in Figs. 6.22–6.24. The fluctuations coherent with the inflow frequency accounts for 8.7% of the total energy, while the mean and incoherent components represent 88% and 3.3%, respectively. Hence, more than 70% of the fluctuations are coherent with the inflow oscillation, suggesting that the general behavior is different to the steady inflow case or the weakest inflow fluctuation. These coherent oscillations are represented by 12 modes, as shown in Fig. 6.22.

The dynamics are strongly driven by the inflow frequency, as shown by modes 1 and 2 in Fig.

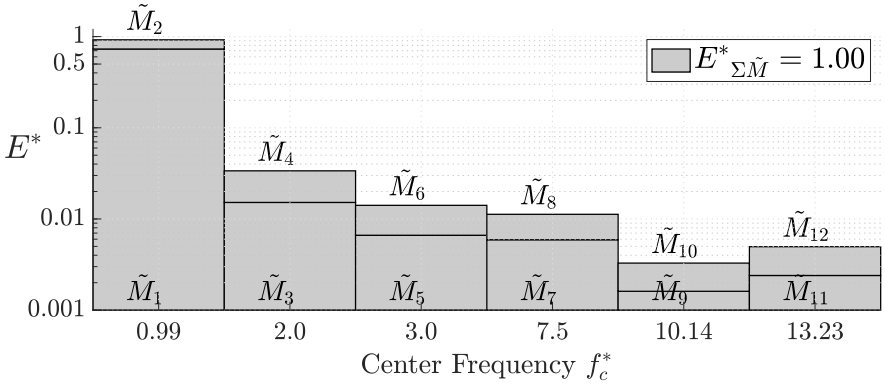

Figure 6.22: Energy ratio of modes for the intermediate inflow fluctuation - $A_{in} = 0.1,\ f_{in}^* = 1$

6.23. These modes account for approximately 90% of the fluctuations in the phase-averaged data and represent the vertical movement of the separated shear layer. This movement is more pronounced compared to the weakest inflow oscillation case; however, no large vortices are visible in these modes.

The second harmonic (modes 3 and 4) and the third harmonic (modes 5 and 6) capture the complex behavior of the vertical movement of the separated shear layer. Specifically, these modes illustrate how the separated shear layer shifts spatially at varying phases and speeds, contributing to the formation of large vortical structures. The large vortex formation becomes evident in the third harmonic modes. This behavior aligns with expectations, as vortex clusters predominantly appear during the end of the deceleration phase and the early stage of the acceleration phase (see Fig. 6.16 at $\phi_{in} = 252°$–$360°$). Outside of this period, the impact of the third harmonic, particularly in the large vortex region, is reduced and surpassed by the contributions from other modes.

The motion of the separated shear layer significantly alters the fundamental frequency of the Kelvin-Helmholtz (KH) vortices. The KH vortices appear only when the bulk velocity gradient is small, i.e., when the bulk flow transitions between acceleration and deceleration. These vortices are manifested as two phase-localized phenomena, represented by mode pairs 9-10 and 11-12.

At the end of the acceleration stage, when $\phi_{in} = 90°$, KH vortices are generated with a frequency f_c^* of approximately 13, corresponding to modes 11 and 12 in Fig. 6.24. These modes are accompanied by their subharmonic modes (modes 7 and 8), which induce vortex pairing. During this stage, the previous vortex cluster has been released downstream, while the formation of a new vortex cluster has not yet begun. Consequently, some of the vortex pairs are convected downstream and are not entrapped in the recirculation region, see Fig. 6.16 at $\phi_{in} = 72°$–$108°$. Once the new vortex cluster begins to form, the fundamental modes diminish, while the subharmonic modes decrease in both magnitude and frequency. These reductions slow the downstream flow and trap the vortices within the recirculation region until they are collectively released with the large vortex.

Towards the end of the deceleration stage, when $\phi_{in} = 270°$, KH vortices are generated with a frequency f_c^* of approximately 10, corresponding to modes 9 and 10. Before the release

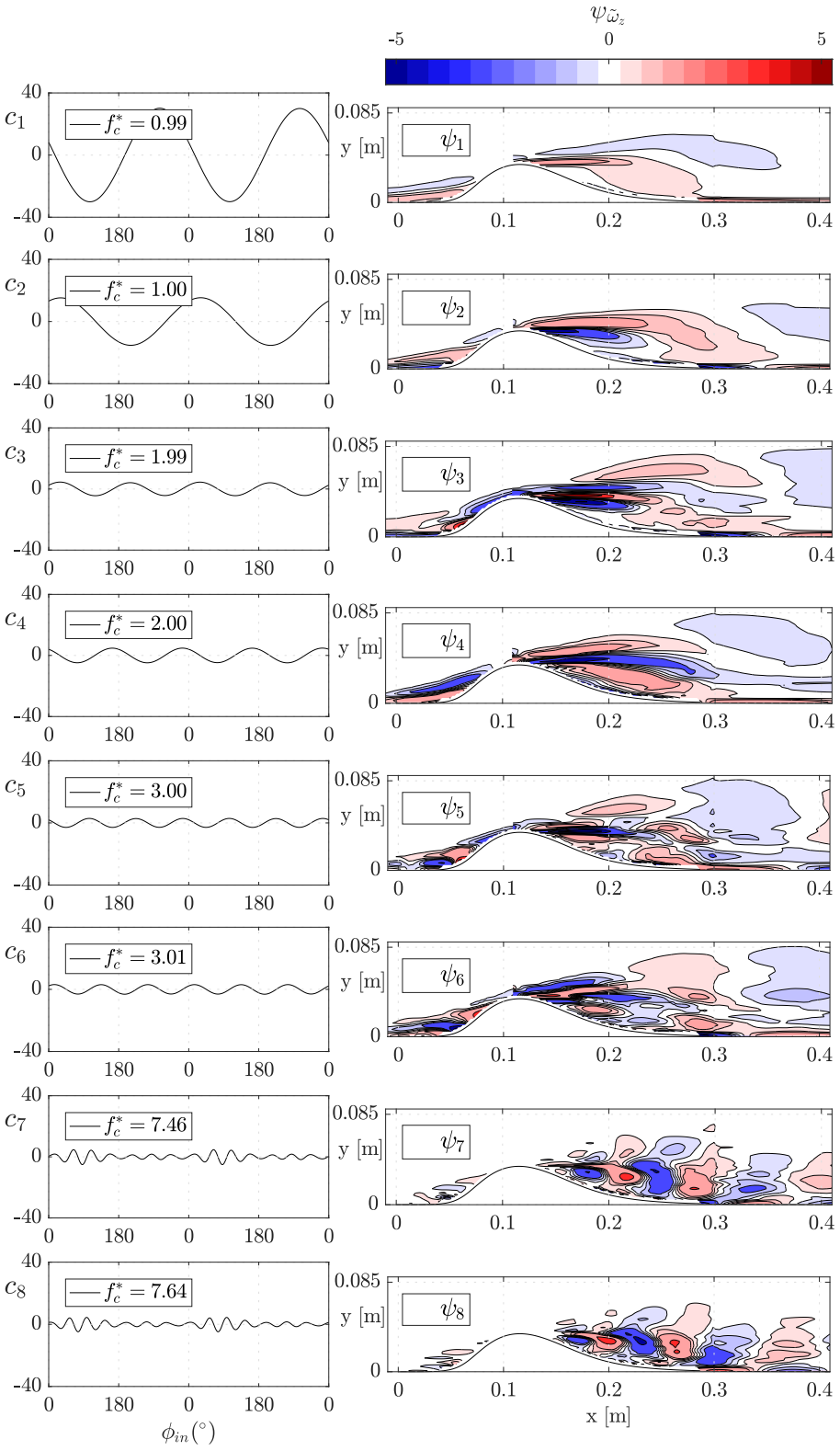

Figure 6.23: OVMD modes 1-8, represented by spanwise vorticity, for the Bump with $A_{in} = 0.1$, $f_{in}^* = 1$

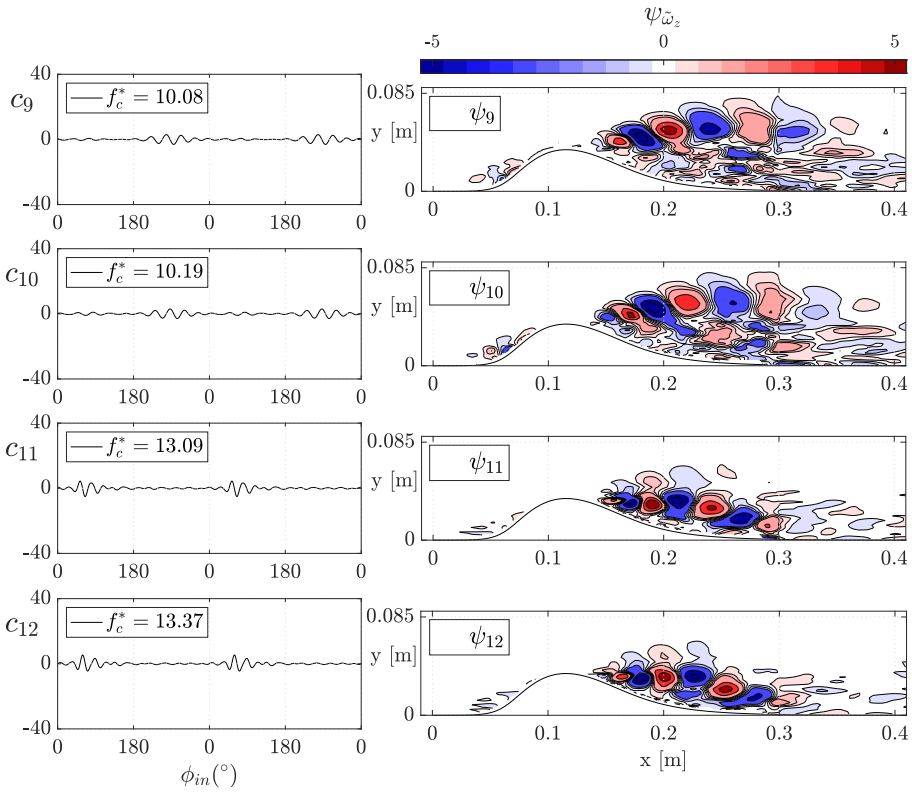

Figure 6.24: OVMD modes 9-12, represented by spanwise vorticity, for the Bump with $A_{in} = 0.1,\ f_{in}^* = 1$

of the large vortex cluster, these vortices remain trapped within the cluster. However, after the release, some of these vortices are convected downstream individually, as the process of forming a new vortex cluster has not yet begun, see Fig. 6.16 at $\phi_{in} = 288°$.

6.6.3 Strongest inflow oscillation: $A_{in} = 0.1,\ f_{in}^* = 2$

For the case of the strongest inflow fluctuation, $A_{in} = 0.1$ and $f_{in}^* = 1$, the energy ratios of the modes and the first fifteen dominant modes are presented in Figs. 6.25–6.27. Oscillatory data coherent with the inflow frequency accounts for approximately 9.5% of the total energy, while the mean flow and incoherent components contribute 87.5% and 3%, respectively. The energy associated with these coherent oscillations is distributed across fifteen modes, as illustrated in Fig. 6.22.

The dynamics are predominantly influenced by the inflow frequency, as indicated by modes 1 and 2 in Fig. 6.26. These modes contribute approximately 80% of the fluctuations in the phase-averaged data and correspond to the vertical motion of the separated shear layer. This motion is more pronounced than in the intermediate inflow case. Notably, these modes alone are sufficient to capture the periodic formation of a large vortex that is more intense and spans all inflow phases, as opposed to the intermediate inflow oscillation case.

The second harmonic (modes 3 and 4) and the third harmonic (modes 5 and 6) capture the

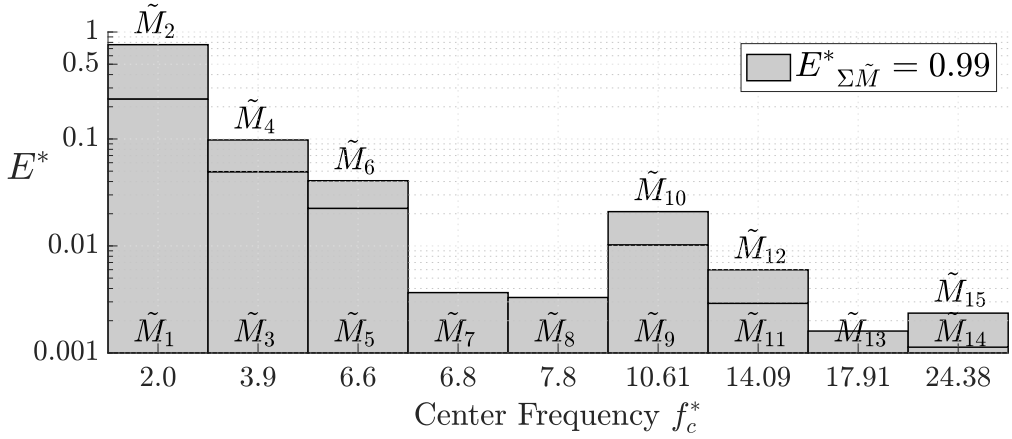

Figure 6.25: Energy ratio of modes for the strongest inflow fluctuation - $A_{in} = 0.1,\ f_{in}^* = 2$

intricate dynamics of the vertical motion of the separated shear layer, revealing how the separated shear layer oscillates spatially at varying phases and speeds to form the large vortex cluster. The third harmonic modes exhibit phase locality, becoming suppressed near the end of the deceleration phase and the early part of the acceleration phase ($\phi_{in} = 245°$–$360°$). This phase locality of the third-harmonic pair results in a slower advection of the large vortex cluster, allowing the reattachment point to remain farther upstream for a longer duration. The varying advection speed of the vortex cluster is evident from the phase-averaged reattachment points shown in Fig. 6.12. This phenomenon contributes to a more concentrated probability density function (PDF) with reduced skewness of the phase-averaged recirculation bubble length, as shown in Fig. 6.13.

Another mode pair appears as the third-harmonic modes weaken. Modes 7 and 8 have a different topology compared to the third harmonic and exhibit noticeable time coefficients during the early acceleration stage. These modes form a pair, as the phase difference and spanwise vorticity suggest that they appear as two modes due to phase lag in the spatial shape. The modes represent two phenomena: (i) the ejection of KH vortices from the separated shear layer into the large vortex cluster, and (ii) the mixing of multiple vortices within the vortex cluster to form a single, stronger cluster. The mixing of vortices in the large vortex cluster distinguishes this case from previous ones and plays a crucial role in creating a more intense and compact vortex, resulting in a significant reduction in mean separation length. This mixing also effectively increases the root-mean-square velocity within the recirculation region (Fig. 6.6).

At the transition from the acceleration stage to the deceleration stage, when $\phi_{in} = 0 - 180°$, KH vortices are generated with a frequency f_c^* of approximately 14, corresponding to modes 11 and 12 in Fig. 6.27. These modes are accompanied by their second harmonic modes (modes 14 and 15) as well as other intermediate-frequency modes: modes 9-10 (lower than the fundamental frequency) and mode 13 (higher than the fundamental frequency). Most of the generated vortices are entrapped in the recirculation region as the process of creating a new vortex cluster begins. The energy cascade, along with modes 7 and 8, later contributes to the mixing process within the vortex cluster.

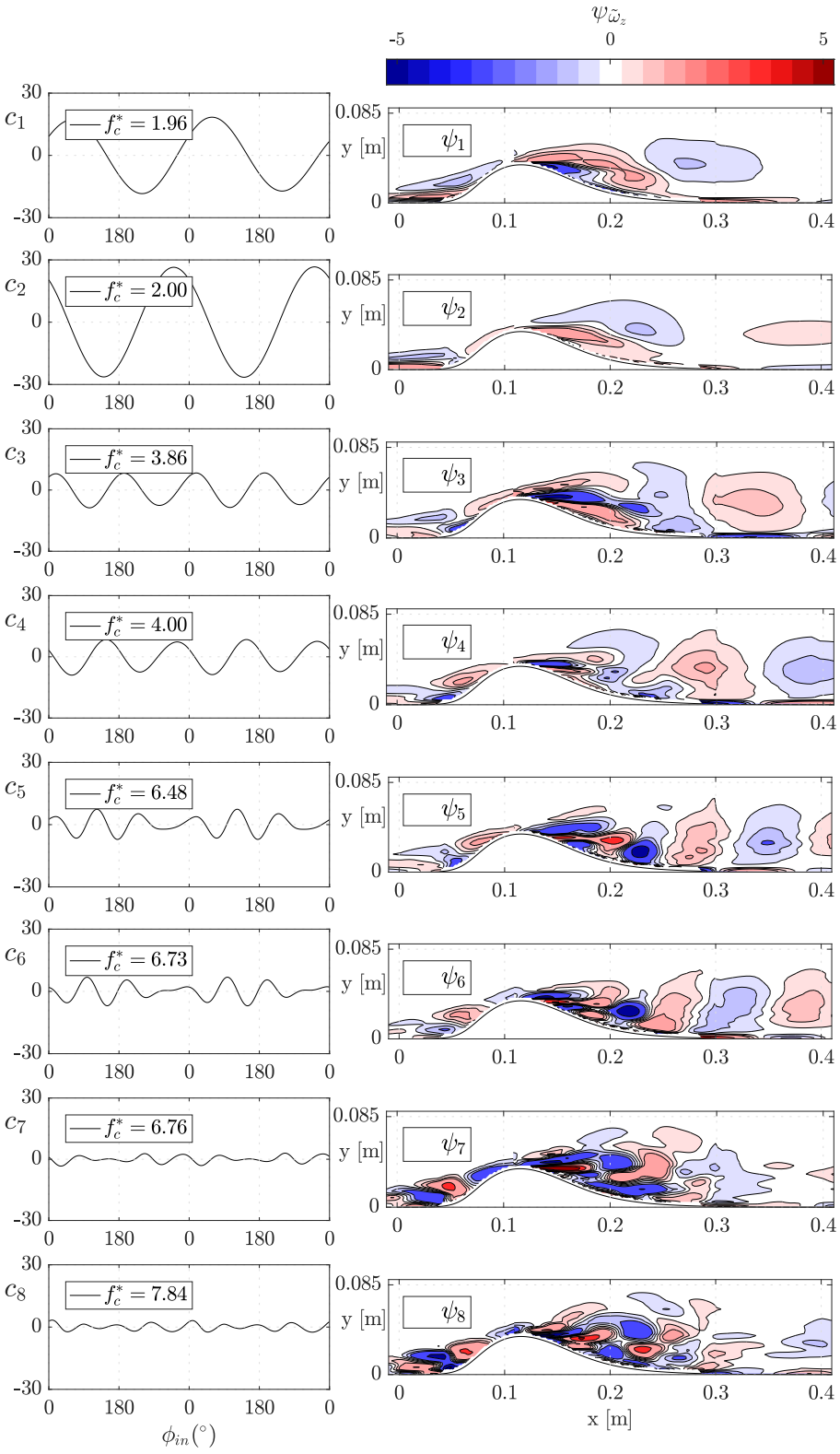

Figure 6.26: OVMD modes 1-8, represented by spanwise vorticity, for the Bump with $A_{in} = 0.1$, $f_{in}^* = 2$

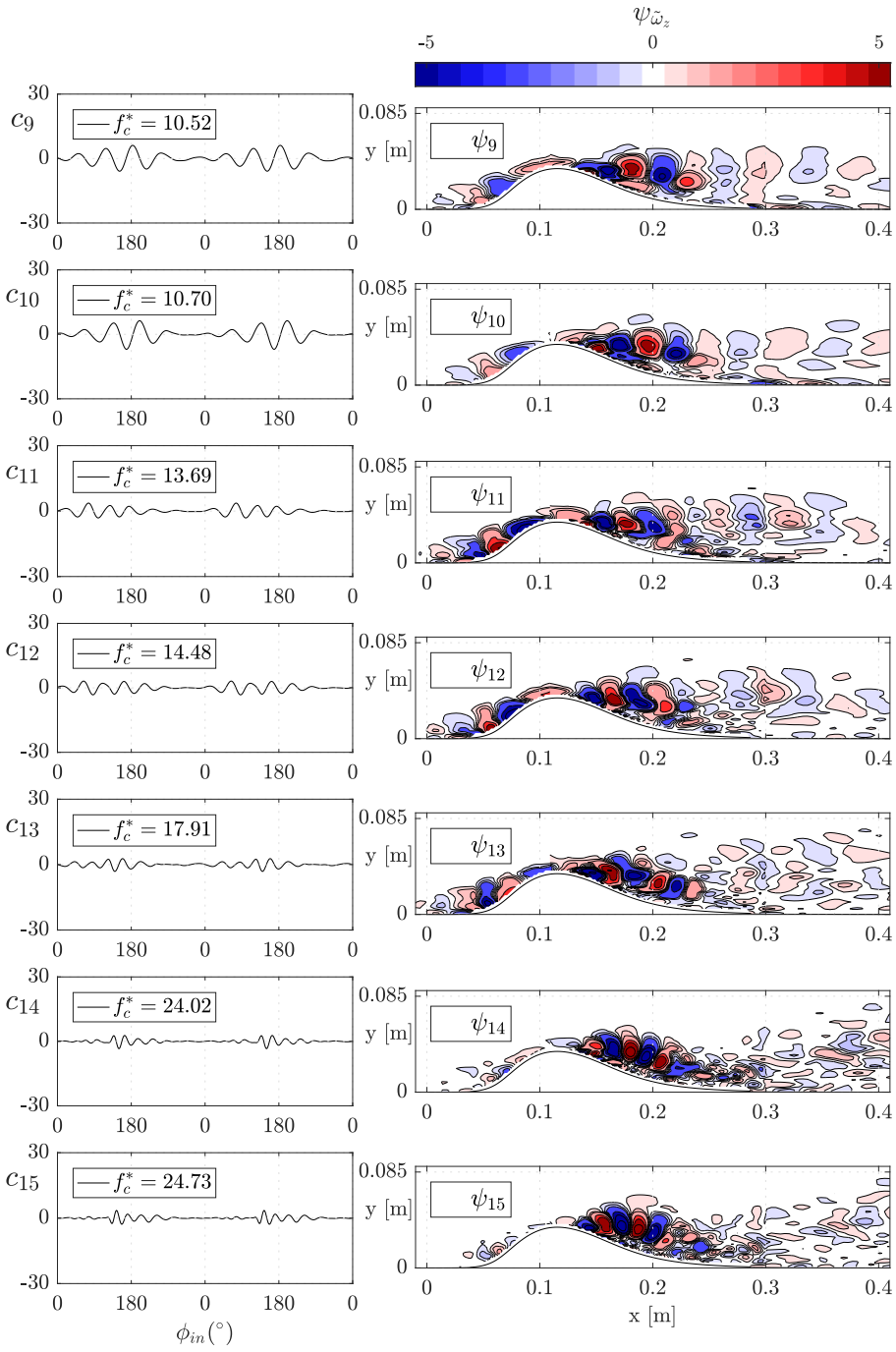

Figure 6.27: OVMD modes 9-15, represented by spanwise vorticity, for the Bump with $A_{in} = 0.1$, $f_{in}^* = 2$

6.7 Classification of the harmonic inflow cases

Table 6.3 shows the correspondence between the simulated cases and the scenario observed for the vortex dynamics. This classification is based on cross-comparing the time histories of the phase-averaged streamwise acceleration parameter (Fig. 6.11), the incoherent spanwise

vorticity along the phase-averaged shear layer (Fig. 6.15), the PDFs of the phase-averaged length of the separated flow region (Fig. 6.13), the frequency spectra 6.18, and the OVMD modes Section 6.6. For reference, the evolution of the three-dimensional flow represented as in Fig. 6.16 is also checked.

Table 6.3: Classification of the cases. Minimum values of the time-averaged and phase-averaged streamwise acceleration parameter and reduction of the time-averaged length of the separated flow region. The first row corresponds to the steady inflow case

A_{in}	f^*_{in}	$A_{in}f^*_{in}$	$< K >_{min}$ $\times 10^{-6}$	$< K_{\partial u/\partial x} >_{min}$ $\times 10^{-6}$	$< K_{\partial u/\partial t} >_{min}$ $\times 10^{-6}$	$\Delta L_s/L_{s,steady}$	Scenario
0.01	0.5	0.005	-12.44	-13.22	-2.37	0	(i)
0.01	1	0.01	-13.60	-13.96	-2.44	-0.0007	(i)
0.01	2	0.02	-22.43	-24.45	-4.51	-0.0564	(ii)
0.05	0.5	0.025	-16.71	-16.04	-6.46	-0.0198	(i)
0.05	1	0.05	-24.74	-22.20	-11.53	-0.0654	(ii)
0.05	2	0.1	-36.12	-39.93	-22.87	-0.2933	(iii)
0.1	0.5	0.05	-23.34	-22.75	-12.82	-0.0744	(ii)
0.1	1	0.1	-36.44	-36.14	-22.61	-0.1650	(ii)
0.1	2	0.2	-53.37	-50.99	-40.87	-0.4490	(iii)

The table shows, for each simulated case, the minimum values of the acceleration parameter for the corresponding time-averaged flow $\bar{K}$, the phase-averaged flow $\langle K \rangle$ and its two components. The time-averaged values are considerably lower than the phase-averaged ones and are not useful in the classification of the cases. The minimum of $\langle K \rangle$ decreases independently with the amplitude and frequency of the inlet oscillations. The convective acceleration $\langle K_{\partial u/\partial x} \rangle$ dominates for low A_{in} and/or f^*_{in} values. As a rough approximation, the temporal acceleration $\langle K_{\partial u/\partial t} \rangle \sim A_{in}f^*_{in}$, and this component becomes comparable to the convective acceleration for the largest values of the product $A_{in}f^*_{in}$.

The resulting classification can be illustrated through three different scenarios, as shown in Fig. 6.28. Scenario (i) corresponds to weak inflow oscillations, resulting in a minimal reduction of the mean recirculation length. Scenario (iii) involves the periodic formation of vortex clusters, leading to a significant reduction in the mean recirculation length. A detailed discussion of each scenario will be provided in Chapter 8.

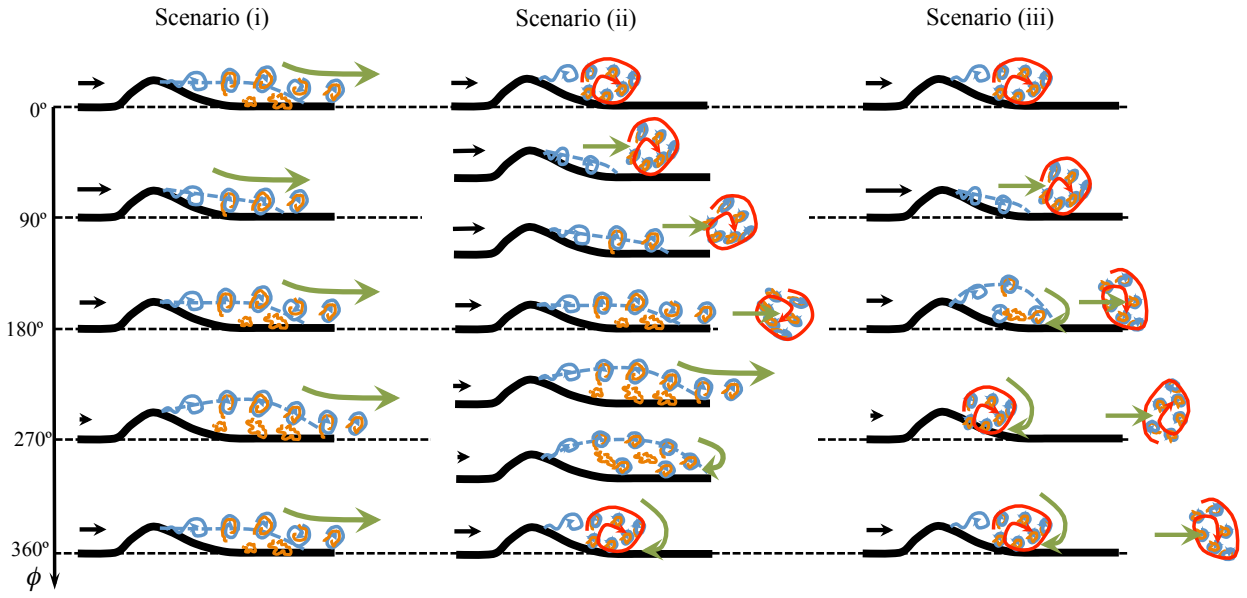

Figure 6.28: Descriptive illustrations of the three scenarios. Dashed blue lines: phase-averaged separation streamline; solid blue: KH vortices; orange: small-grained vorticity; red: vortex cluster; green arrows show the instantaneous trajectory of the flow structures

This page is intentionally left blank

Chapter 7

Impact of a 2D synthetic jet on the size and dynamics of the separated flow over a bump in laminar and turbulent inflow

In this chapter, active flow control strategies employing synthetic jets are implemented to reduce the separation length for both steady laminar inflow and turbulent inflow. Synthetic jets, which operate as zero-net mass-flux systems with periodic blowing and suction, are the focus of the study. Research by Sigurdson (1995) and Kiya et al. (1997) indicates that the optimal actuation frequency lies between 2 and 5 times the shedding frequency. The proposed scaling for the shedding frequency is expressed as a function of the half-width of the wake h and the separation velocity, characterized by the Strouhal number $St_h = f_{shed}\ h/U_s \approx 0.07 - 0.08$.

This chapter examines this hypothesis, proposes an alternative actuation strategy, and performs OVMD decomposition to investigate the underlying physics.

7.1 Flow configuration

The study is conducted using an identical domain and setup as described in Chapter 3. This domain is discretized into high-order meshes for two configurations: 63,864 elements for laminar inflow simulations and 192,000 elements for turbulent inflow simulations. The high-order mesh for the laminar inflow configuration is illustrated in Fig. 7.1. Compared to the setup in Chapter 3.1, this mesh features a higher density of elements near the walls and in the spanwise direction to capture more complex wall-bounded structures. The turbulent inflow mesh is identical to that in Chapter 3.2, as shown in Fig. 3.11. A third-order polynomial is used for all simulations, resulting in 4,087,296 Degrees of Freedom (DOF) for the laminar inflow and 12,288,000 DOF for the turbulent inflow. The numerical schemes used are identical to those described in Chapter 2, with a constant time step corresponding to a CFL number

< 0.8.

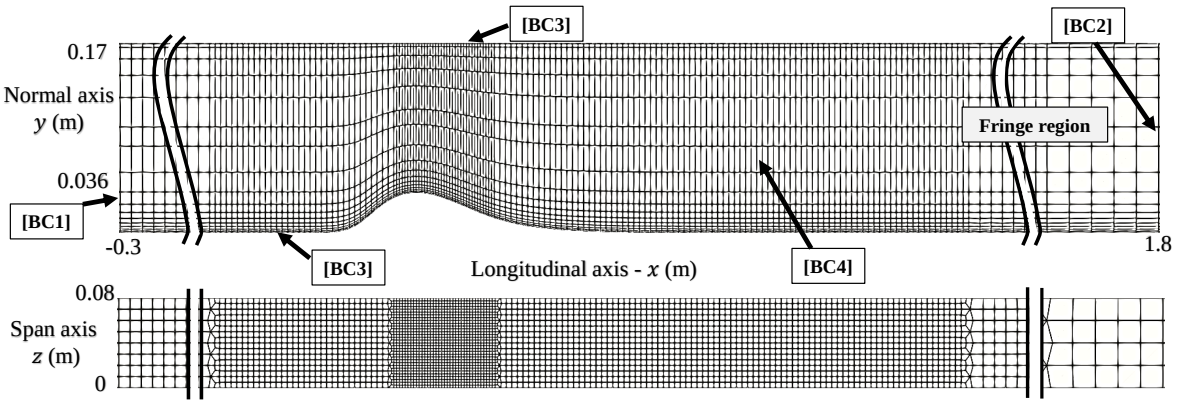

Figure 7.1: Computational domain and representative mesh for study with laminar inflow in this chapter

The boundary conditions are similar to Tables 3.1 and 3.4 for the laminar and turbulent inflow setups, respectively. Recall that this configuration corresponds to $Re/L \approx 100,000$ or $Re_{h_{bump}} = 3,600$ and $M = 0.2$, with a reference velocity of $U_{Ref} = 68.158$ m/s. For the laminar inflow, the characteristic Reynolds numbers based on the separation length and the momentum thickness at separation are $Re_{L_s} = 27,000$ and $Re_{\theta,s} = 27$. For the turbulent inflow, these values are $Re_{L_s} = 28,900$ and $Re_{\theta,s} = 22$.

7.1.1 Synthetic jet actuation

A synthetic jet is applied at a location from $x = 0.1025$ m to $x = 0.1075$ m and extended in the spanwise direction to induce a two-dimensional disturbance. This location is just upstream of the separation point, as illustrated in Figure 7.2. An analytical solution to oscillatory Poiseuille flow, assuming two-dimensional incompressible flow, is imposed as a Dirichlet boundary condition. It ensures a zero-net mass-flux and maintains a continuous velocity profile in the longitudinal direction. The synthetic jet is ejected vertically and described as (Ma and Kuo, 2017):

$$v(x,t) = A_{jet}\; i \left\{ 1 - \frac{\cosh\left[\zeta / h_{jet}\,(1+i)\,|x - x_{c,jet}|\right]}{\cosh\left[\zeta\,(1+i)\right]} \right\} \left\{ \Im \left(\frac{\cosh\left[\zeta\,(1+i)\right]}{\cosh\left[\zeta\,(1+i)\right] - 1} \right) \right\} e^{i\omega_{jet}(t^* - t_0^*)} \tag{7.1}$$

$$u(x,t) = w(x,t) = 0 \tag{7.2}$$

$$p(x,t) = \bar{p}(x)_{no\ jet}, \tag{7.3}$$

where $i = \sqrt{-1}$, $\Im$ denotes the imaginary component, A_{jet} is the amplitude of the synthetic jet velocity relative to the reference velocity $A_{jet} = v_{jet,max}/U_{Ref}$, $h_{jet} = 0.0025$ m is the half-width of jet slot, $x_{x,jet} = 0.105$ m is the centerline of the jet slot, $t^* = tU_{Ref}/L_{Ref}$ is the

dimensionless time, and t_0^* is a reference instant. The non-dimensional parameter ζ is defined as

$$\zeta = h_{jet}\sqrt{\omega_{jet}/2\nu}, \tag{7.4}$$

where ω_{jet} is the angular frequency of actuation $\omega_{jet} = 2\pi f_{jet}^*$ and $f_{jet}^* = f_{jet}\ L_{Ref}/U_{Ref}$ is the dimensionless frequency of the actuation. The reference length L_{Ref} is 1 m as defined in Chapter 3.

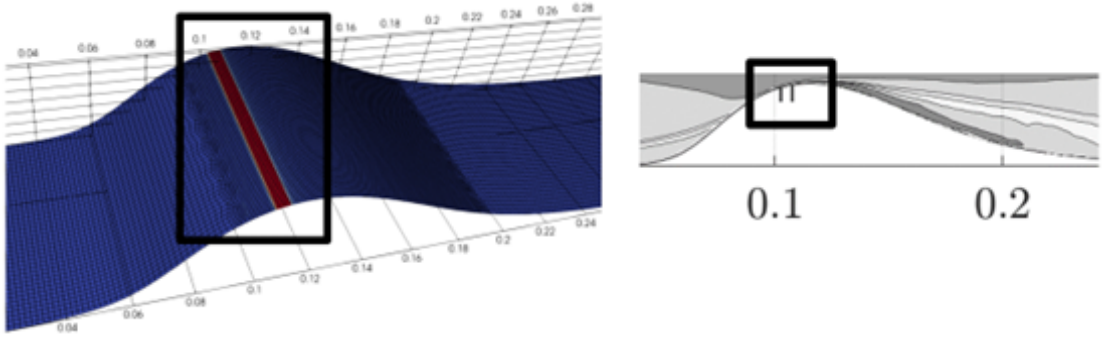

Figure 7.2: Location of synthetic jet boundary condition

7.1.2 Actuation strategies

The first strategy involves periodic blowing and suction, characterized by A_{jet} and f_{jet}^*, as previously described. One of the objectives of this study is to test the hypothesis of Sigurdson (1995), which suggests that the range of f_{jet}^* should extend from 2 to 5 times the shedding frequency (f_{shed}^*).

For the steady laminar inflow case, the shedding frequency is approximately $f_{shed}^* = 2.9$–3.3, with $h \approx h_{bump}$. The value of $f_{shed}^* = 2.6$ is selected based on the OVMD decomposition of the steady inflow, as detailed in Appendix E. In the turbulent inflow case, the streamwise velocity at the separation point U_s is lower than that of the laminar case, as shown in Fig. 3.15. Consequently, the shedding frequency is approximately $f_{shed}^* = 2.6$–3.0, with a value of $f_{shed}^* = 2.6$ again chosen based on the OVMD decomposition (Appendix E).

To effectively span the range of 2 to 5 times the shedding frequency, the following integer frequencies are selected: $f_{jet}^* = \{2, 8, 12, 15, 16, 20\}$. Two amplitudes, $A_{jet} = \{0.04, 0.2\}$, are chosen to align with the range of experimental conditions reported in Sigurdson (1995). Figure 7.3 illustrates the normal velocity profile across the longitudinal location at various jet phase instances (ϕ_{jet}) for $A_{jet} = 0.2$, $f_{jet}^* = 2$, and $\zeta = 0.24$.

The second strategy consists of periodic blowing and suction followed by a delay interval without actuation. This approach introduces two additional parameters: the *duty ratio* D and the *duty frequency* f_D^*. The duty ratio is defined as the ratio of the active jet time to the inert (inactive) time and is given by:

$$D = \frac{\Delta t_{jet}}{\Delta t_{int}}. \tag{7.5}$$

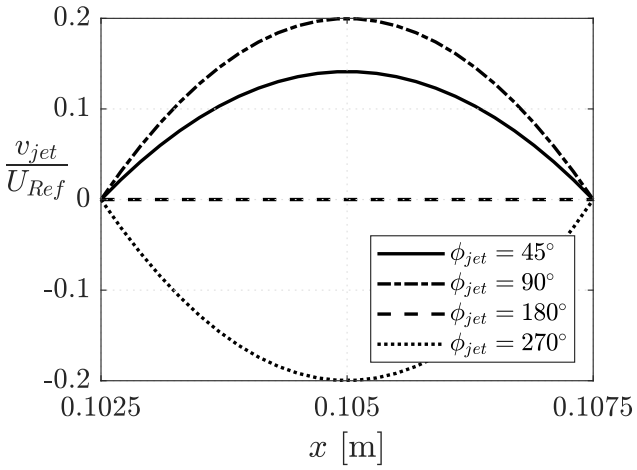

Figure 7.3: The normal velocity profile on the jet boundary at different jet phase instances for $A_{jet} = 0.2,\ f^*_{jet} = 2, \zeta = 0.24$

The duty frequency f^*_D is defined as the frequency of the duty cycle within one normalized time t^*. For this study, a duty ratio of $D = 1$ is selected, along with duty frequencies $f^*_D = \{1, 2\}$. Fig 7.4 presents the normal velocity on the jet centreline at different duty phases ϕ_D with a duty ratio $D = 1$, $f^*_D = 1$, $A_{jet} = 0.2$, and $f^*_{jet} = 16$.

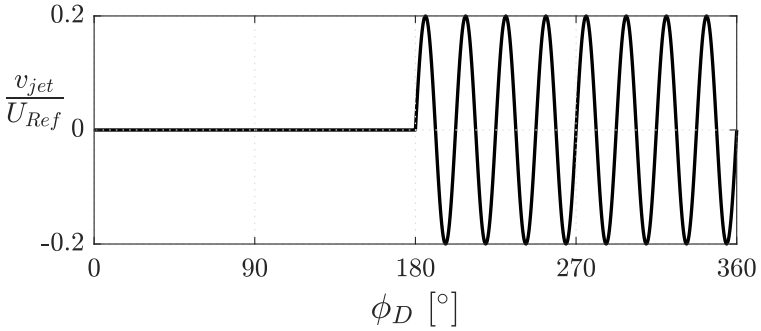

Figure 7.4: The normal velocity on the jet centerline at different duty phases (ϕ_D) for actuation strategy II with a duty ratio $D = 1$, $f^*_D = 1$, $A_{jet} = 0.2$, and $f^*_{jet} = 16$

7.2 Results

7.2.1 Strategy I: Alternating blowing and suction actuation

Table 7.1 presents the DNS simulations conducted using actuation strategy I. The dataset comprises 20 simulations, including two cases without actuation for each inflow condition and 18 cases with synthetic jet actuation. For the laminar inflow condition, two actuation amplitudes (0.04 and 0.2) are implemented. The dimensionless actuation frequency spans 2 to 20, corresponding to approximately 0.8 to 7.7 times the shedding frequency. The lowest frequency $f^*_{jet} = 2$ targets the shedding instability, whereas the higher frequencies align

with the Kelvin-Helmholtz instability. These actuation frequencies correspond to reduced frequencies based on the separation region length without control, $F^{+}_{L_s}$, which ranges from 0.5 to 5.8. These values are comparable to those reported in previous studies by Dandois et al. (2007), Greenblatt, Paschal, Yao, and Harris (2006), and Kiya et al. (1997).

Table 7.1: Summary of the cases simulated for actuation strategy I, including the amplitude and frequency of jet actuation, its frequency ratio to the shedding frequency f^{*}_{shed}, reduced frequency $F^{*}_{L_s}$, momentum coefficient C_μ, and stagnation pressure loss coefficient Y_{p_t}. The location of mean separation and reattachment are given along with the length of recirculation region L_s and the relative reduction to the unforced case ΔL_s.

Inflow	A_{jet}	f^{*}_{jet}	f^{*}_{jet}/f^{*}_{shed}	$F^{+}_{L_s}$	C_μ 10^{-4}	x_s (m)	x_r (m)	L_s (m)	ΔL_s (m)	Y_{p_t}
laminar	-	-	-	-	-	0.109	0.387	0.278	-	0.34
turbulent	-	-	-	-	-	0.116	0.404	0.289	-	0.35
laminar	0.04	2	0.8	0.56	0.14	0.115	0.364	0.249	-0.030	0.32
	0.04	8	3.1	2.23	0.14	0.114	0.314	0.200	-0.078	0.31
	0.04	12	4.6	3.34	0.14	0.115	0.302	0.187	-0.091	0.30
	0.04	15	5.8	4.17	0.14	0.116	0.326	0.210	-0.068	0.30
	0.04	16	6.2	4.45	0.14	0.113	0.321	0.208	-0.070	0.30
	0.04	20	7.7	5.56	0.14	0.112	0.318	0.206	-0.073	0.30
laminar	0.2	2	0.8	0.56	3.5	0.118	0.337	0.219	-0.059	0.33
	0.2	8	3.1	2.23	3.5	0.117	0.290	0.173	-0.105	0.27
	0.2	12	4.6	3.34	3.5	0.117	0.268	0.151	-0.128	0.22
	0.2	15	5.8	4.17	3.5	0.117	0.259	0.141	-0.137	0.20
	0.2	16	6.2	4.45	3.5	0.117	0.259	0.141	-0.137	0.20
	0.2	20	7.7	5.56	3.5	0.116	0.296	0.180	-0.098	0.23
turbulent	0.2	2	0.8	0.58	3.5	0.118	0.357	0.238	-0.050	0.34
	0.2	8	3.1	2.31	3.5	0.119	0.292	0.173	-0.116	0.25
	0.2	12	4.6	3.47	3.5	0.118	0.285	0.167	-0.122	0.24
	0.2	15	5.8	4.33	3.5	0.118	0.294	0.176	-0.113	0.24
	0.2	16	6.2	4.62	3.5	0.118	0.306	0.189	-0.100	0.24
	0.2	20	7.7	5.78	3.5	0.117	0.317	0.199	-0.089	0.24

Moreover, to facilitate comparisons with the aforementioned studies, the phase-averaged momentum coefficient, C_μ, is provided for all cases, defined as:

$$C_\mu = \frac{\rho_{jet}\ 2h_{jet} < v^2_{jet} >}{\rho_\infty\ c_{bump}\ U^2_\infty}, \tag{7.6}$$

where $\rho_{jet} \equiv \rho_\infty$, c_{bump} represents the equivalent chord length for the modeled LPT blade (i.e, the length of the convex region of the bump, which is 0.1 m), and the freestream velocity U_∞ is taken as the reference velocity U_{Ref}. The phase-averaged square of the jet velocity,

$< v_{jet}^2 >$, is calculated as:

$$< v_{jet}^2 >= \frac{\int\int v_{jet}^2(x,\phi)\ dx\ d\phi}{\int\int dx\ d\phi}. \tag{7.7}$$

The values of the jet amplitude and the momentum coefficient are within the range of those reported in Greenblatt, Paschal, Yao, and Harris (2006), Kiya et al. (1997), and Sigurdson (1995), and smaller than those in the study by Dandois et al. (2007), as shown in Table 7.2.

Table 7.2: Comparison of jet amplitude and momentum coefficient with those from other reference studies

Reference	A_{jet}	C_μ 10^{-4}	h_{jet} mm
present	0.04 - 0.2	0.14 - 3.5	2.5
Sigurdson, 1995	0.04 - 0.24	-	3.2
Kiya et al., 1997	0.005-0.2	-	1.25
Greenblatt, Paschal, Yao, and Harris, 2006	0.12-0.6	1-300	~ 0.9
Dandois et al., 2007	0.5	10	1.67

For each case, the separation and reattachment locations are identified, and the length of the separation region is determined by calculating the difference between these two points. These locations are obtained from the zero-crossing of the skin friction coefficient in the mean flow field, averaged over time and the spanwise direction. In cases with actuation, the reduction in the separation region length is quantified relative to the corresponding no-actuation case for the given inflow condition. Time-averaged quantities are computed from datasets sampled at every time step, with a time span of $t^*_{data} \geq 12$ for the laminar inflow and $t^*_{data} = 9$ for the turbulent inflow.

The final parameter presented in Table 7.1 is the stagnation pressure loss coefficient. This parameter quantifies the flow characteristics that contribute to the overall efficiency reduction, as described by Denton (1993). It is defined as the difference between the inlet and outlet total pressure, normalized by the dynamic pressure at the outlet. In this study, the inlet corresponds to the transverse plane at the longitudinal location $x = -0.1$ m, while the outlet corresponds to $x = 0.4$ m. The stagnation pressure loss coefficient is expressed as:

$$Y_{p_t} = \frac{\overline{p}_{t,@x=-0.1} - \overline{p}_{t,@x=0.4}}{\overline{p}_{t,@x=0.4} - \overline{p}_{@x=0.4}}. \tag{7.8}$$

The transverse plane extends from the bottom wall to the top wall; consequently, the parameter also accounts for losses from the top wall boundary layer.

The introduction of a disturbance just upstream of the separation point shifts the separation region slightly downstream. This also influences the reattachment location, thereby reducing the size of the recirculation region across the tested amplitude and frequency ranges. The maximum reduction occurs at a dimensionless actuation frequency of 12 for $A_{jet} = 4\%$, increasing to 16 for $A_{jet} = 20\%$ under laminar inflow conditions. For turbulent inflow

conditions with $A_{jet} = 20\%$, the maximum reduction is observed at $f^*_{jet} = 12$. These frequencies correspond to 4.6 to 6.2 times the shedding frequency, aligning with the range of optimal frequencies identified in the study by Sigurdson (1995). The frequency that results in the shortest separation region also corresponds to the minimum stagnation pressure loss coefficient.

The reduction in the separation region length, relative to the uncontrolled case, as a function of the actuation frequency range is shown in Fig. 7.5. At the optimum frequency, the reduction in the separation region is approximately 33% for $A_{jet} = 4\%$ and 49% for $A_{jet} = 20\%$ under laminar inflow conditions. For an amplitude of $A_{jet} = 20\%$ with turbulent inflow conditions, the maximum measured reduction is 42% compared to the no-actuation case with turbulent inflow.

A comparison of the reductions under laminar inflow for the two different forcing amplitudes confirms the logarithmic dependence of the maximum reduction in separation length on the amplitude, as suggested by Kiya et al. (1997). This relationship is expressed as:

$$\frac{|\Delta L_{s,max}|}{(L_s)_{no\ jet}} \sim b_1 + b_2 \ln(A_{jet}) \sim c_1 + c_2 \ln(\sqrt{C_\mu}), \tag{7.9}$$

where $b_{1,2}$ and $c_{1,2}$ are constants.

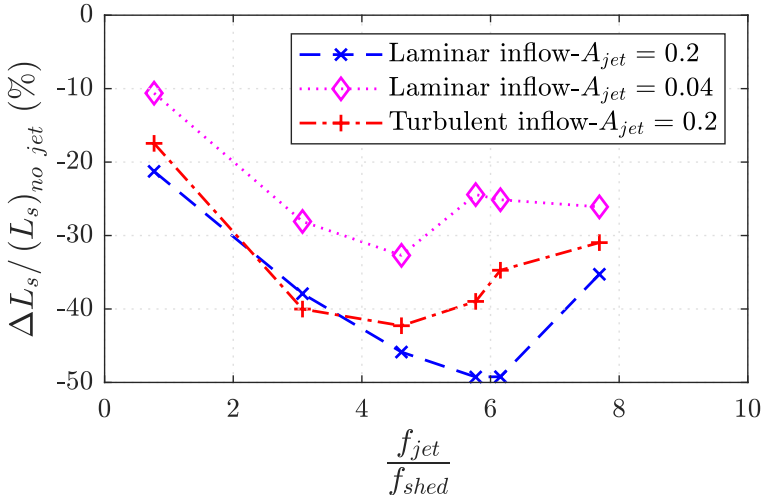

Figure 7.5: Percentage reduction of recirculation region normalized with the recirculation length without actuation

Furthermore, by normalizing the length reduction ΔL_s with its maxima over all actuation frequencies, a frequency sensitivity map can be constructed, as shown in Fig. 7.6. The results converge into a similar trend across all setups and show good agreement with Sigurdson (1995). The cases analyzed have comparable Re_h, f_{KH}/f_{shed} and C_μ values to those in Sigurdson (1995). Fig. 7.6 indicates that forcing frequencies around 3–6 times the shedding frequency yield reductions close to the optimum frequency, with only minor differences. In this regime, the KH instability, which scales with the momentum thickness of the shear layer, amplifies the impact of the forcing (Sigurdson, 1995). This may explain why the results for laminar

and turbulent inflows show good agreement, as the momentum thickness for the unforced case is relatively similar for both conditions.

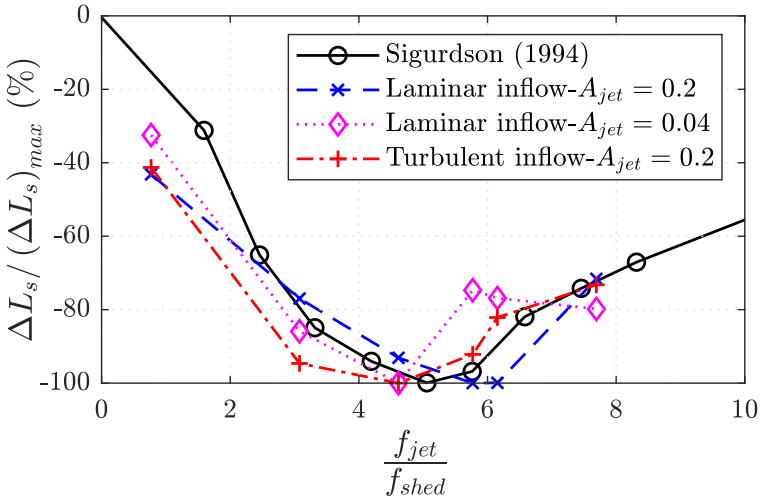

Figure 7.6: Percentage reduction of recirculation region normalized with maximum reduction

Instantaneous flow fields

Figures 7.7 and 7.8 depict the instantaneous spanwise vorticity fields for laminar inflow under actuation with an amplitude of $A_{jet} = 20\%$ and nondimensional frequencies of 2 and 16, respectively. The frequency $f^*_{jet} = 2$ corresponds to cases where $f^*_{jet} = \mathcal{O}(f^*_{shed})$, while $f^*_{jet} = 16$ represents the optimum actuation frequency, situated within the range $f^*_{shed} < f^*_{jet} < f^*_{KH}$. The arrows indicate the state of the synthetic jet (blowing or suction), with their length representing the magnitude. Each figure consists of eight subfigures, representing jet phases with $\phi_{jet} = \{0, 45, 90, \ldots, 315\}^\circ$, arranged in increasing order corresponding to the indicated time (t^*).

In Fig. 7.7 for $f^*_{jet} = \mathcal{O}(f^*_{shed})$, a periodic generation of a large vortex cluster, consisting of smaller vortices, is observed. This cluster pulls fluid together in the recirculation region, resembling the structures induced by inflow fluctuations (see Chapter 6). The formation of the large vortex cluster begins with the vertical movement of the separated shear layer in phase with the synthetic jet. During the blowing phase, the shear layer moves toward the wall, whereas during the suction phase, it moves further away. Consequently, the small vortices generated by KH instability become trapped and form a vortex cluster, which is then ejected downstream during the blowing phase. This behavior is consistent with the turbulent inflow case, which is discussed in the Appendix E for brevity.

For the optimum forcing frequency, where $f^*_{shed} < f^*_{jet} < f^*_{KH}$, as shown in Fig. 7.8, different observations emerge. A dominant spanwise vortex forms periodically because of the interaction of the synthetic jet with the local boundary layer and/or shear layer. This vortex travels downstream near the bump's surface, merging with other vortices in the recirculation region. These periodic formation of spanwise vortices, which are in phase with the synthetic jet, effectively break the separated shear layer down and reduce the recirculation region, while

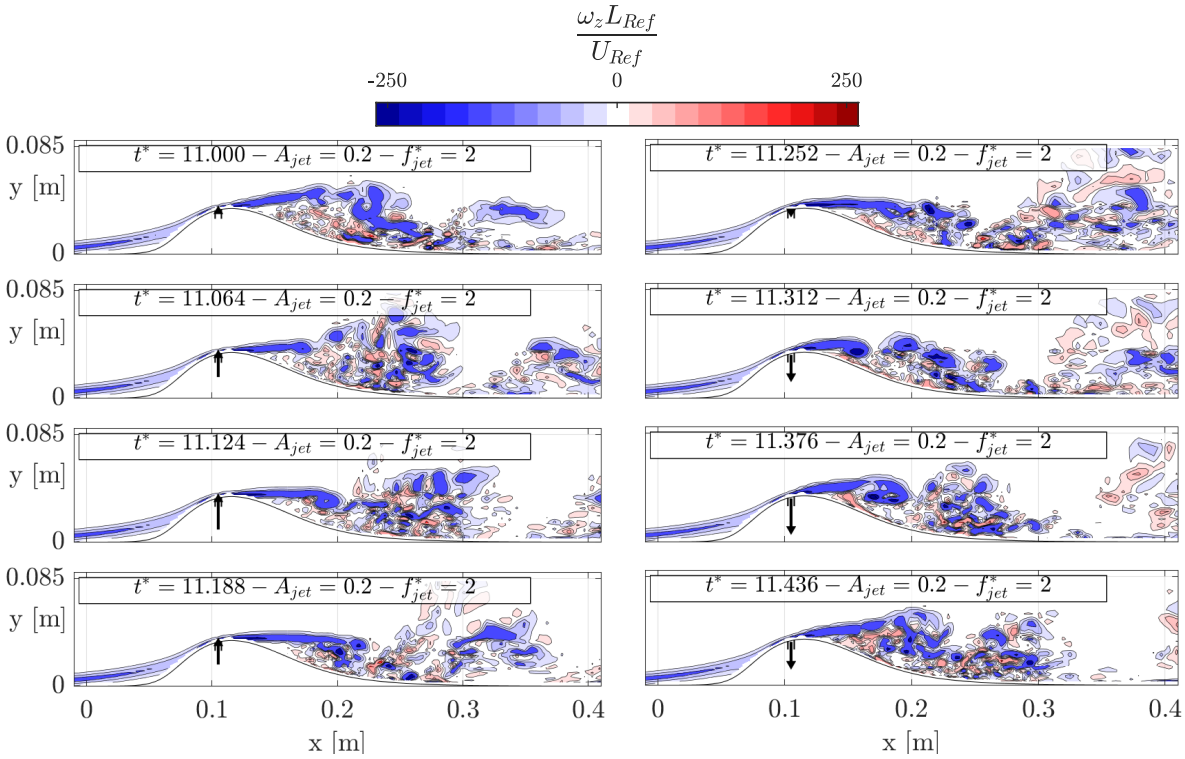

Figure 7.7: Instantaneous spanwise vorticity. $A_{jet} = 0.2,\ f^*_{jet} = 2$

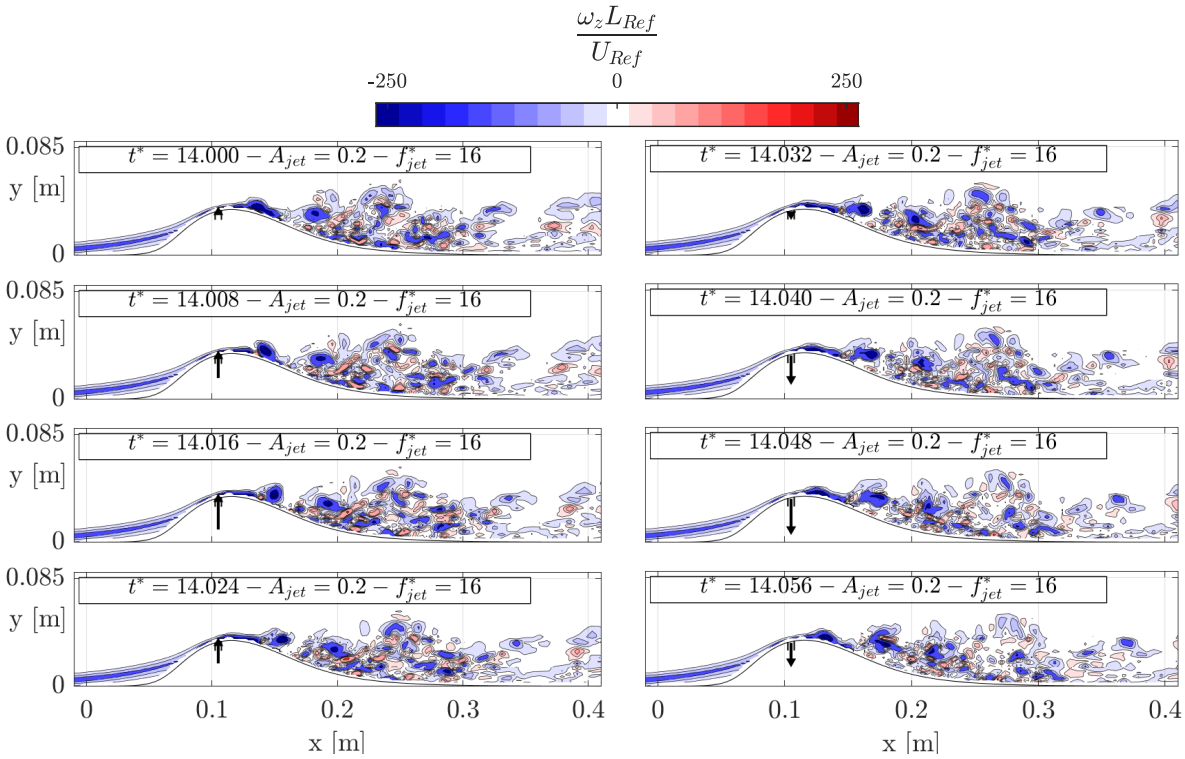

Figure 7.8: Instantaneous spanwise vorticity. $A_{jet} = 0.2,\ f^*_{jet} = 16$

also enhancing entrainment within the recirculation region. In the case of turbulent inflow, as shown in the Appendix E, the spanwise vortex is less distinct, rapidly dissipating and mixing with the surrounding turbulence.

Mean flow fields

The mean flowfield characteristics are presented through time-averaged streamwise velocity and turbulence kinetic energy (TKE) in Fig. 7.9. The cases are divided into three regimes, as outlined by Sigurdson (1995). The first regime, shown in Fig. 7.9a, corresponds to the case when the actuation frequency is of the same order as the shedding frequency. The second regime, Fig. 7.9b, represents the optimum range of actuation frequencies, where $f^*_{shed} < f^*_{jet} < f^*_{KH}$. The final regime, Fig. 7.9c, occurs when $f^*_{jet} > f^*_{KH}$.

Dandois et al., 2007 suggests that at low-frequency actuation, where $f^*_{jet} = \mathcal{O}(f^*_{shed})$, the production of TKE will increase thereby enhancing the entrainment process. This relationship is evident in Fig. 7.9a. As A_{jet} increases, TKE also increases. Moreover, the formation of large vortex clusters generates a substantial recirculation region and a maximum reverse velocity of $\overline{u}_{rev,max} \sim 20\%$ of the freestream velocity. In the optimal actuation frequency range (Fig. 7.9a), TKE decreases as A_{jet} increases. The high-TKE region shifts upstream toward the separation point, but remains located on the mean separated shear layer. However, its location does not align with the position of maximum reverse flow. The mean recirculation region is significantly reduced, with the maximum reverse velocity decreased to $\overline{u}_{rev,max} \sim 10\%$ of the freestream. The last regime ($f^*_{jet} > f^*_{KH}$), shown in Fig. 7.9c, exhibits contour patterns similar to that of the optimal frequency range. A reduction in TKE is visible compared to the previous regime. The location of the highest TKE remains relatively stationary or slightly shifts upstream in the low A_{jet} case. The time-averaged streamwise velocity shows a larger mean recirculation region with a higher maximum reverse flow, now located further downstream. In summary, the figure suggests that the overall size and magnitude of TKE in the recirculation region, along with the proximity of the high-TKE area to the separation point and wall, control the mean recirculation region.

7.2.2 Strategy II: Alternating blowing and suction actuation with inactive intervals

Table 7.3 presents the DNS simulations performed using actuation strategy II. The dataset includes two simulations with f^*_D values of 1 and 2, both conducted at an amplitude $A_{jet} = 20\%$ and frequency $f^*_{jet} = 16$. The simulations are with laminar inflow conditions, as the previous section suggested that cases with laminar and turbulent inflow exhibit similar characteristics. Both simulations used a duty ratio $D = 1$, which translates to a half-period during which the synthetic jet is inactive and the other half during which it actively performs blowing and suction into the domain. The duty phase ϕ_{jet} of the synthetic jet is illustrated in Fig. 7.4. Due to the inactive period, the phase-averaged momentum coefficient is 8.7×10^{-5}, which is four times lower than the value without an idle period. This corresponds to an effective $A_{jet} = 10\%$ in the previous strategy.

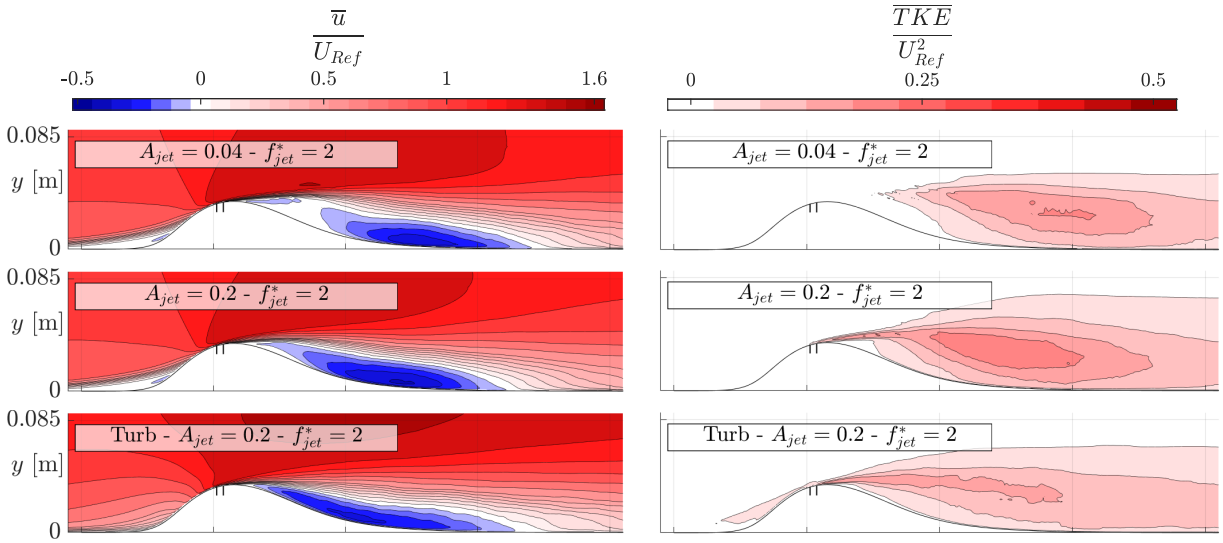

(a) $f^*_{jet} = \mathcal{O}(f^*_{shed})$

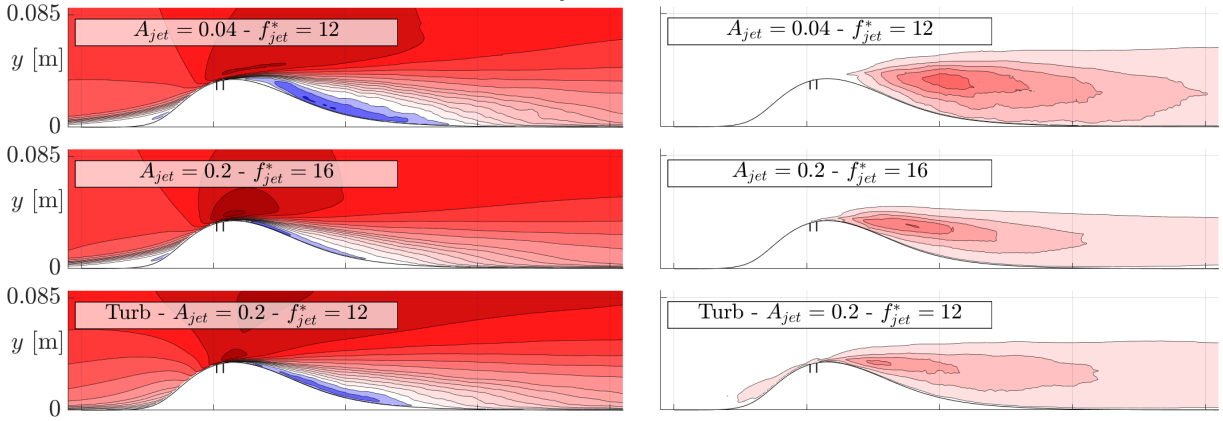

(b) Optimum frequency actuation $f^*_{shed} < f^*_{jet} < f^*_{KH}$

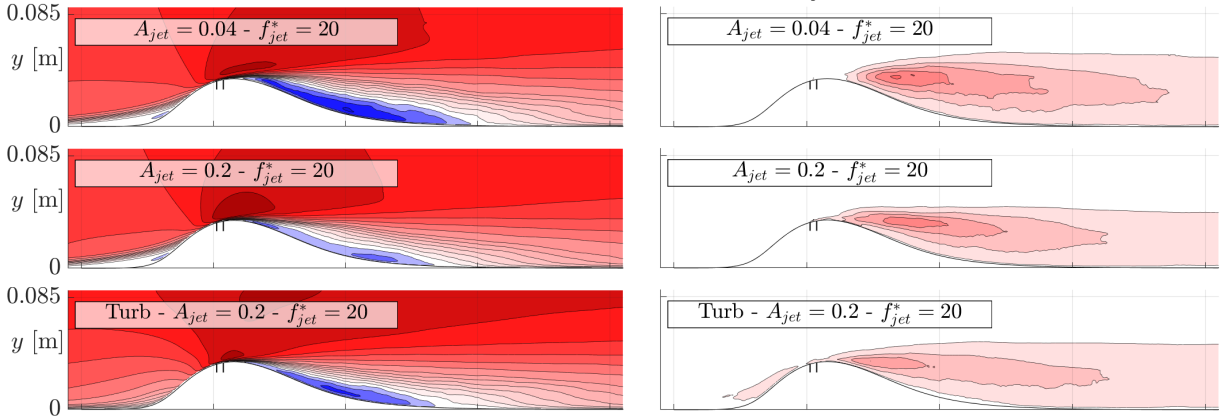

(c) $f^*_{jet} > f^*_{KH}$

Figure 7.9: Time-averaged streamwise velocity (left) and turbulence kinetic energy (right) for actuation strategy I

Table 7.3: Summary of the cases simulated for strategy II

Inflow	A_{jet}	f^*_{jet}	f^*_{jet}/f^*_{shed}	C_μ 10^{-4}	D	f^*_D (m)	x_s (m)	x_r (m)	L_s (m)	ΔL_s	Y_{p_t}
laminar	0.2	16	5.5	0.87	1	1	0.116	0.295	0.179	-0.099	0.27
laminar	0.2	16	5.5	0.87	1	2	0.116	0.288	0.172	-0.106	0.27

Both simulations result in an identical mean separation point, which is located farther downstream compared to the unactuated case. The mean reattachment location for $f^*_D = 1$ is farther downstream than for $f^*_D = 2$. As a result, the case with $f^*_D = 1$ exhibits a marginally larger mean recirculation length compared to $f^*_D = 2$, with L_s values 0.179 and 0.172, respectively. The stagnation pressure loss coefficient Y_{pt} is identical for both cases.

The reduction in the mean recirculation region is $\Delta L_s \approx 0.1$ m relative to the unactuated case for these duty frequencies. Considering the relationship between the momentum coefficient and the maximum reduction in the mean separation length for the previous strategy (Eq. (7.9)), the expected maximum reduction for the equivalent C_μ using strategy I is 0.117 m. This value is close to the reduction observed in the cases simulated with strategy II.

Additional simulations would be required to determine whether the actuation frequency $f^*_{jet} = 16$ and $D = 1$ represents the optimal frequency and duty ratio. However, the simulated cases provide evidence of a potential alternative approach that allows the actuation system to rest and prepare for subsequent blowing and suction cycles.

Instantaneous flow fields

Figures 7.10 and 7.11 show the instantaneous spanwise vorticity fields for cases simulated with duty frequencies of $f^*_D = 1$ and $f^*_D = 2$, respectively. The arrows in the figures indicate the state of the synthetic jet (blowing or suction), with their lengths representing the corresponding magnitude. Each figure contains eight subfigures, corresponding to duty phases $\phi_D = \{0, 45, 90, \ldots, 315\}^\circ$, arranged sequentially in increasing order of the indicated time (t^*). During the duty phases from 0° to 180°, the synthetic jet is inactive, while it becomes active during the phases from 180° to 360°, see Fig. 7.4. The number of periodic blowing and suction cycles is given by $Df^*_{jet}/((D + 1/D)f^*_D)$, which results in 8 cycles for $f^*_D = 1$ and 4 cycles for $f^*_D = 2$ in the simulated cases.

The figures reveal that the flow dynamics are governed by the periodic generation of a large vortex cluster during the inactive jet period and the periodic formation of a dominant spanwise vortex during the jet active period. The dominant spanwise vortex plays a critical role, reducing the separation region and driving the downstream movement of the vortex cluster.

In both cases, the vortex cluster begins to form immediately after the last spanwise vortex from the jet's blowing and suction phase detaches from the wall. At this stage, the streamwise acceleration K near the separation point is expected to reach its maximum negative value (i.e., maximum deceleration). The cluster originates from the amalgamation of smaller vortices

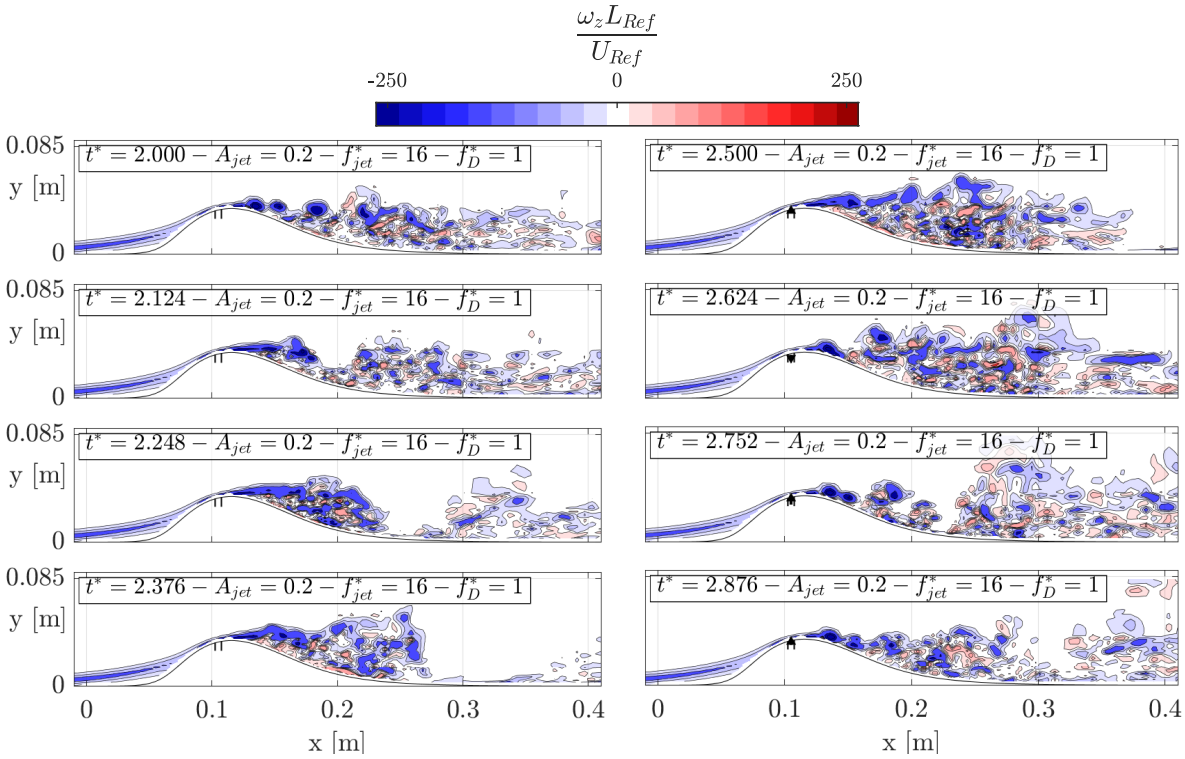

Figure 7.10: Instantaneous spanwise vorticity. $A_{jet} = 0.2,\ f^*_{jet} = 2,\ f^*_D = 1$

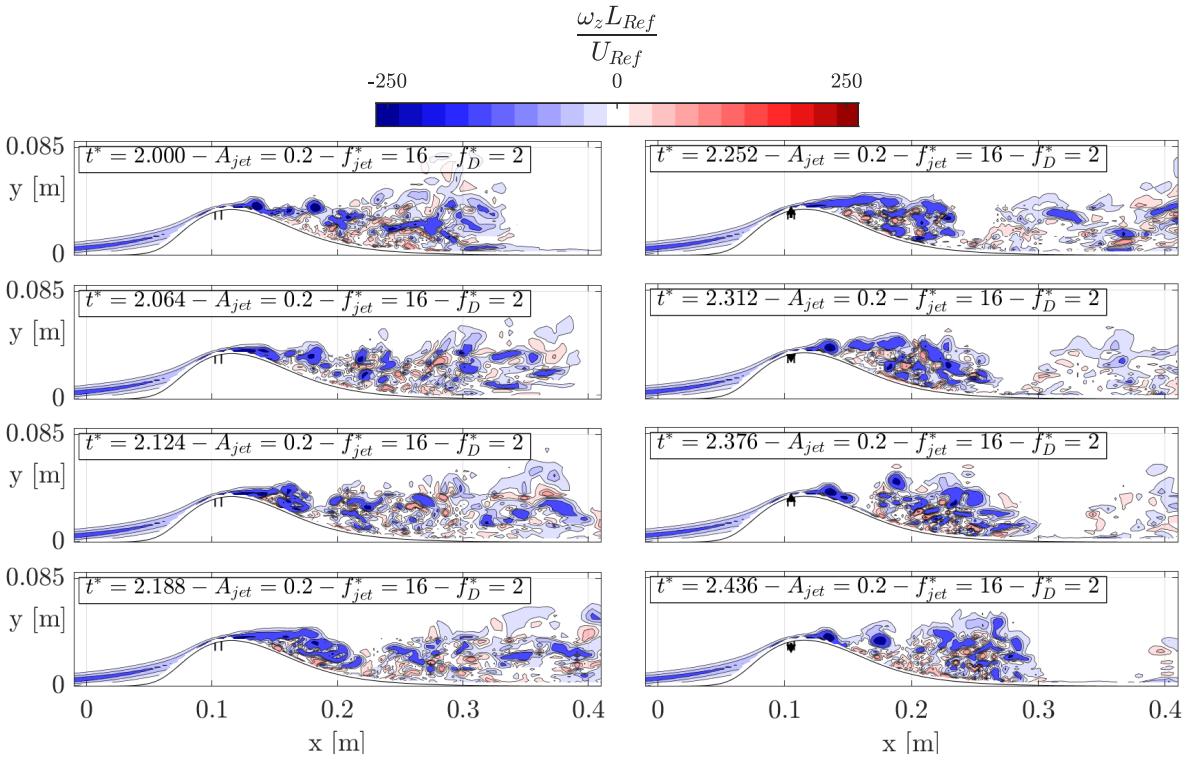

Figure 7.11: Instantaneous spanwise vorticity. $A_{jet} = 0.2,\ f^*_{jet} = 2,\ f^*_D = 2$

generated by shear layer instabilities. The duration of the jet-inactive phase significantly influences the size of the vortex cluster. Cases with higher duty frequency f_D result in a larger accumulation of small vortices. By duty phase $\phi_D = 180°$, a more mature vortex cluster corresponds to a downstream shift of the reattachment point. Once the jet becomes active, the dominant spanwise vortex periodically sheds downstream, dispersing the vortex cluster and causing it to dissipate as it moves downstream. This process effectively reduces the size of the recirculation region until the jet transitions to an inactive state. For lower duty frequencies (longer jet active periods), the recirculation region is suppressed more effectively, and the separation point moves upstream. When the jet becomes inactive again, a new vortex cluster begins to form and the process repeats.

Mean flow fields

The mean flowfield characteristics are presented using time-averaged streamwise velocity and turbulence kinetic energy (TKE) in Fig. 7.12. Both cases exhibit similar contour patterns in the TKE, with minor variations in magnitude. The lower duty frequency ($f_D^* = 1$) features a smaller mean recirculation region/size and a lower maximum mean reverse flow $\overline{u}_{rev,max}$ compared to the higher duty frequency $f_D^* = 2$. These differences are driven by the longer active time of the jet at the lower duty frequency. On the other hand, the higher duty frequency results in a slightly shorter mean recirculation length L_s, which is attributed to the smaller vortex cluster size caused by the shorter inactive jet period.

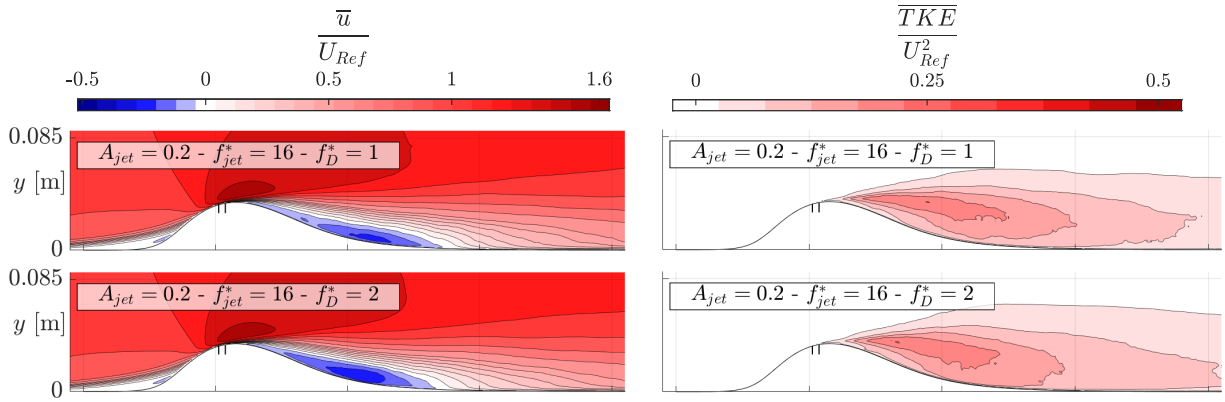

Figure 7.12: Time-averaged streamwise velocity (left) and turbulence kinetic energy (right) for actuation strategy II

7.3 Mode decomposition of oscillatory components with synthetic jets

This section analyzes the results by decomposing the oscillatory flow fields using Orthogonalized Variational Mode Decomposition (OVMD). The oscillatory flow fields are used to isolate phenomena that are coherent with the synthetic jet or duty phases. The data consist of

streamwise and wall-normal velocity snapshots spanning $x \in [-0.05, 0.445]$ and $y \in [0, 0.083]$ at the midspan of the domain, discretized into 127×42 pixels per velocity field. The snapshot sampling frequency, $f_s^* = 250$, is an order of magnitude higher than both the highest actuation frequency and the Kelvin–Helmholtz (KH) frequency.

The multivariate oscillatory component data coherent with the inflow frequency is defined as shown in Eq. (6.10). The multivariate phase-averaged data, $< \mathbf{q} >$, represents the spatial topology of both streamwise and wall-normal velocities. Phase averaging is performed using the lowest inflow actuation frequency ($f_{jet}^* = 2$) for strategy I (coherent with the actuation phases) and the duty frequency (coherent with the duty phase) for strategy II. Additionally, the oscillatory component data, $\tilde{\mathbf{q}}(\phi)$, contains 10,668 channels per snapshot (5,334 pixels for each velocity component). The data are padded as described in Chapter 6.

Multivariate POVMD is performed for both results with actuation strategies I and II. For strategy I, two cases are selected with $A_{jet} = 20\%$, laminar inflow, and $f_{jet}^* = \{2, 16\}$. For the actuation strategy II, a case is selected with $f_D^* = 2$. Each resulting mode $\tilde{M}$ comprises a temporal coefficient c and a spatial topology ψ, as presented in Chapter 5 and 6. The spatial structure is represented using the spanwise vorticity ψ_{ω_z}, defined in Eq. (5.24).

7.3.1 Laminar inflow, Strategy I - $A_{jet} = 0.2,\ f_{jet}^* = 2$

The energy ratios of the modes and their first 14 dominant components are presented in Figs. 7.13-7.15. The energy ratio quantifies the total energy of the streamwise and wall-normal velocities of the modes relative to the input snapshots, as in Eq 6.11.

The energy of the oscillatory data, represented as $\tilde{\mathbf{q}} = [\tilde{\mathbf{u}}; \tilde{\mathbf{v}}]$ from the discretized snapshot data, constitutes approximately 3% of the total energy of the streamwise and wall-normal velocity, $\|\mathbf{q}\|_F^2$. The time-averaged component accounts for 90.5% of the total energy, while the incoherent component, $\mathbf{q}'$, contributes approximately 6.5%. Notably, this 3% of energy coherent with the jet oscillation is distributed among 14 modes, as shown in Fig. 7.13.

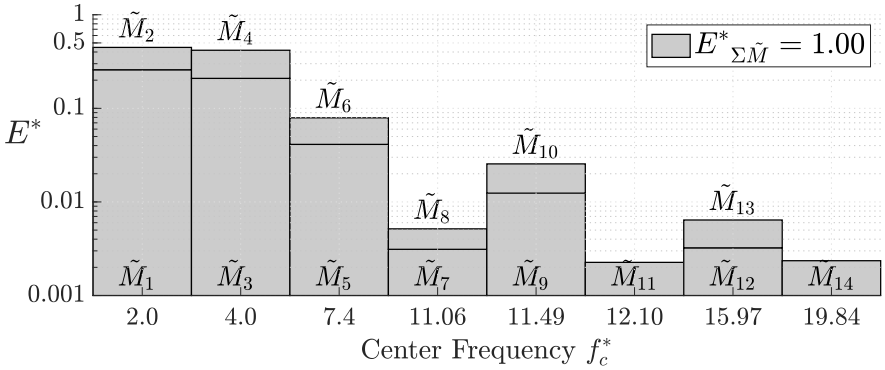

Figure 7.13: Energy ratio of modes - laminar - $A_{jet} = 0.2,\ f_{jet}^* = 2$

The dynamics of the coherent structure are predominantly driven by the mode pair corresponding to the actuation frequency and its harmonic, as shown by modes 1 to 4 in Figs. 7.13 and 7.14. These modes account for nearly 90% of the fluctuations in the phase-averaged

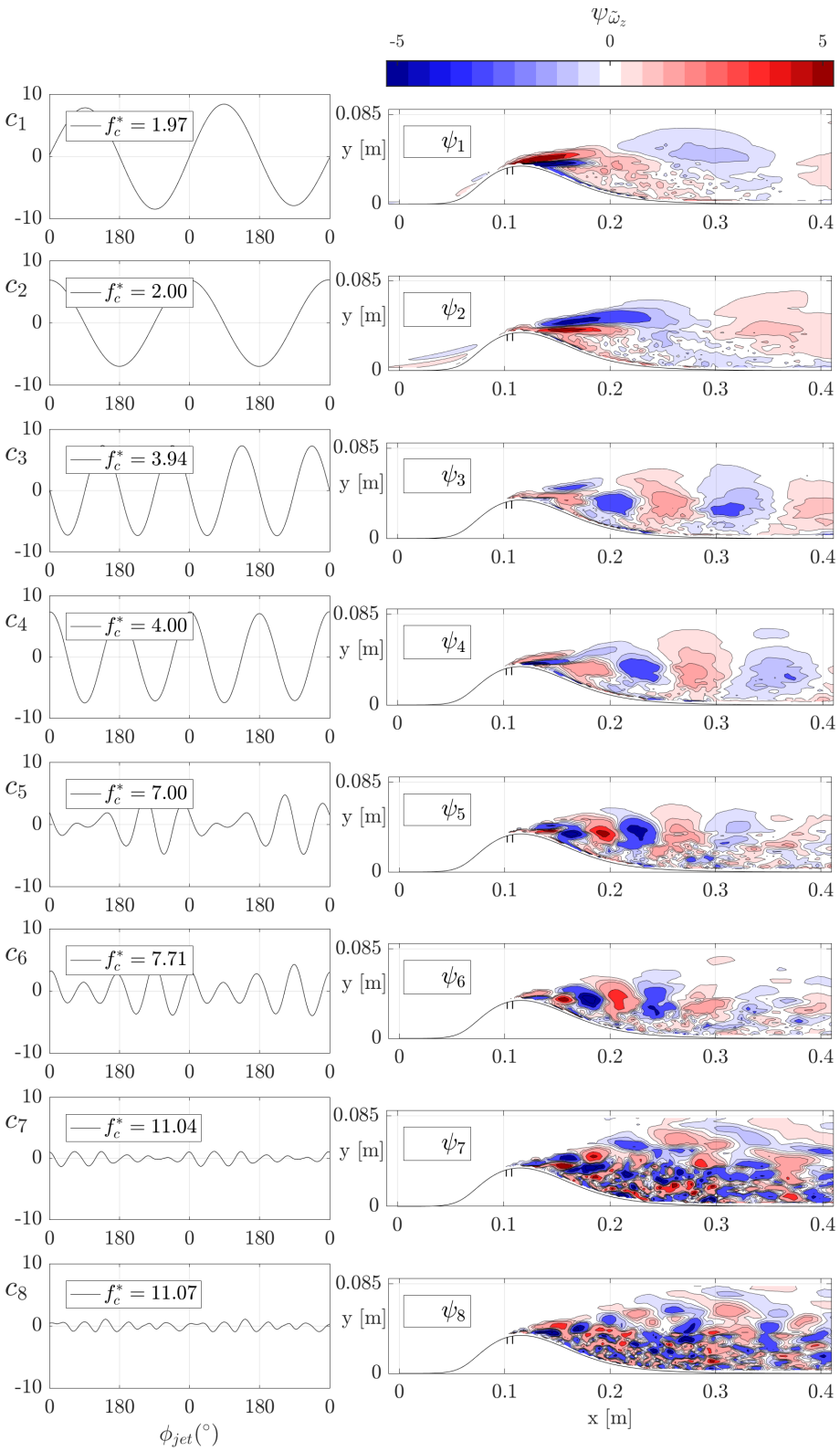

Figure 7.14: OVMD modes 1-8, represented by spanwise vorticity, for the Bump with laminar inflow and $A_{jet} = 0.2,\ f_{jet}^* = 2$

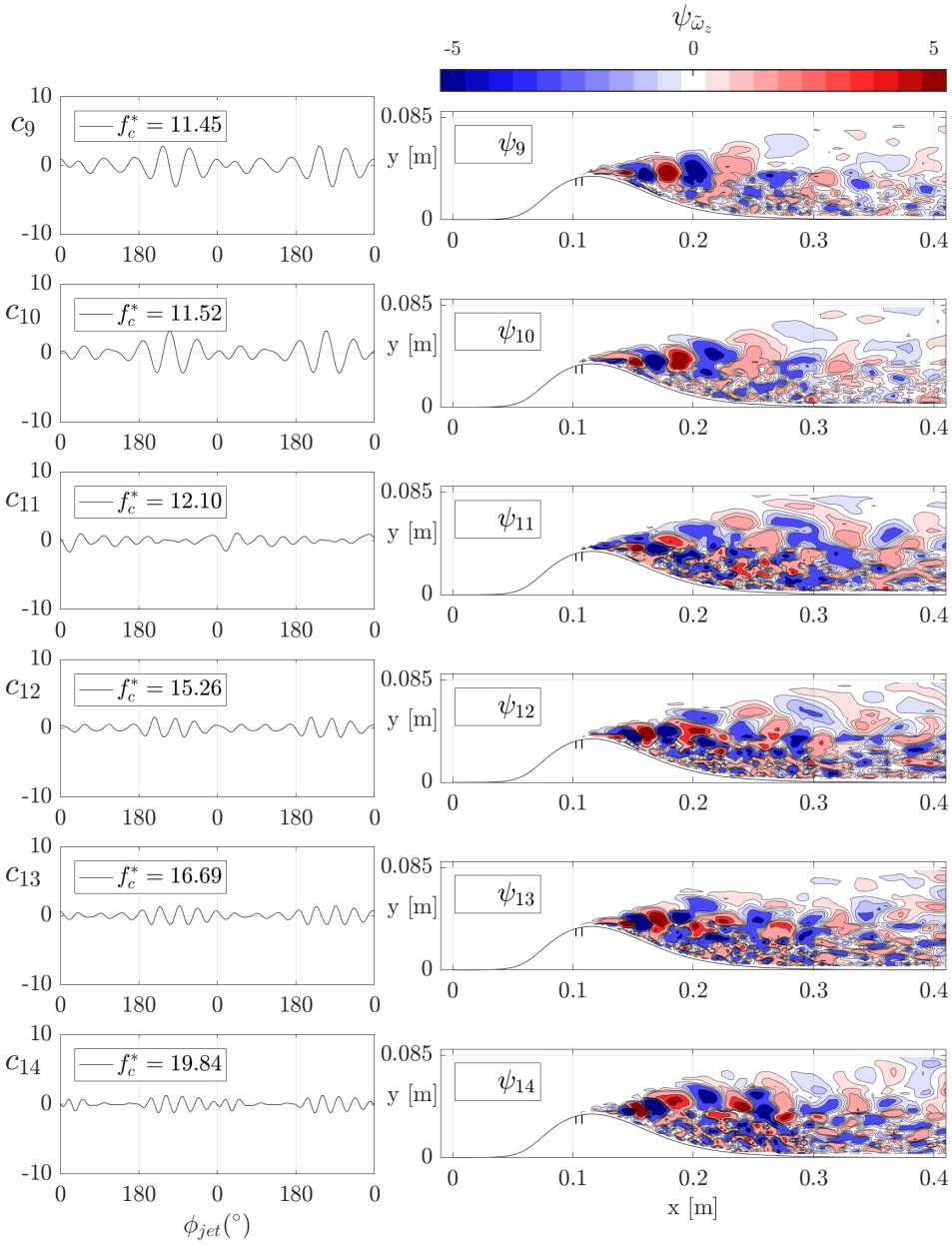

Figure 7.15: OVMD modes 9-14, represented by spanwise vorticity, for the Bump with laminar inflow and $A_{jet} = 0.2$, $f^*_{jet} = 2$

data and represent the vertical movement of the separated shear layer, which leads to the formation of large vortices. The first harmonic pair exhibits its maximum amplitude within the separated shear layer, while the second harmonic pair shows its maximum amplitude distributed between the separated shear layer and the vortices.

The significant contribution of the second harmonic pair to large vortex formation is evident from the premature release of medium-sized vortices downstream, as shown in Fig. 7.7 for $\phi_{jet} = 270^\circ - 360^\circ$. Meanwhile, other medium-sized vortex clusters associated with the second harmonic grow and align with the large vortex in the first harmonic. Consequently, the

dynamics observed in the first and second harmonic pairs align more closely with Scenario 2 from Chapter 6, where the formation and release of vortex clusters do not occur consistently across all phases due to the premature release of medium-sized vortices from the second harmonic. This observation is further supported by the absence of third and fourth harmonic modes with localized event characteristics, as seen in the mode decomposition of Scenario 3 in Chapter 6.6.3.

The other lower-energy modes represent the instability of the separated shear layer and its subharmonic. The Kelvin-Helmholtz (KH) vortices are prominent during the jet phase $\phi_{jet} = 180° - 360°$. These vortices are captured by mode pairs 12 and 13, while their subharmonic counterparts are represented by modes 5 and 6, as well as the intermediate mode pair 8 and 9. The subharmonic modes 5 and 6 are formed through the amalgamation of smaller vortices. The significant energy of these modes suggests that the premature release of medium-sized vortices during these jet phases is driven by the strong vortices in these modes. Additionally, modes 7, 8, 11, and 14 also capture aspects of the shear layer instability.

7.3.2 Laminar inflow, Strategy I - $A_{jet} = 0.2,\ f^*_{jet} = 16$

For the optimum frequency actuation $f^*_{jet} = 16$, the energy ratios of the modes and the six dominant modes are illustrated in Figs. 7.16–7.17. The oscillatory data coherent with the actuation frequency accounts for only 1% of the total energy, while the mean and incoherent components contribute 95.5% and 3.5%, respectively. Most of the dynamics are incoherent with the jet oscillation, with the coherent oscillation localized near the wall along the mean separated shear layer. These coherent oscillations are captured by six modes, which collectively represent 91% of the coherent oscillation energy, as shown in Fig. 7.16.

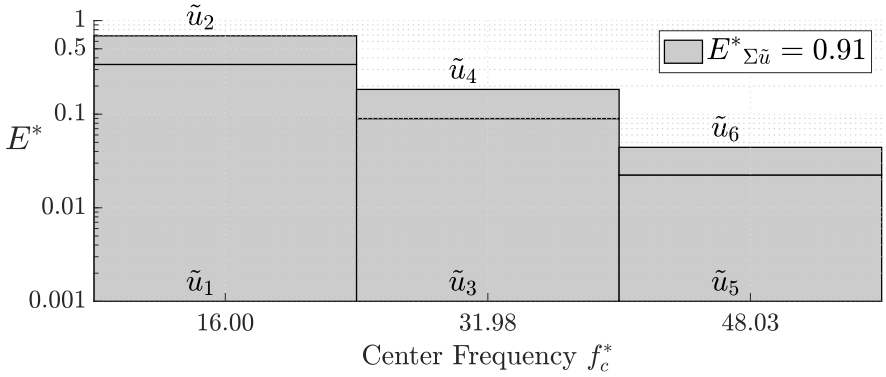

Figure 7.16: Energy ratio of modes - laminar - $A_{jet} = 0.2,\ f^*_{jet} = 16$

The dynamics of the coherent structures are strongly driven by the jet frequency, as evidenced by modes 1 and 2 in Fig. 7.17. These modes account for approximately 70% of the fluctuations in the phase-averaged data and represent the periodic formation and release of spanwise-dominant vortices. The second and third harmonic modes are present but with significantly lower energy, showing a reduction to about one-quarter of the energy of the preceding harmonic. The periodic formation of spanwise vortices pushes the separated shear layer closer to the wall, effectively reducing the size of the recirculation region. Furthermore, no

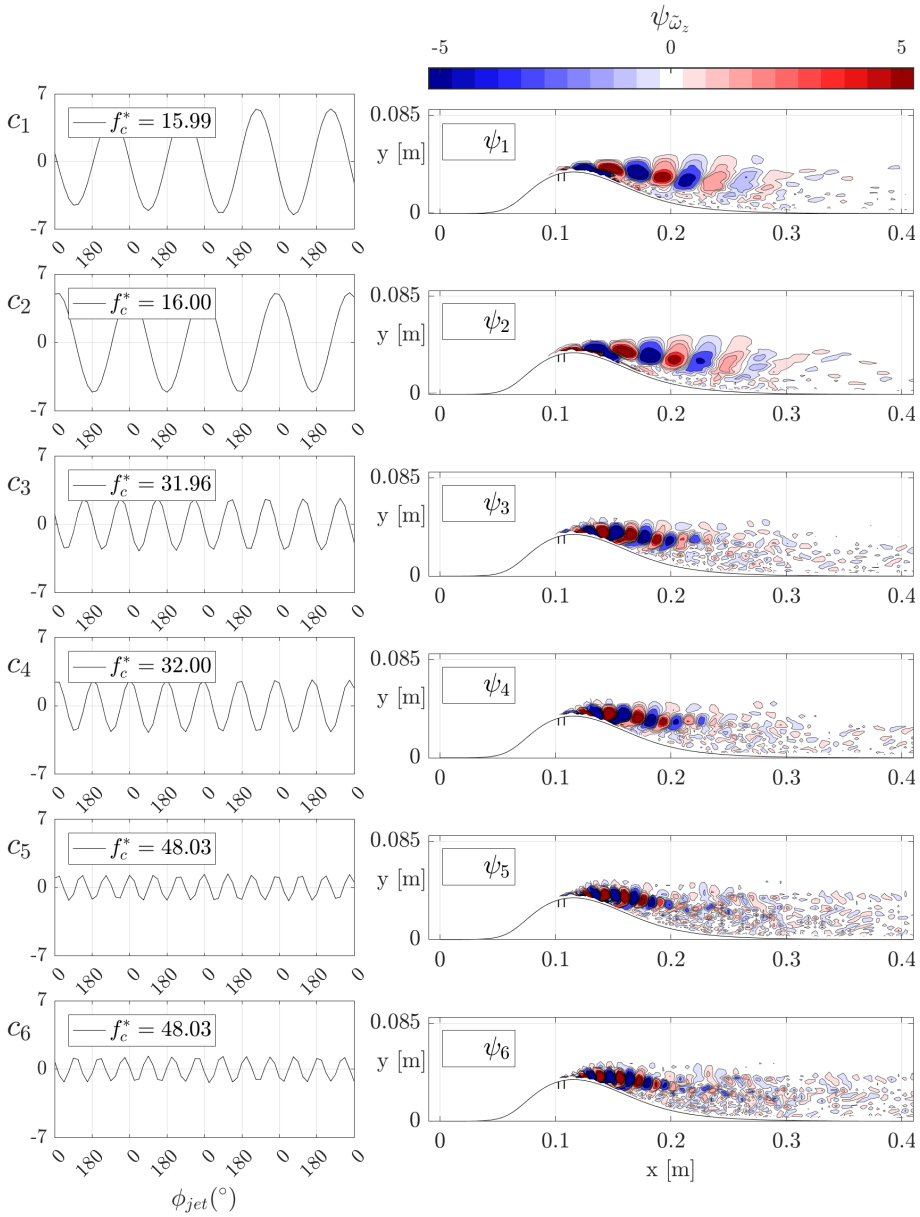

Figure 7.17: OVMD modes 1-6, represented by spanwise vorticity, for the Bump with laminar inflow and $A_{jet} = 0.2,\ f^*_{jet} = 16$

dominant subharmonic is observed in the decomposition, suggesting that most of the energy is transferred through a cascade process, which translates into enhanced entrainment.

7.3.3 Laminar inflow, Strategy II - $A_{jet} = 0.2,\ f^*_{jet} = 16,\ f^*_D = 2$

The decomposition of the selected case with actuation strategy II is presented in Fig. 7.18 for the energy ratios, and in Figs. 7.19 and 7.20 for the temporal and spatial topology of the spanwise vorticity. The oscillatory data coherent with the duty frequency accounts for approximately 4.7% of the total energy, while the mean flow and incoherent components contribute 91% and 4.3%, respectively. The energy associated with these coherent fluctuations is distributed across 12 dominant modes, as shown in Fig. 7.18.

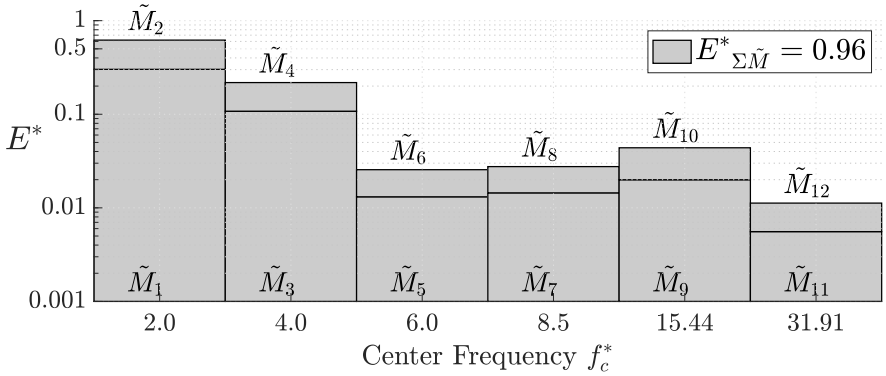

Figure 7.18: Energy ratio of modes - laminar - $A_{jet} = 0.2,\ f^*_{jet} = 16,\ f^*_D = 2$

The dynamics is predominantly influenced by the inflow frequency, as indicated by the mode pair 1 and 2. These modes account for approximately 62% of the fluctuations in the phase-averaged data and correspond to the vertical motion of the separated shear layer and the periodic formation of a large vortex. The maximum amplitude occurs in the separated shear layer, with values that do not differ significantly from the maximum amplitude in the large vortex, as shown in Fig. 7.19. The time coefficients of these modes do not exhibit temporal localization due to the state change of actuation, indicating that the formation and release of large vortex clusters span all duty phases.

The second harmonic (modes 3 and 4), third harmonic (modes 5 and 6), and fourth harmonic (modes 7 and 8) capture the intricate dynamics of large vortex generation. These modes are significantly weaker than the first harmonic pair. The fourth harmonic modes exhibit phase locality, becoming suppressed during the early stage of the jet active period ($\phi_D = 180° - 270°$). This behavior is similar to Scenario 3 in Chapter 6, although it occurs in the fourth harmonic modes rather than the third. The phase locality of the fourth harmonic pair results in slower advection of the large vortex cluster during their suppression, allowing the reattachment point to remain farther upstream for a longer duration.

During the synthetic jet active period, $\phi_D = 180° - 360°$, spanwise-dominant vortices are generated due to the periodic blowing and suction of the jet. The first and second harmonic modes are represented by the mode pairs 9–10 and 11–12, respectively. Outside this period, the time coefficients approach zero.

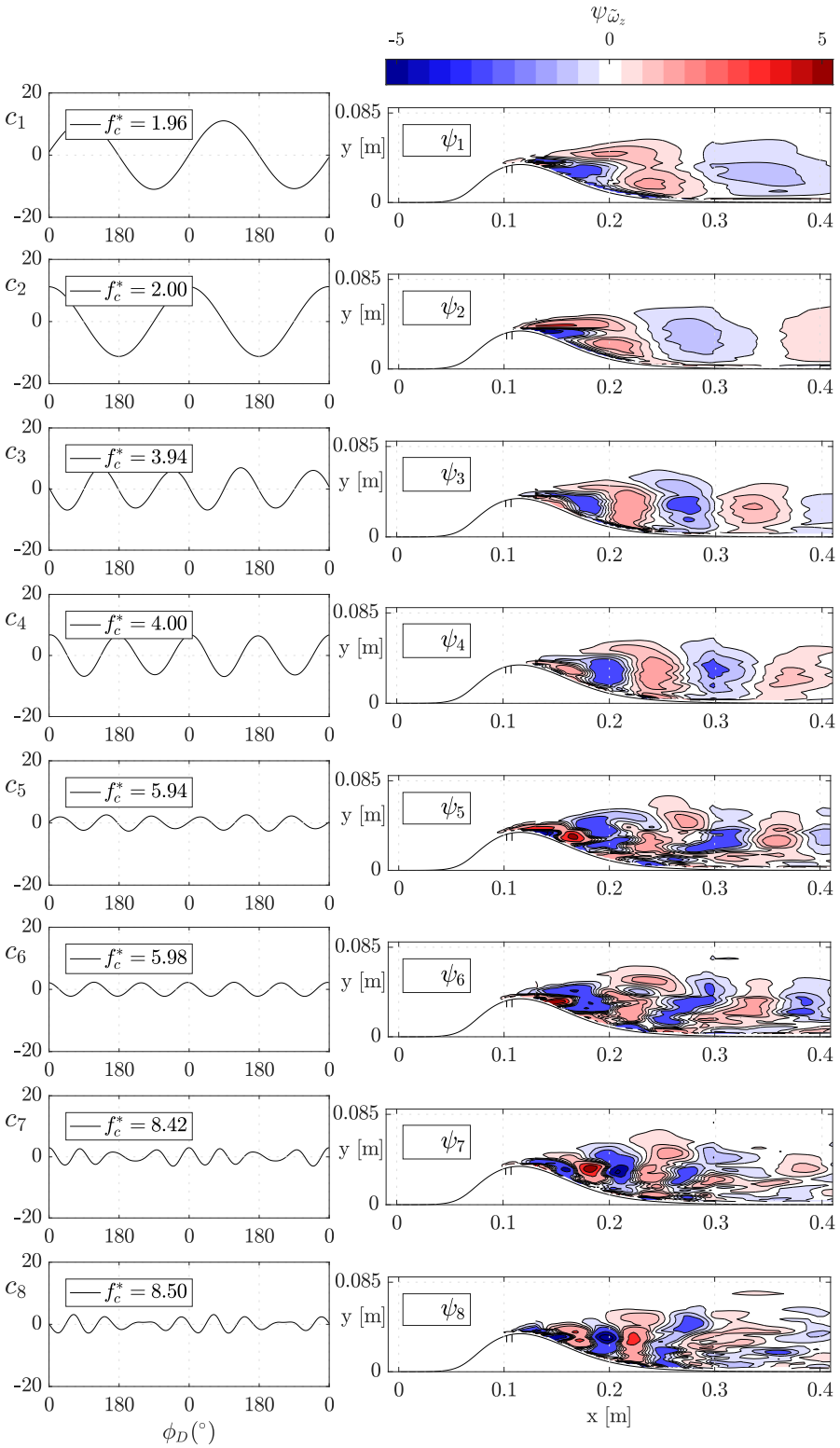

Figure 7.19: OVMD modes 1-8, represented by spanwise vorticity, for the Bump with laminar inflow and $A_{jet} = 0.2$, $f^*_{jet} = 16$, $f^*_D = 2$

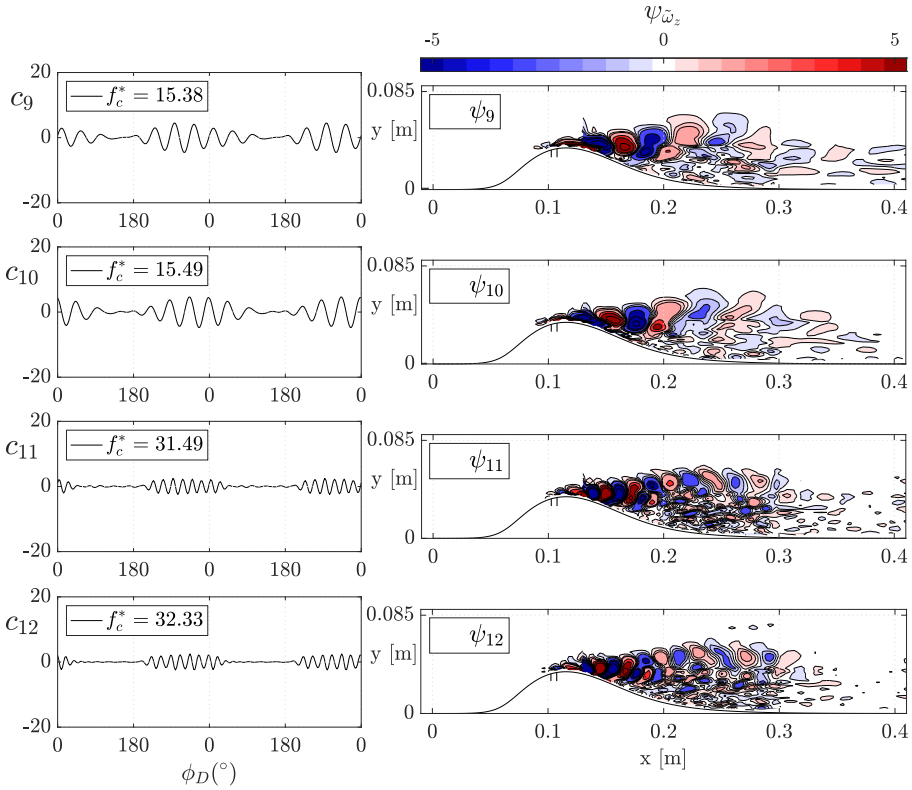

Figure 7.20: OVMD modes 9-16, represented by spanwise vorticity, for the Bump with laminar inflow and $A_{jet} = 0.2,\ f^*_{jet} = 2,\ f^*_D = 2$

Chapter 8

General Discussions

This chapter discusses and analyzes the novel time-frequency modal decomposition introduced and the results obtained in the study of the impact of harmonic inflow oscillations and a 2D synthetic jet on the separated flow over a bump geometry.

8.1 A time-frequency modal decomposition for the analysis of non-stationary flow

Chapters 4 and 5 introduce a novel data-driven time-frequency modal decomposition, named Orthogonalized Variational Mode Decomposition (OVMD). The methodology is primarily developed for analyzing non-stationary separated flow, particularly in high Reynolds number and complex geometry settings, but it can also be applied directly to other applications. The technique demonstrates its superiority in decomposing data with time locality.

In OVMD, two key modifications are introduced: (i) the incorporation of orthogonality objectives and (ii) an adaptive filter bandwidth strategy, α_k. Together, these enhancements result in a significantly more robust decomposition over the original VMD (Dragomiretskiy and Zosso, 2014) and effectively mitigating over-segmentation. When an excessive number of modes is prescribed, the additional modes exhibit very small amplitudes or capture high-frequency incoherent fluctuations. Consequently, this prevents mode duplication, minimizes interference between the resulting modes, as demonstrated in the sensitivity analysis in Section 4.4.3, and improved robustness due to noise contamination. Additional advantages of the method include its robustness to the prescribed constant factor F and its improved convergence. To further refine the methodology in under-segmentation, a progressive algorithm is implemented. In progressive OVMD, the decomposition first captures the set of modes with higher amplitudes/energy, while the remaining components are preserved in the residual.

The extension of the technique to multidimensional/multivariate data further enhances its value. The multivariate approach decomposes the time-dependent flow field as a linear combination of modes, where each mode consists of a time-invariant spatial function and

a scalar temporal coefficient. This formulation is shared with other modal decomposition techniques such as Proper Orthogonal Decomposition (POD) (Berkooz et al., 1993; Lumley, 1970), Spectral POD (Towne et al., 2018), and Dynamic Mode Decomposition (DMD) (Schmid, 2010). Previous implementations of this multivariate (reduced-order) VMD approach in fluid flow have demonstrated its effectiveness in extracting low-dimensional models of non-stationary flows (Liao et al., 2023).

In the multivariate progressive OVMD, the improvement of the method is evident, as it is capable of accurately decomposing different types of data at a considerably low cost. The transient cylinder wake demonstrates the methodology's ability to recover a "spectral-like" modal decomposition, where discrete structures, such as individual vortices, emerge through the linear combination of multiple modes. The spatial functions of these modes resemble wavepackets, similar to those identified by POD or SPOD. However, unlike traditional methods, OVMD does not require an additional projection of the original data onto the spatial functions to obtain the time coefficients. Instead, the time coefficients— which directly capture non-stationary dynamics—are computed simultaneously with the spatial functions. This coupled determination of spatial and temporal components enables a more efficient flow decomposition.

8.2 Impact of harmonic inflow oscillations on the separated flow

Chapter 6 studies the impact of harmonic oscillations of the inflow velocity, imposed via the total pressure, on the flow over a wall-mounted bump geometry. This geometry gives rise to a streamwise pressure gradient distribution with similar features to those encountered in LPT blades. The harmonic inflow oscillation roughly models the effect of the passage of the wake due to the previous stage of blades, periodically creating a velocity deficit followed by acceleration, and consequently a periodic modification of streamwise velocity gradients.

Under steady inflow conditions, the laminar-to-turbulent transition is initiated by a self-excited KH instability with a well-defined vortex-shedding frequency ($f^*_{KH} \approx 18$). These vortices are subject to secondary instabilities and interactions with turbulent structures that are recirculated within the separated flow and progressively break down into smaller eddies as they travel downstream. The associated entrainment leads to the reattachment of the mean flow.

The impact of the inflow oscillations on the flow dynamics is strongly dependent on the frequency and amplitude of the oscillations. The cases studied involve oscillations of the inflow total pressure A_{in} between 1% and 10% of the mean value, and frequencies $f^*_{in} = 0.5 - 2$, substantially lower than f^*_{KH} but comparable to the wake-passing frequency in LPT turbines. If the reference velocity U_{Ref} and the mean recirculation length for the steady inflow case $L_s = 0.2782$ m are used to calculate the reduced frequency F, the inlet frequencies f^*_{in} take the values $F = 0.1391, 0.2782$ and 0.5564, which lie between the $F \ll 1$ and $F \sim 1$ ranges. Three different scenarios have been identified. Table 6.3 shows the classification of the cases

and Fig. 6.28 depicts them schematically:

Scenario (i): *Inflow-modulated Kelvin-Helmholtz vortex shedding*, corresponding to comparatively weak inflow oscillations (lowest values of A_{in} and f^*_{in}, cf. Fig. 6.2 and 6.28 left). The transition process is qualitatively the same as for the steady inflow case. However, the harmonic changes of the bulk velocity lead to a periodic vertical displacement of the separated shear layer, phase-locked to the inflow oscillation. While the self-sustained vortex shedding originated by KH instability remains, its spatial amplification is modulated by the changes in the shear layer properties: vortex-shedding takes place upstream for the part of the period in which the bulk flow is decelerated and downstream for the part in which it is accelerated. Consequently, the phase-averaged length of the recirculation region L_s changes gradually over the period, but the mean length (i.e. averaged over the period) is approximately the same as for the steady case. This scenario is consistent with the experiments by Lou and Hourmouziadis (2000) that imposed inflow oscillations with $\Delta u^* = 0.13$ and $F \approx 0.06$ (obtained by scaling their reported dimensionless frequency with the mean length of their separation bubble). The OVMD results successfully identify the mode corresponding to the periodic displacement of the separated shear layer, as well as a portion of the KH instability. This identification is based on phase-averaged data, as the majority of the KH component is incoherent with the inflow.

Scenario (ii): *Alternation between KH vortex shedding and formation/release of a large vortex cluster*, corresponding to intermediate inflow oscillations (see Fig. 6.16 and 6.28 centre, and supplementary movies 3 and 4). For a portion of the period, KH-initiated vortex shedding is dominant, identical to scenario (i). However, as the bulk flow decelerates, the phase-averaged streamwise acceleration parameter $\langle K \rangle$ transiently surpasses a threshold negative value in the region neighbouring flow reattachment, giving rise to new dynamics: the vortical structures formed in the shear layer are not shed and advected downstream. Instead, they are entrapped in the recirculation region, which accordingly grows in size forming a large vortex cluster formed by eddies of a wide range of scales. When the bulk flow is re-accelerated, instead of reducing the recirculation region gradually through the shedding of KH vortices (as in scenario (i)), the large vortex cluster is released and advected downstream. The advection of the vortex cluster pulls the stagnant fluid, transiently reducing the separated flow extent. Subsequently, the recirculation region regenerates and the KH vortex shedding re-starts. The periodic formation and release of the large vortex cluster impact the phase-averaged length of the reversed flow region drastically: the time-averaged L_s is reduced with respect to the steady inflow case, but the deviations from the mean value (see the PDFs in Fig. 6.13) become considerably broader including lengths longer than those for the steady inflow. Important hysteresis effects appear between the accelerating and decelerating parts of the period. This scenario would translate into undesirable conditions regarding practical LPT blades, involving strong oscillatory loads without a substantial reduction of the mean separation length. Using the OVMD decomposition, the periodic movement of the separated shear layer, the periodic formation and release of vortex clusters, and the phase-localized KH vortices are clearly visible in the decomposition of the phase-averaged data.

Scenario (iii): *Phase-locked formation and release of large vortex clusters*, corresponding to strong inflow oscillations (the largest values of A_{in} and f^*_{in}, cf. Fig. 6.3 and 6.28 right).

The dynamics of the formation and release of the large vortex cluster following the inflow oscillations occupy all periods: before one vortex cluster has time to travel downstream a distance sufficient for the recirculation region to re-initiate the KH vortex shedding, the threshold value of the streamwise acceleration parameter is reached and a new vortex cluster is being formed. The deviation of the separated flow length over the period is larger than that of scenario (i) but less than that of scenario (ii). More importantly, the phase-averaged L_s is smaller than the mean length for the steady inflow case for all the phases and the time-averaged L_s is remarkably reduced, above a 40% for the case ($A_{in} = 0.1$, $f^*_{in} = 2$). Regarding a practical LPT application, this scenario would be preferable over the other two. This scenario is the same recovered in the simulations by Wissink and Rodi (2003) and Wissink (2006), who considered different inflow frequencies between $F \approx 1$ and $F \approx 6$ and amplitudes Δu^* between 0.05 and 0.2. The OVMD decomposition reveals the periodic movement of the separated shear layer, the periodic formation and release of vortex clusters, the phase-localized weak vortices, and modes corresponding to the amalgamation of small vortices in the phase-averaged data.

In order to clarify if our conclusions regarding the three different scenarios are general or particular to wall-mounted bump geometry considered so far, Appendix D briefly presents an analogous study considering the related setup of the NASA hump. The same three scenarios are recovered, while the combination of values of A_{in} and f^*_{in} for each of them is changed.

It is to be noted that the impact of the inflow oscillations is not related to the individual parameters A_{in} or f^*_{in} but to a combination of both. In all the cases A_{in} is too large to be considered a linear flow disturbance, and f^*_{in} is an order of magnitude lower than the natural frequency of the Kelvin-Helmholtz instability, f^*_{KH}. The transition between the different scenarios is thus not associated with the excitation of the KH instability. The transition between scenarios (i) and (ii) is related to the existence of a threshold value of the acceleration parameter $\langle K \rangle$. When this value is exceeded transiently in the region towards the end of the bump, a large vortex cluster is formed and eventually released. According to the cases simulated, the threshold value is bounded between $\langle K \rangle = -16.71 \times 10^{-6}$ and -22.43×10^{-6} (see Table 6.3). However, the numerical value of this parameter is particular to the definition of $\langle K \rangle$ used, which is based on an arbitrary y coordinate. On the other hand, the transition between scenarios (ii) and (iii) is related to the ratio between the inlet oscillation period and the time required for the recirculation region to regenerate and re-start the KH vortex shedding after the release of one vortex cluster.

Our results cannot ascertain if a further increase in the inflow frequency would lead to further reductions in the time-averaged separated flow length. Within scenario (iii), the optimal time-averaged L_s reduction would be achieved by a balance between increasing the amount of recirculating fluid advected with one vortex cluster (i.e. the size of the phase-averaged vortex) and increasing the frequency of release of such clusters. However, the impact of inflow oscillations on the dynamics and time-averaged length of separated flows described in this work presents similarities with studies of active flow control via harmonic suction/blowing or moving parts reviewed by Greenblatt and Wygnanski (2000) and with the experiments by Hasan (1992) and Sigurdson (1995). These works report the existence of an optimal forcing frequency that scales with the global size of the recirculating flow region and the free-stream

inflow velocity. Forcing at this frequency range promotes the phase-locked formation and shedding of large vortices similar to present scenario (iii), altering the dynamics from those of the KH-initiated transition (scenario (i)). Greenblatt and Wygnanski (2000) concluded that the optimal forcing frequency scales with the streamwise length of the unforced recirculating flow region, L_s. Conversely, Hasan (1992) and Sigurdson (1995) argue that the natural frequency for the "shedding of the entire bubble" (i.e. release of the large coherent vortex cluster) scales with its wall-normal height h, in analogy to the von Karman vortex street, and the optimum forcing would act at this frequency. Sigurdson (1995) proposed a dimensionless frequency $St_{shedding} = fh/U_s = 0.07 - 0.08$ (where U_s is the free-stream velocity at the separation point) and demonstrated that it correlates well with a variety of geometry-induced separation bubbles. Translated into the dimensionless form used in this study, and using the bump height to estimate the half-width of the wake, the global shedding frequency is $f^*_{shedding} = 2.9 - 3.3$, which is only slightly higher than the largest f^*_{in} considered.

On the other hand, forcing with higher frequencies, aimed at exciting the -local- KH instability, may lead to a faster transition via scenario (i) Embacher and Fasel (2014) or by inducing pairing of KH-vortices Kurelek et al. (2019) and Marxen et al. (2013). This certainly leads to reductions in the time-averaged separation length, but in view of present results, these reductions are expected to be smaller than the ones achieved by exciting the global dynamics of the separated flow.

8.3 Impact of a 2D synthetic jet on the separated flow

Chapter 7 examines the impact of active control, implemented through periodic blowing and suction boundary conditions, on the flow over a wall-mounted bump geometry with both laminar and turbulent inflow. The blowing and suction boundary conditions are positioned just upstream of the mean separation point, extend in the spanwise direction to introduce a two-dimensional disturbance, and have a streamwise velocity profile resembling the solution of oscillatory plane Poiseuille flow to mimic a zero net mass flux jet. Two strategies are considered: Strategy I involves periodic blowing and suction, while Strategy II incorporates periodic blowing and suction with an inactive period or duty cycle.

In Strategy I, actuations are applied over a frequency range spanning from a frequency of the same order of magnitude as the vortex shedding to a frequency exceeding the Kelvin-Helmholtz (KH) instability, for both laminar and turbulent inflow conditions. A total of 18 cases are simulated, comprising two inflow conditions. For the laminar inflow, two amplitudes are considered, $A_{jet} = \{0.04, 0.2\}$, while the turbulent inflow is simulated with a single amplitude, $A_{jet} = 0.2$. Each condition and amplitude includes six different actuation frequencies, ranging from $f^*_{jet} = 0.8$ to 7.7 times the shedding frequency f^*_{shed}.

The simulated cases align with the findings of Sigurdson (1995), showing a similar percentage reduction in the recirculation region, and indicate that the optimal actuation frequency lies between 3 and 6 times the shedding frequency. The absence of significant differences between laminar and turbulent inflow suggests that the dynamics are primarily governed by the shedding instability, determined by the bump height, and the Kelvin-Helmholtz

(KH) instability from the shear layer, influenced by the momentum thickness at separation (θ_s). Additionally, the results reveal a logarithmic dependence of the maximum reduction in separation length on the amplitude of actuation A_{jet}, as suggested by Kiya et al. (1997).

The mode decompositions reveal distinct dynamics between the lowest frequency case, where actuation occurs at a frequency of the same order of magnitude as the shedding frequency ($f^*_{jet} = \mathcal{O}(f^*_{shed})$), and the optimum frequency range ($f^*_{shed} < f^*_{jet} < f^*_{KH}$). In the lowest frequency case, actuation induces periodic vertical movement of the separated shear layer, generating large vortex clusters. These clusters exhibit characteristics similar to those described in Scenario 2 of Chapter 6.

Within the optimum frequency range, actuation produces periodic spanwise dominant vortices that are further amplified by the shear layer instability. At frequencies higher than the Kelvin-Helmholtz instability ($f^*_{jet} > f^*_{KH}$), the dynamics remain similar to those observed in the optimum frequency range, as indicated by comparable contour patterns in the mean flow fields, with weaker spanwise dominant vortices.

In the second strategy, actuation is applied with equal time periods for the jet's active and inactive states. Two duty frequencies f^*_D are simulated with the synthetic jet frequency f^*_{jet} at the optimal frequency. The duty frequencies, $f^*_D = 1$ and 2, are of the same order of magnitude as the shedding frequency and result in a relatively similar reduction in the mean recirculation. Mode decomposition reveals that the dynamics are primarily controlled by the periodic formation and release of large vortex clusters spanning all duty phases, as well as the generation of spanwise vortices during the jet's active state. The formation and release of vortex clusters exhibit similarities to Scenario 3 in Chapter 6.

The reductions observed in cases with strategy II are close to the expected maximum reduction in mean recirculation for strategy I, assuming similar momentum coefficients C_μ and using the relationship in Eq. 7.9. This suggests the potential of strategy II, particularly in low-pressure turbine applications, as it allows the actuation system to rest and prepare for the next blowing and suction cycle. More research is needed to determine the optimum duty cycle and frequency.

The final contribution of this thesis proposes an alternative flow control strategy that aims at inducing the dynamics of Scenario 3 in a configuration with steady-inflow (Chapter 7). This novel approach, consisting of periodic blowing-suction cycles with an inert state (actuation strategy II), demonstrates the potential to match the optimum performance of periodic blowing-suction without an inert state (actuation strategy I). Furthermore, an extended analysis using the OVMD method reveals that the dynamics at low-frequency actuation, near the shedding frequency, which correspond to the release of the large vortex cluster and scale with the height of the bump ($f^*_{jet} = \mathcal{O}(f^*_{shed})$) in strategy I, resembling those of Scenario 2. Moreover, at the optimum frequency, the dynamics are dominated by the formation of KH vortices, which enhance entrainment. Actuation strategy II, with a duty frequency in the range of the shedding frequency, exhibits dynamics similar to Scenario 3, confirming its potential as a superior strategy for controlling the separation region.

Chapter 9

Conclusions and future perspectives

This thesis investigates flow separation in setups resembling the flow over low-pressure turbine (LPT) blades at high-altitude cruising conditions (low Reynolds), aiming to understand the fundamental physical processes of separated flow and its reattachment under unsteady harmonic inflow and turbulent conditions, with a focus on developing potential flow control strategies. The research has led to the development of a novel method for analyzing fluid flows through mode decomposition and proposes an active actuation strategy to mitigate separation-associated losses on low-pressure turbine blades. Furthermore, the thesis demonstrates the capability of a high-order discontinuous Galerkin (DG) solver to accurately simulate unsteady and turbulent flows.

Flow simulations are performed using a high-order DG-Spectral Element Method solver, which is known for its superior accuracy in solving partial differential equations (PDEs) compared to low-order methods. No additional turbulence modeling is introduced into the compressible Navier-Stokes equations to avoid unphysical fluid behavior, particularly during separation. In the validation case, which consists of LNS simulations of disturbance evolution in Plane Poiseuille flow and turbulent channel flow, the high-order numerical simulations accurately match both the theoretical predictions of LST and the reference results for the turbulent channel flow. In simulations of laminar and turbulent boundary layer separation, the high-order approach successfully captures the key physical phenomena. Although this method entails significantly higher computational costs compared to low-order approaches, its use in complex fluid analyzes is highly beneficial.

One of the most significant contributions of this thesis is the development of a novel mode decomposition technique called Orthogonalized Variational Mode Decomposition (OVMD) (Chapters 4 and 5). This method demonstrates a substantial improvement over existing approaches in decomposing signals consisting of time-localized events, such as pulses or wave packets. Its extension to multichannel applications, e.g., multivariate and multi-dimensional flow fields, highlights its robustness and reasonable computational cost. The capability of progressive OVMD to produce orthogonal dominant modes in sequence is particularly advantageous for analyzing phenomena involving time-localized events or state transitions.

Another significant contribution of this thesis is the analysis of flow separation over a wall-

mounted bump geometry under harmonic inflow variations (Chapter 6). This setup mimics the periodic passage of upstream wakes in a multi-stage LPT. The study identifies three distinct scenarios depending on the amplitude and frequency of the inflow oscillations, highlighting the presence of large vortex clusters in two scenarios (Scenario 2 (alternation between KH vortices and formation/release of large vortex cluster) and 3 (phase-locked formation and release of large vortex clusters)) that effectively reduce the separation region. A criterion based on the local acceleration parameter K is derived to categorize the dynamics into the three identified scenarios. Extensive analyzes using the OVMD technique successfully distinguish the unique characteristics of each scenario and the distinct generation processes of the large vortex clusters. Additionally, OVMD captures time-localized phenomena, enabling a clear distinction between Scenarios 2 and 3.

The final contribution of this thesis proposes an alternative flow control strategy that aims at inducing the dynamics of Scenario 3 in a configuration with steady-inflow (Chapter 7). This novel approach, consisting of periodic blowing-suction cycles with an inert state (actuation strategy II), demonstrates the potential to match the optimum performance of periodic blowing-suction without an inert state (actuation strategy I). Furthermore, an extended analysis using the OVMD method reveals that the dynamics at low-frequency actuation, near the shedding frequency, which correspond to the release of the large vortex cluster and scale with the height of the bump ($f^*_{jet} = \mathcal{O}(f^*_{shed})$) in strategy I, resembling those of Scenario 2. Moreover, at the optimum frequency, the dynamics are dominated by the formation of KH vortices, which enhance entrainment. Actuation strategy II, with a duty frequency in the range of the shedding frequency, exhibits dynamics similar to Scenario 3, confirming its potential as a superior strategy for controlling the separation region.

To conclude the thesis, future research directions inspired by the findings of this work are proposed:

- Integrating OVMD analysis with machine learning methods has the potential to enhance physical understanding and provide insights into the non-linear relationships between modes in more chaotic flows (dominant incoherent parts).
- Integrating OVMD analysis with the CFD solver will enable the efficient application to the method to the investigation of three-dimensional phenomena in fluid flows, fostering new physical understanding, sensitivity analysis, novel control strategies, and/or innovative turbulence modeling. How simulation data is handled and processed will be critical for the development of this capability. The OVMD method itself has been demonstrated to provide accurate representations with minimal input data.
- Optimal criteria and conditions that effectively and efficiently promote large vortex clusters for flow control strategies. Other potential applications of large vortex clusters, beyond flow control, are equally compelling, such as in fluid mixing for combustion processes.

References

Ambrogi, F., Piomelli, U., & Rival, D. (2022). Characterization of unsteady separation in a turbulent boundary layer: Mean and phase-averaged flow. *Journal of Fluid Mechanics*, *945*, A10. https://doi.org/10.1017/jfm.2022.561

Aniffa, S. M., Caesar, V., Dabaria, V., & Mandal, A. (2023). Characteristics of geometry- and pressure-induced laminar separation bubbles at an enhanced level of free-stream turbulence. *Journal of Fluid Mechanics*, *957*, A19. https://doi.org/10.1017/jfm.2023.53

Avanci, M. P., Rodríguez, D., & Alves, L. S. B. (2019). A geometrical criterion for absolute instability in separated boundary layers. *Physics of Fluids*, *31*(1), 014103. https://doi.org/10.1063/1.5079536

Bagheri, S. (2013). Koopman-mode decomposition of the cylinder wake. *Journal of Fluid Mechanics*, *726*, 596–623. https://doi.org/10.1017/jfm.2013.249

Balin, R., & Jansen, K. (2021). Direct numerical simulation of a turbulent boundary layer over a bump with strong pressure gradients. *Journal of Fluid Mechanics*, *918*, A14. https://doi.org/10.1017/jfm.2021.312

Balzer, W., & Fasel, H. F. (2016). Numerical investigation of the role of free-stream turbulence in boundary-layer separation. *Journal of Fluid Mechanics*, *801*, 289–321. https://doi.org/10.1017/jfm.2016.424

Berkooz, G., Holmes, P., & Lumley, J. L. (1993). The proper orthogonal decomposition in the analysis of turbulent flows. *Annual Review of Fluid Mechanics*, *25*, 539–575. https://doi.org/10.1146/annurev.fl.25.010193.002543

Bernard, A., Foucaut, J. M., Dupont, P., & Stanislas, M. (2003). Decelerating boundary layer: A new scaling and mixing length model. *AIAA Journal*, *41*(2), 248–255. https://doi.org/10.2514/2.1937

Biferale, L., Musacchio, S., & Toschi, F. (2012). Inverse energy cascade in three-dimensional isotropic turbulence. *Physical Review Letters*, *108*, 164501. https://doi.org/10.1103/PhysRevLett.108.164501

Bons, J. P., Sondergaard, R., & Rivir, R. B. (2002). The fluid dynamics of LPT blade separation control using pulsed jets. *Journal of Turbomachinery*, *124*(1), 77–85. https://doi.org/10.1115/1.1425392

Boppana, V. B. L., & Gajjar, J. S. B. (2011). Onset of global instability in the flow past a circular cylinder cascade. *Journal of Fluid Mechanics*, *668*, 304–334. https://doi.org/10.1017/S0022112010004684

Bowen, A. J., & Lindley, D. (1977). A wind-tunnel investigation of the wind speed and turbulence characteristics close to the ground over various escarpment shapes. *Boundary-layer metereology*, *12*, 259–271. https://doi.org/10.1007/BF00121466

Brown, G. L., & Thomas, A. S. W. (1977). Large structure in a turbulent boundary layer. *The Physics of Fluids*, *20*(10), S243–S252. https://doi.org/10.1063/1.861737

Brun, C., Petrovan Boiarciuc, M., & Haberkorn, M. (2008). Large eddy simulation of compressible channel flow. *Theoretical and Computational Fluid Dynamics*, *22*, 189–212. https://doi.org/10.1007/s00162-007-0073-y

Carter, G., & Knapp, C. (1975). Coherence and its estimation via the partitioned modified chirp-z transform. *IEEE Transactions on Acoustics, Speech, and Signal Processing*, *23*(3), 257–264. https://doi.org/10.1109/TASSP.1975.1162684

Chatterjee, A. (2000). An introduction to the proper orthogonal decomposition. *Current Science*, *78*(7), 808–817.

Chen, Q., Lang, X., Xie, L., & Su, H. (2021). Multivariate intrinsic chirp mode decomposition. *Signal Processing*, *183*, 108009. https://doi.org/10.1016/j.sigpro.2021.108009

Chen, S., Dong, X., Peng, Z., Zhang, W., & Meng, G. (2017). Nonlinear chirp mode decomposition: A variational method. *IEEE Transactions on Signal Processing*, *65*(22), 6024–6037. https://doi.org/10.1109/TSP.2017.2731300

Cichy, R. M., & Pantazis, D. (2017). Multivariate pattern analysis of MEG and EEG: A comparison of representational structure in time and space. *NeuroImage*, *158*, 441–454. https://doi.org/10.1016/j.neuroimage.2017.07.023

Cicone, A., & Pellegrino, E. (2022). Multivariate fast iterative filtering for the decomposition of nonstationary signals. *IEEE Transactions on Signal Processing*, *70*, 1521–1531. https://doi.org/10.1109/TSP.2022.3157482

Cohen, E., & Gloerfelt, X. (2018). Influence of pressure gradients on wall pressure beneath a turbulent boundary layer. *Journal of Fluid Mechanics*, *838*, 715–758. https://doi.org/10.1017/jfm.2017.898

Coull, J. D., & Hodson, H. P. (2011). Unsteady boundary-layer transition in low-pressure turbines. *Journal of Fluid Mechanics*, *681*, 370–410. https://doi.org/10.1017/jfm.2011.204

Curtis, E. M., Hodson, H. P., Banieghbal, M. R., Denton, J. D., Howell, R. J., & Harvey, N. W. (1997). Development of blade profiles for low-pressure turbine applications. *Journal of Turbomachinery*, *119*(3), 531–538. https://doi.org/10.1115/1.2841154

Dandois, J., Garnier, E., & Sagaut, P. (2007). Numerical simulation of active separation control by a synthetic jet. *Journal of Fluid Mechanics*, *574*, 25–58. https://doi.org/10.1017/S0022112006003995

Das, K., & Pachori, R. B. (2021). Schizophrenia detection technique using multivariate iterative filtering and multichannel EEG signals. *Biomedical Signal Processing and Control*, *67*, 102525. https://doi.org/10.1016/j.bspc.2021.102525

Daubechies, I., Lu, J., & Wu, H.-T. (2011). Synchrosqueezed wavelet transforms: An empirical mode decomposition-like tool. *Applied and Computational Harmonic Analysis*, *30*(2), 243–261. https://doi.org/10.1016/j.acha.2010.08.002

Dellacasagrande, M., Basi, D., Lengani, D., Simoni, D., & Verdoya, J. (2020). Response of a flat plate laminar separation bubble to Reynolds number, free-stream turbulence and

adverse pressure gradient variation. *Experiments in Fluids*, *61*, 128. https://doi.org/10.1007/s00348-020-02958-y

Denton, J. D. (1993, May). *Loss mechanisms in turbomachines* (Vol. Volume 2: Combustion and Fuels; Oil and Gas Applications; Cycle Innovations; Heat Transfer; Electric Power; Industrial and Cogeneration; Ceramics; Structures and Dynamics; Controls, Diagnostics and Instrumentation; IGTI Scholar Award). https://doi.org/10.1115/93-GT-435

Diwan, S. S., & Ramesh, O. N. (2009). On the origin of the inflectional instability of a laminar separation bubble. *Journal of Fluid Mechanics*, *629*, 263–298. https://doi.org/10.1017/S002211200900634X

Diwan, S., Chetan, S., & Ramesh, O. (2006). On the bursting criterion for laminar separation bubbles. In R. Govindarajan (Ed.), *Iutam symposium on laminar-turbulent transition* (pp. 401–407). Springer Netherlands. https://doi.org/10.1007/1-4020-4159-4_57

Dovgal, A., Kozlov, V., & Michalke, A. (1994). Laminar boundary layer separation: Instability and associated phenomena. *Progress in Aerospace Sciences*, *30*(1), 61–94. https://doi.org/10.1016/0376-0421(94)90003-5

Dragomiretskiy, K., & Zosso, D. (2014). Variational mode decomposition. *IEEE Transactions on Signal Processing*, *62*(3), 531–544. https://doi.org/10.1109/TSP.2013.2288675

Duck, P. W., Ruban, A. I., Theofilis, V., Hein, S., & Dallmann, U. (2000). On the origins of unsteadiness and three-dimensionality in a laminar separation bubble. *Philosophical Transactions of the Royal Society of London. Series A: Mathematical, Physical and Engineering Sciences*, *358*(1777), 3229–3246. https://doi.org/10.1098/rsta.2000.0706

Embacher, M., & Fasel, H. F. (2014). Direct numerical simulations of laminar separation bubbles: Investigation of absolute instability and active flow control of transition to turbulence. *Journal of Fluid Mechanics*, *747*, 141–185. https://doi.org/10.1017/jfm.2014.123

Farge, M. (1992). Wavelet transforms and their applications to turbulence. *Annual Review of Fluid Mechanics*, *24*(1), 395–458. https://doi.org/10.1146/annurev.fl.24.010192.002143

Ferrer, E., Rubio, G., Ntoukas, G., Laskowski, W., Mariño, O., Colombo, S., Mateo-Gabín, A., Marbona, H., Manrique de Lara, F., Huergo, D., Manzanero, J., Rueda-Ramírez, A., Kopriva, D., & Valero, E. (2023). HORSES3D: A high-order discontinuous Galerkin solver for flow simulations and multi-physics applications. *Computer Physics Communications*, *287*, 108700. https://doi.org/10.1016/j.cpc.2023.108700

Gabay, D., & Mercier, B. (1976). A dual algorithm for the solution of nonlinear variational problems via finite element approximation. *Computers & Mathematics with Applications*, *2*(1), 17–40. https://doi.org/10.1016/0898-1221(76)90003-1

Gallaire, F., Marquillie, M., & Ehrenstein, U. (2007). Three-dimensional transverse instabilities in detached boundary layers. *Journal of Fluid Mechanics*, *571*, 221–233. https://doi.org/10.1017/S0022112006002898

Ganapathisubramani, B., Hutchins, N., Monty, J. P., Chung, D., & Marusic, I. (2012). Amplitude and frequency modulation in wall turbulence. *Journal of Fluid Mechanics*, *712*, 61–91. https://doi.org/10.1017/jfm.2012.398

Gaster, M. (1967, March). *The structure and behaviour of separation bubbles* (Reports and Memoranda No. 3595). Queen Mary College. London.

Gilles, J. (2013). Empirical wavelet transform. *IEEE Transactions on Signal Processing*, *61*(16), 3999–4010. https://doi.org/10.1109/TSP.2013.2265222

Greenblatt, D., Paschal, K. B., Yao, C.-S., Harris, J., Schaeffer, N. W., & Washburn, A. E. (2006). Experimental investigation of separation control Part 1: Baseline and steady suction. *AIAA Journal*, *44*(12), 2820–2830. https://doi.org/10.2514/1.13817

Greenblatt, D., Paschal, K. B., Yao, C.-S., & Harris, J. (2006). Experimental investigation of separation control part 2: Zero mass-flux oscillatory blowing. *AIAA Journal*, *44*(12), 2831–2845. https://doi.org/10.2514/1.19324

Greenblatt, D., & Wygnanski, I. J. (2000). The control of flow separation by periodic excitation. *Progress in Aerospace Sciences*, *36*, 487–545. https://doi.org/10.1016/S0376-0421(00)00008-7

Grossmann, A., & Morlet, J. (1984). Decomposition of hardy functions into square integrable wavelets of constant shape. *SIAM Journal on Mathematical Analysis*, *15*(4), 723–736. https://doi.org/10.1137/0515056

Gungor, A. G., Simens, M. P., & Jiménez, J. (2012). Direct numerical simulations of wake-perturbed separated boundary layers. *Journal of Turbomachinery*, *134*, 061024. https://doi.org/10.1115/1.4004882

Hammond, D., & Redekopp, L. (1998). Local and global instability properties of separation bubbles. *European Journal of Mechanics - B/Fluids*, *17*(2), 145–164. https://doi.org/10.1016/S0997-7546(98)80056-3

Hasan, M. A. Z. (1992). The flow over a backward-facing step under controlled perturbation: Laminar separation. *Journal of Fluid Mechanics*, *238*, 73–96. https://doi.org/10.1017/S0022112092001642

Himeno, F. H., Souza, D. S., Amaral, F. R., Rodríguez, D., & Medeiros, M. (2021). SPOD analysis of noise-generating Rossiter modes in a slat with and without a bulb seal. *Journal of Fluid Mechanics*, *915*, A67. https://doi.org/10.1017/jfm.2021.93

Hodson, H. P., & Howell, R. J. (2005). Bladerow interactions, transition and high-lift aerofoils in low-pressure turbine. *Annual Review of Fluid Mechanics*, *37*, 71–98. https://doi.org/10.1146/annurev.fluid.37.061903.175511

Hosseinverdi, S., & Fasel, H. (2018). Role of the Klebanoff modes in active flow control of separation: direct numerical simulation. *Journal of Fluid Mechanics*, *850*, 954–983. https://doi.org/10.1017/jfm.2018.489

Hosseinverdi, S., & Fasel, H. (2019). Numerical investigation of laminar-turbulent transition in laminar separation bubbles: the effect of free-stream turbulence. *Journal of Fluid Mechanics*, *858*, 714–759. https://doi.org/10.1017/jfm.2018.809

Hou, T. Y., & Shi, Z. (2011). Adaptive data analysis via sparse time-frequency representation. *Advances in Adaptive Data Analysis*, *3*, 1–28. https://doi.org/10.1142/S1793536911000647

Hourmouziadis, J. (1989). Aerodynamic design of low pressure turbines. In *AGARD Lecture Series No. 167 Blading Design for Axial Turbomachines* (pp. 8.1–8.40). AGARD.

Howell, R. J., Ramesh, O. N., Hodson, H. P., Harvey, N. W., & Schulte, V. (2000). High lift and aft-loaded profiles for low-pressure turbines. *Journal of Turbomachinery*, *123*(2), 181–188. https://doi.org/10.1115/1.1350409

Hoyas, S., & Jiménez, J. (2006). Scaling of the velocity fluctuations in turbulent channels up to $\mathrm{Re}_\tau = 2003$. *Physics of Fluids*, *18*(1), 011702. https://doi.org/10.1063/1.2162185

Hoyas, S., & Jiménez, J. (2008). Reynolds number effects on the Reynolds-stress budgets in turbulent channels. *Physics of Fluids*, *20*(10), 101511. https://doi.org/10.1063/1.3005862

Huang, N. E., Shen, Z., Long, S. R., Wu, M. C., Shih, H. H., Zheng, Q., Yen, N.-C., Tung, C. C., & Liu, H. H. (1998). The empirical mode decomposition and the hilbert spectrum for nonlinear and non-stationary time series analysis. *Proceedings of the Royal Society of London. Series A: Mathematical, Physical and Engineering Sciences*, *454*(1971), 903–995. https://doi.org/10.1098/rspa.1998.0193

Hussain, A. K. M. F., & Reynolds, W. C. (1970). The mechanics of an organized wave in turbulent shear flow. *Journal of Fluid Mechanics*, *41*(2), 241–258. https://doi.org/10.1017/S0022112070000605

Jackson, C. P. (1987). A finite-element study of the onset of vortex shedding in flow past variously shaped bodies. *Journal of Fluid Mechanics*, *182*, 23–45. https://doi.org/10.1017/S0022112087002234

Jacobs, R. G., & Durbin, P. A. (2001). Simulations of bypass transition. *Journal of Fluid Mechanics*, *428*, 185–212. https://doi.org/10.1017/S0022112000002469

Jeong, J., & Hussain, F. (1995). On the identification of a vortex. *Journal of Fluid Mechanics*, *285*, 69–94. https://doi.org/10.1017/S0022112095000462

Jiang, H., & Cheng, L. (2017). Strouhal–Reynolds number relationship for flow past a circular cylinder. *Journal of Fluid Mechanics*, *832*, 170–188. https://doi.org/10.1017/jfm.2017.685

Karaca, S., & Gungor, A. (2016). DNS of unsteady effects on the control of laminar separated boundary layers. *European Journal of Mechanics - B/Fluids*, *56*, 71–81. https://doi.org/10.1016/j.euromechflu.2015.11.007

Kiya, M., Shimizu, M., & Mochizuki, O. (1997). Sinusoidal forcing of a turbulent separation bubble. *Journal of Fluid Mechanics*, *342*, 119–139. https://doi.org/10.1017/S0022112097005521

Kopriva, D. (2009). Implementing spectral methods for partial differential equations: Algorithms for scientists and engineers. Springer Science Business Media.

Kopriva, D., Winters, A. R., Schlottke-Lakemper, M., Schoonover, J. A., & Ranocha, H. (2024). Hohqmesh: An all quadrilateral/hexahedral unstructured mesh generator for high order elements. *Journal of Open Source Software*, *9*(104), 7476. https://doi.org/10.21105/joss.07476

Kurelek, J. W., Yarusevych, S., & Kotsonis, M. (2019). Vortex merging in a laminar separation bubble under natural and forced conditions. *Phys. Rev. Fluids*, *4*, 063903. https://doi.org/10.1103/PhysRevFluids.4.063903

Laskowski, W. (2022, September). *Efficient solvers for steady and unsteady high-order compressible flow simulations* [Doctoral dissertation, Universidad Politécnica de Madrid - School of Aeronautics (ETSIAE)]. https://doi.org/10.20868/UPM.thesis.72084

Launder, B. E. (1964). Laminarization of the turbulent boundary layer in a severe acceleration. *Journal of Applied Mechanics*, *31*(4), 707–708. https://doi.org/10.1115/1.3629738

Legleiter, C., & Kyriakidis, P. (2006). Forward and inverse transformations between cartesian and channel-fitted coordinate systems for meandering rivers. *Mathematical Geology*, *38*, 927–958. https://doi.org/10.1007/s11004-006-9056-6

Liao, Z.-M., Zhao, Z., Chen, L.-B., Wan, Z.-H., Liu, N.-S., & Lu, X.-Y. (2023). Reduced-order variational mode decomposition to reveal transient and non-stationary dynamics in fluid flows. *Journal of Fluid Mechanics*, *966*, A7. https://doi.org/10.1017/jfm.2023.435

Lighthill, M. J. (1963). Introduction. boundary layer theory. In L. Rosenhead (Ed.), *Laminar boundary layers* (pp. 46–113). Clarendon Press.

Lilly, J. M., & Olhede, S. C. (2012). Analysis of modulated multivariate oscillations. *IEEE Transactions on Signal Processing*, *60*(2), 600–612. https://doi.org/10.1109/TSP.2011.2173681

Lind, A. H., & Jones, A. R. (2016). Unsteady aerodynamics of reverse flow dynamic stall on an oscillating blade section. *Physics of Fluids*, *28*(7), 077102. https://doi.org/10.1063/1.4958334

Lou, W., & Hourmouziadis, J. (2000). Separation Bubbles Under Steady and Periodic-Unsteady Main Flow Conditions. *Journal of Turbomachinery*, *122*(4), 634–643. https://doi.org/10.1115/1.1308568

Lumley, J. (1970). *Stochastic tools in turbulence*. Academic Press.

Ma, H.-L., & Kuo, C.-H. (2017). Theoretical analysis of an oscillatory plane Poiseuille flow—A link to the design of vortex flow meter. *Physics of Fluids*, *29*(5), 053602. https://doi.org/10.1063/1.4984006

Manzanero Torrico, J. (2020, January). *A high-order discontinuous galerkin multiphase flow solver for industrial applications* [Doctoral dissertation, Universidad Politécnica de Madrid - School of Aeronautics (ETSIAE)]. https://doi.org/10.20868/UPM.thesis.65136

Marbona, H., Rodríguez, D., Martínez-Cava, A., & Valero, E. (2024). Impact of harmonic inflow variations on the size and dynamics of the separated flow over a bump. *Physical Review Fluids*, *9*, 053901. https://doi.org/10.1103/PhysRevFluids.9.053901

Marbona, H., Rodríguez, D., Martínez-Cava, A., Valero, E., Vandenhoeck, R., & Puri, K. (2024). Large-eddy simulations of a turbulent boundary layer separation over a bump with strong pressure gradients and freestream turbulence. In *Aiaa aviation forum and ascend 2024*. AIAA Aviation. https://doi.org/10.2514/6.2024-4530

Mariño Sánchez, O. Á. (2024, July). *High order methods for the generation and propagation of wind turbine aeroacoustics* [Doctoral dissertation, Universidad Politécnica de Madrid - School of Aeronautics (ETSIAE)]. https://doi.org/10.20868/UPM.thesis.81980

Marquillie, M., & Ehrenstein, U. (2003). On the onset of nonlinear oscillations in a separating boundary-layer flow. *Journal of Fluid Mechanics*, *490*, 169–188. https://doi.org/10.1017/S0022112003005287

Marxen, O., Lang, M., & Rist, U. (2013). Vortex formation and vortex breakup in laminar separation bubbles. *Journal of Fluid Mechanics*, *728*, 58–90. https://doi.org/10.1017/jfm.2013.222

Marxen, O., Lang, M., Rist, U., Levin, O., & Henningson, D. (2009). Mechanisms for spatial steady three-dimensional disturbance growth in a non-parallel and separating boundary layer. *Journal of Fluid Mechanics*, *634*, 165–189. https://doi.org/10.1017/S0022112009007149

Matai, R., & Durbin, P. (2019). Large-eddy simulation of turbulent flow over a parametric set of bumps. *Journal of Fluid Mechanics*, *866*, 503–525. https://doi.org/10.1017/jfm.2019.80

Mateo Gabín, A. (2024, February). *High-order numerical methods for the simulation of supersonic flows* [Doctoral dissertation, Universidad Politécnica de Madrid - School of Aeronautics (ETSIAE)]. https://doi.org/10.20868/UPM.thesis.81149

Mayle, R. E. (1991). The 1991 IGTI Scholar Lecture: The Role of Laminar-Turbulent Transition in Gas Turbine Engines. *Journal of Turbomachinery*, *113*(4), 509–536. https://doi.org/10.1115/1.2929110

McAuliffe, B. R., & Yaras, M. I. (2009). Transition mechanisms in separation bubbles under low- and elevated-freestream turbulence. *Journal of Turbomachinery*, *132*(1), 011004. https://doi.org/10.1115/1.2812949

Morlet, J., Arens, G., Fourgeau, E., & Giard, D. (1982a). Wave propagation and sampling theory—Part I: Complex signal and scattering in multilayered media. *GEOPHYSICS*, *47*(2), 203–221. https://doi.org/10.1190/1.1441328

Morlet, J., Arens, G., Fourgeau, E., & Giard, D. (1982b). Wave propagation and sampling theory—part ii: Sampling theory and complex waves. *GEOPHYSICS*, *47*(2), 222–236. https://doi.org/10.1190/1.1441329

Nazari, M., & Sakhaei, S. M. (2020). Successive variational mode decomposition. *Signal Processing*, *174*, 107610. https://doi.org/10.1016/j.sigpro.2020.107610

Nishioka, M., & Sato, H. (1978). Mechanism of determination of the shedding frequency of vortices behind a cylinder at low Reynolds numbers. *Journal of Fluid Mechanics*, *89*(1), 49–60. https://doi.org/10.1017/S0022112078002451

Noack, B. R. (2016). From snapshots to modal expansions – bridging low residuals and pure frequencies. *Journal of Fluid Mechanics*, *802*, 1–4. https://doi.org/10.1017/jfm.2016.416

Noack, B. R., Stankiewicz, W., Morzyński, M., & Schmid, P. J. (2016). Recursive dynamic mode decomposition of transient and post-transient wake flows. *Journal of Fluid Mechanics*, *809*, 843–872. https://doi.org/10.1017/jfm.2016.678

Nordström, J., Nordin, N., & Henningson, D. (1999). The fringe region technique and the fourier method used in the direct numerical simulation of spatially evolving viscous flows. *SIAM Journal on Scientific Computing*, *20*(4), 1365–1393. https://doi.org/10.1137/S1064827596310251

Nowak, H. D., Lluesma-Rodriguez, F., Rahbari, I., Clark, J. P., & Paniagua, G. (2022). Response of separated boundary layers to steady and pulsated flow injection [061001]. *Journal of Turbomachinery*, *145*(6). https://doi.org/10.1115/1.4056184

Ntoukas, G. (2023, March). *Robust and adaptive high-order discontinuous galerkin methods for multiphase flows* [Doctoral dissertation, Universidad Politécnica de Madrid - School of Aeronautics (ETSIAE)]. https://doi.org/10.20868/UPM.thesis.73311

Padilla-Montero, I., Rodríguez, D., Jaunet, V., & Jordan, P. (2024). Eduction of coherent structures from schlieren images of twin jets using SPOD informed with momentum potential theory in the spectral domain. *Theoretical and Computational Fluid Dynamics*, *38*(3), 375–401. https://doi.org/10.1007/s00162-024-00699-w

Passaggia, P.-Y., Leweke, T., & Ehrenstein, U. (2012). Transverse instability and low-frequency flapping in incompressible separated boundary layer flows: An experimental study. *Journal of Fluid Mechanics*, *703*, 363–373. https://doi.org/10.1017/jfm.2012.225

Patel, V. C. (1965). Calibration of the preston tube and limitations on its use in pressure gradients. *Journal of Fluid Mechanics*, *23*(1), 185–208. https://doi.org/10.1017/S0022112065001301

Pescini, E., Marra, F., De Giorgi, M., Francioso, L., & Ficarella, A. (2017). Investigation of the boundary layer characteristics for assessing the DBD plasma actuator control of the separated flow at low Reynolds numbers. *Experimental Thermal and Fluid Science*, *81*, 482–498. https://doi.org/10.1016/j.expthermflusci.2016.09.005

Postl, D., Balzer, W., & Fasel, H. F. (2011). Control of laminar separation using pulsed vortex generator jets: Direct numerical simulations. *Journal of Fluid Mechanics*, *676*, 81–109. https://doi.org/10.1017/jfm.2011.34

Prakash, A., Balin, R., Evans, J. A., & Jansen, K. E. (2024). A streamline coordinate analysis of a turbulent boundary layer subject to pressure gradients and curvature on the windward side of a bump. *Journal of Fluid Mechanics*, *984*, A23. https://doi.org/10.1017/jfm.2024.199

Price, M. (2018, July). *Current and emerging trends in the aerospace sector* (White Paper). SNC-Lavalin's Atkins.

Rehman, N., & Mandic, D. P. (2010). Multivariate empirical mode decomposition. *Proceedings of the Royal Society A: Mathematical, Physical and Engineering Sciences*, *466*(2117), 1291–1302. https://doi.org/10.1098/rspa.2009.0502

Rehman, N., & Aftab, H. (2019). Multivariate variational mode decomposition. *IEEE Transactions on Signal Processing*, *67*(23), 6039–6052. https://doi.org/10.1109/TSP.2019.2951223

Rist, U., & Maucher, U. (2002). Investigations of time-growing instabilities in laminar separation bubbles. *European Journal of Mechanics - B/Fluids*, *21*(5), 495–509. https://doi.org/10.1016/S0997-7546(02)01205-0

Rodríguez, D., & Gennaro, E. M. (2019). Enhancement of disturbance wave amplification due to the intrinsic three-dimensionalisation of laminar separation bubbles. *The Aeronautical Journal*, *123*(1268), 1492–1507. https://doi.org/10.1017/aer.2018.115

Rodríguez, D., Gennaro, E. M., & Juniper, M. P. (2013). The two classes of primary modal instability in laminar separation bubbles. *Journal of Fluid Mechanics*, *734*, R4. https://doi.org/10.1017/jfm.2013.504

Rodríguez, D., Gennaro, E. M., & Souza, L. F. (2021). Self-excited primary and secondary instability of laminar separation bubbles. *Journal of Fluid Mechanics*, *906*, A13. https://doi.org/10.1017/jfm.2020.767

Rodríguez, D., & Theofilis, V. (2010). Structural changes of laminar separation bubbles induced by global linear instability. *Journal of Fluid Mechanics*, *655*, 280–305. https://doi.org/10.1017/S0022112010000856

Rolls-Royce. (1996). *The jet engine* (Fifth Edition).

Rueda-Ramírez, A. (2019, September). *Efficient space and time solution techniques for high-order discontinuous galerkin discretizations of the 3d compressible navier-stokes equations* [Doctoral dissertation, Universidad Politécnica de Madrid - School of Aeronautics (ETSIAE)]. https://doi.org/10.20868/UPM.thesis.57182

Saavedra, J., & Paniagua, G. (2018). Transient performance of separated flows: Characterization and active flow control [011002]. *Journal of Engineering for Gas Turbines and Power*, *141*(1). https://doi.org/10.1115/1.4040685

Saavedra, J., & Paniagua, G. (2021). Experimental analysis of Reynolds effect on flow detachment and sudden flow release on a wall-mounted hump. *Experimental Thermal and Fluid Science*, *126*, 110398. https://doi.org/10.1016/j.expthermflusci.2021.110398

Schmid, P. J. (2010). Dynamic mode decomposition of numerical and experimental data. *Journal of Fluid Mechanics*, *656*, 5–28. https://doi.org/10.1017/S0022112010001217

Schmid, P. J., & Brandt, L. (2014). Analysis of fluid systems: stability, receptivity, sensitivity: Lecture notes from the FLOW-NORDITA summer school on advanced instability methods for complex flows, Stockholm, Sweden, 2013. *Applied Mechanics Reviews*, *66*(2), 024803. https://doi.org/10.1115/1.4026375

Schubauer, G. B., & Klebanoff, P. S. (1951, January). *Investigation of Separation of the Turbulent Boundary Layer* (NACA Report No. NACA-TR-1030). National Advisory Comittee for Aeronautics. California.

Seifert, A., Bachar, T., Koss, D., Shepshelovich, M., & Wygnanski, I. (1993). Oscillatory blowing: A tool to delay boundary-layer separation. *AIAA Journal*, *31*(11), 2052–2060. https://doi.org/10.2514/3.49121

Seifert, A., & Pack, L. G. (2002). Active flow separation control on wall-mounted hump at high Reynolds numbers. *AIAA Journal*, *40*(7), 1363–1372. https://doi.org/10.2514/2.1796

Shapiro, J. (1993). Embedded image coding using zerotrees of wavelet coefficients. *IEEE Transactions on Signal Processing*, *41*(12), 3445–3462. https://doi.org/10.1109/78.258085

Sieber, M., Paschereit, C. O., & Oberleithner, K. (2016). Spectral proper orthogonal decomposition. *Journal of Fluid Mechanics*, *792*, 798–828. https://doi.org/10.1017/jfm.2016.103

Siegel, S. G., Seidel, J., Fagley, C., Luchtenburg, D. M., Cohen, K., & McLaughlin, T. (2008). Low-dimensional modelling of a transient cylinder wake using double proper orthogonal decomposition. *Journal of Fluid Mechanics*, *610*, 1–42. https://doi.org/10.1017/S0022112008002115

Sigurdson, L. W. (1995). The structure and control of a turbulent reattaching flow. *Journal of Fluid Mechanics*, *298*, 139–165. https://doi.org/10.1017/S0022112095003259

Simoni, D., Lengani, D., Ubaldi, M., Zunino, P., & Dellacasagrande, M. (2017). Inspection of the dynamic properties of laminar separation bubbles: free-stream turbulence intensity effects for different Reynolds numbers. *Experiments in Fluids*, *58*(6), 66. https://doi.org/10.1007/s00348-017-2353-7

Spalart, P. (1989). Direct numerical study of leading-edge contamination. *"Fluid Dynamics of 3D Turbulent Shear Flows and Transition"*, (438), 5.1–5.13.

Spalart, P. R. (1986a, February). *Numerical simulation of boundary layers: Part 3. Turbulence and relaminarization in sink flows* (NASA Technical Memorandum No. 88220). NASA Ames Research Center. California.

Spalart, P. R., & Watmuff, J. H. (1993). Experimental and numerical study of a turbulent boundary layer with pressure gradients. *Journal of Fluid Mechanics*, *249*, 337–371. https://doi.org/10.1017/S002211209300120X

Spalart, P. R. (1986b). Numerical study of sink-flow boundary layers. *Journal of Fluid Mechanics*, *172*, 307–328. https://doi.org/10.1017/S0022112086001751

Spalding, D. B. (1961). A Single Formula for the "Law of the Wall". *Journal of Applied Mechanics*, *28*(3), 455–458. https://doi.org/10.1115/1.3641728

Suzen, Y. B., Huang, P., Hultgren, L. S., & Ashpis, D. E. (2003). Predictions of separated and transitional boundary layers under low-pressure turbine airfoil conditions using an intermittency transport equation. *Journal of Turbomachinery*, *125*, 455–464. https://doi.org/10.1115/1.1580159

Thomas, L. H. (1953). The stability of plane Poiseuille flow. *Physical Review*, *91*, 780–783. https://doi.org/10.1103/PhysRev.91.780

Towne, A., Schmidt, O. T., & Colonius, T. (2018). Spectral proper orthogonal decomposition and its relationship to dynamic mode decomposition and resolvent analysis. *Journal of Fluid Mechanics*, *847*, 821–867. https://doi.org/10.1017/jfm.2018.283

Uzun, A., & Malik, M. R. (2022). High-fidelity simulation of turbulent flow past gaussian bump. *AIAA Journal*, *60*(4), 2130–2149. https://doi.org/10.2514/1.J060760

Volino, R. J. (2012). Effect of unsteady wakes on boundary layer separation on a very high lift low pressure turbine flow. *Journal of Turbomachinery*, *134*, 011011. https://doi.org/10.1115/1.4003232

Volino, R. J., Kartuzova, O., & Ibrahim, M. B. (2011). Separation control on a very high lift low pressure turbine airfoil using pulsed vortex generator jets. *Journal of Turbomachinery*, *133*(4). https://doi.org/10.1115/1.4003024

Walker, J. (2006). Wavelet-based image processing. *Applicable Analysis*, *85*. https://doi.org/10.1080/00036810500358874

Welch, P. (1967). The use of fast fourier transform for the estimation of power spectra: A method based on time averaging over short, modified periodograms. *IEEE Transactions on Audio and Electroacoustics*, *15*(2), 70–73. https://doi.org/10.1109/TAU.1967.1161901

White, L., & Boashash, B. (1990). Cross spectral analysis of nonstationary processes. *IEEE Transactions on Information Theory*, *36*(4), 830–835. https://doi.org/10.1109/18.53742

Wissink, J. G., & Rodi, W. (2003). DNS of a laminar separation bubble in the presence of oscillating flow. *Flow Turbulence and Combustion*, *71*, 311–331. https://doi.org/10.1023/B:APPL.0000014917.71180.f1

Wissink, J. (2006). Separating, transitional flow affected by various inflow oscillation regimes. *Applied Mathematical Modelling*, *30*(10), 1134–1142. https://doi.org/10.1016/j.apm.2005.02.016

Xu, H., Guerrier, S., Molinari, R. C., & Karemera, M. (2019). Multivariate signal modeling with applications to inertial sensor calibration. *IEEE Transactions on Signal Processing*, *67*(19), 5143–5152. https://doi.org/10.1109/TSP.2019.2935902

Yang, T., Yang, Z., Li, F., & Wang, H. (2024). A short-term wind power forecasting method based on multivariate signal decomposition and variable selection. *Applied Energy*, *360*, 122759. https://doi.org/10.1016/j.apenergy.2024.122759

Zerva, M. C. H., Christou, V., Giannakeas, N., Tzallas, A. T., & Kondi, L. P. (2023). An improved medical image compression method based on wavelet difference reduction. *IEEE Access*, *11*, 18026–18037. https://doi.org/10.1109/ACCESS.2023.3246948

Annexes

This page is intentionally left blank

A. Compressible Navier-Stokes in Horses3D

A.1. Navier-Stokes equations

The compressible Navier-Stokes equations are expressed in HORSES3D code in conservative form as:

$$\frac{\partial \mathbf{q}}{\partial t} + \vec{\nabla} \cdot \left(\vec{\mathbf{f}}^a - \vec{\mathbf{f}}^v \right) = \mathbf{s} \tag{1}$$

where $\mathbf{q} = [\rho, \rho u, \rho v, \rho w, \rho E]^T$, also known as conservative variables for 3D flow. Note that all variables are written in non-dimensional form and normalized with reference values. The fluxes for advection, $\mathbf{f}^a$, and viscous, $\mathbf{f}^v$, are written in primitive variables as follows:

$$\mathbf{f}_1^a = \begin{bmatrix} \rho u \\ p + \rho u^2 \\ \rho uv \\ \rho uw \\ u(\rho E + p) \end{bmatrix} \quad , \quad \mathbf{f}_2^a = \begin{bmatrix} \rho v \\ \rho uv \\ p + \rho v^2 \\ \rho vw \\ v(\rho E + p) \end{bmatrix} \quad , \quad \mathbf{f}_3^a = \begin{bmatrix} \rho w \\ \rho uw \\ \rho vw \\ p + \rho w^2 \\ w(\rho E + p) \end{bmatrix} \tag{2}$$

$$\mathbf{f}_1^v = \frac{1}{Re_\infty} \begin{bmatrix} 0 \\ \tau_{xx} \\ \tau_{xy} \\ \tau_{xz} \\ v_i \tau_{1i} + \kappa \partial_x T \end{bmatrix} \quad , \quad \mathbf{f}_2^v = \frac{1}{Re_\infty} \begin{bmatrix} 0 \\ \tau_{yx} \\ \tau_{yy} \\ \tau_{yz} \\ v_i \tau_{2i} + \kappa \partial_y T \end{bmatrix} \quad , \quad \mathbf{f}_3^v = \frac{1}{Re_\infty} \begin{bmatrix} 0 \\ \tau_{zx} \\ \tau_{zy} \\ \tau_{zz} \\ v_i \tau_{3i} + \kappa \partial_z T \end{bmatrix}, \tag{3}$$

some relation for primitive variables:

$$p = (\gamma - 1)\, \rho \left[E - \frac{u^2 + v^2 + w^2}{2} \right] \tag{4}$$

$$\mu = \frac{1 + T_{suth}/T_\infty}{T + T_{suth}/T_\infty} T^{\frac{3}{2}}, \tag{5}$$

where $T_{suth} = 110.4K$ and T_∞ is the reference value for the temperature. The pressure p

and the dynamic viscosity μ are non-dimensional. Equation 5 is the Sutherland´s law. The non-dimensional thermal conductivity can be expressed as:

$$\kappa = \frac{\mu}{(\gamma - 1)\, Pr\; M_{ref}}, \tag{6}$$

where Pr is the Prandtl number, assumed to be constant. The stress tensor is expressed using the Stokes hypothesis as

$$\underline{\tau} = \mu \left(\left(\vec{\nabla} \vec{v} \right)^T + \vec{\nabla} \vec{v} \right) - \frac{2}{3} \mu \left(\vec{\nabla} \cdot \vec{v} \underline{\mathbf{I}} \right). \tag{7}$$

The temperature is calculated with ideal gas relation:

$$T = \gamma M_{ref}^2 \frac{p}{\rho} \tag{8}$$

Equation (7) is non-dimensional and results of $p_{ref} = (M_{ref})^2 \gamma \rho_{ref} R T_{ref}$, which is used to define the non-dimensional pressure. Hence, the non-dimensional reference static pressure is $p_{amb} = \frac{1}{\gamma M_{ref}^2}$.

A.2. Advection flux - conservative variables

The advection flux can be expressed using conservative variables by defining the primitive variable as conservative variables such as:

$$u = \frac{q_2}{q_1}\ , \quad v = \frac{q_3}{q_1}\ , \quad w = \frac{q_4}{q_1} \tag{9}$$

$$p = (\gamma - 1) \left[q_5 - \frac{1}{2} \left(\frac{q_2^2}{q_1} + \frac{q_3^2}{q_1} + \frac{q_4^2}{q_1} \right) \right]. \tag{10}$$

The expressions for the advection flux are as follows:

$$\mathbf{f}_1^a = \begin{bmatrix} q_2 \\ \frac{q_2^2}{q_1} + (\gamma - 1) \left[q_5 - \frac{1}{2} \left(\frac{q_2^2}{q_1} + \frac{q_3^2}{q_1} + \frac{q_4^2}{q_1} \right) \right] \\ \frac{q_2 q_3}{q_1} \\ \frac{q_2 q_4}{q_1} \\ \frac{q_2}{q_1} \left[\gamma\ q_5 - \frac{(\gamma-1)}{2} \left(\frac{q_2^2}{q_1} + \frac{q_3^2}{q_1} + \frac{q_4^2}{q_1} \right) \right] \end{bmatrix} \quad , \quad \mathbf{f}_2^a = \begin{bmatrix} q_3 \\ \frac{q_2 q_3}{q_1} \\ \frac{q_3^2}{q_1} + (\gamma - 1) \left[q_5 - \frac{1}{2} \left(\frac{q_2^2}{q_1} + \frac{q_3^2}{q_1} + \frac{q_4^2}{q_1} \right) \right] \\ \frac{q_3 q_4}{q_1} \\ \frac{q_3}{q_1} \left[\gamma\ q_5 - \frac{(\gamma-1)}{2} \left(\frac{q_2^2}{q_1} + \frac{q_3^2}{q_1} + \frac{q_4^2}{q_1} \right) \right] \end{bmatrix}$$

$$\mathbf{f}_3^a = \begin{bmatrix} q_4 \\ \frac{q_2 q_4}{q_1} \\ \frac{q_3 q_4}{q_1} \\ \frac{q_4^2}{q_1} + (\gamma - 1) \left[q_5 - \frac{1}{2} \left(\frac{q_2^2}{q_1} + \frac{q_3^2}{q_1} + \frac{q_4^2}{q_1} \right) \right] \\ \frac{q_4}{q_1} \left[\gamma\ q_5 - \frac{(\gamma-1)}{2} \left(\frac{q_2^2}{q_1} + \frac{q_3^2}{q_1} + \frac{q_4^2}{q_1} \right) \right] \end{bmatrix} \tag{11}$$

A.3. Viscous flux - conservative variables

Similar to the advection flux, the viscous flux can be expressed as conservative variables by deriving the primitive variables in a conservative form. The velocity gradient in the x-direction can be written as follows:

$$\begin{aligned}
\frac{\partial u}{\partial x} &= \frac{\partial \left(\frac{q_2}{q_1}\right)}{\partial x} = \frac{1}{q_1}\frac{\partial q_2}{\partial x} - \frac{q_2}{q_1^2}\frac{\partial q_1}{\partial x} \\
\frac{\partial v}{\partial x} &= \frac{\partial \left(\frac{q_3}{q_1}\right)}{\partial x} = \frac{1}{q_1}\frac{\partial q_3}{\partial x} - \frac{q_3}{q_1^2}\frac{\partial q_1}{\partial x}. \\
\frac{\partial w}{\partial x} &= \frac{\partial \left(\frac{q_4}{q_1}\right)}{\partial x} = \frac{1}{q_1}\frac{\partial q_4}{\partial x} - \frac{q_4}{q_1^2}\frac{\partial q_1}{\partial x}
\end{aligned} \tag{12}$$

The concepts for the y- and z-directions follow a similar approach.

Temperature can be expressed in terms of the conservative variables as follows:

$$T = (\gamma^2 - \gamma) M_{ref}^2 \left[\frac{q_5}{q_1} - \frac{1}{2}\left(\frac{q_2^2}{q_1^2} + \frac{q_3^2}{q_1^2} + \frac{q_4^2}{q_1^2}\right)\right]. \tag{13}$$

Its partial derivative in x direction is:

$$\begin{aligned}
\frac{\partial T}{\partial x} &= (\gamma^2 - \gamma) M_{ref}^2 \frac{\partial \left[\frac{q_5}{q_1} - \frac{1}{2}\left(\frac{q_2^2}{q_1^2} + \frac{q_3^2}{q_1^2} + \frac{q_4^2}{q_1^2}\right)\right]}{\partial x} \\
&= (\gamma^2 - \gamma) M_{ref}^2 \left[\frac{\partial \left(\frac{q_5}{q_1}\right)}{\partial x} - \frac{1}{2}\left(\frac{\partial \left(\frac{q_2^2}{q_1^2}\right)}{\partial x} + \frac{\partial \left(\frac{q_3^2}{q_1^2}\right)}{\partial x} + \frac{\partial \left(\frac{q_4^2}{q_1^2}\right)}{\partial x}\right)\right] \\
&= (\gamma^2 - \gamma) M_{ref}^2 \left[\frac{\partial \left(\frac{q_5}{q_1}\right)}{\partial x} - \frac{q_2}{q_1}\frac{\partial \left(\frac{q_2}{q_1}\right)}{\partial x} - \frac{q_3}{q_1}\frac{\partial \left(\frac{q_3}{q_1}\right)}{\partial x} - \frac{q_4}{q_1}\frac{\partial \left(\frac{q_4}{q_1}\right)}{\partial x}\right] \\
&= (\gamma^2 - \gamma) M_{ref}^2 \left[\frac{1}{q_1}\frac{\partial q_5}{\partial x} - \frac{q_5}{q_1^2}\frac{\partial q_1}{\partial x} - \frac{q_2}{q_1}\left(\frac{1}{q_1}\frac{\partial q_2}{\partial x} - \frac{q_2}{q_1^2}\frac{\partial q_1}{\partial x}\right)\right. \\
&\qquad \left. - \frac{q_3}{q_1}\left(\frac{1}{q_1}\frac{\partial q_3}{\partial x} - \frac{q_3}{q_1^2}\frac{\partial q_1}{\partial x}\right) - \frac{q_4}{q_1}\left(\frac{1}{q_1}\frac{\partial q_4}{\partial x} - \frac{q_4}{q_1^2}\frac{\partial q_1}{\partial x}\right)\right] \\
&= (\gamma^2 - \gamma) M_{ref}^2 \left[\left(\frac{1}{q_1}\frac{\partial q_5}{\partial x} - \frac{q_4}{q_1^2}\frac{\partial q_4}{\partial x} - \frac{q_3}{q_1^2}\frac{\partial q_3}{\partial x} - \frac{q_2}{q_1^2}\frac{\partial q_2}{\partial x}\right) + \right. \\
&\qquad \left. \left(\frac{q_2^2}{q_1^3} + \frac{q_3^2}{q_1^3} + \frac{q_4^2}{q_1^3} - \frac{q_5}{q_1^2}\right)\frac{\partial q_1}{\partial x}\right]
\end{aligned} \tag{14}$$

The partial derivatives of T in y and z-direction are:

$$\frac{\partial T}{\partial y} = (\gamma^2 - \gamma) M_{ref}^2 \left[\left(\frac{1}{q_1} \frac{\partial q_5}{\partial y} - \frac{q_4}{q_1^2} \frac{\partial q_4}{\partial y} - \frac{q_3}{q_1^2} \frac{\partial q_3}{\partial y} - \frac{q_2}{q_1^2} \frac{\partial q_2}{\partial y} \right) + \left(\frac{q_2^2}{q_1^3} + \frac{q_3^2}{q_1^3} + \frac{q_4^2}{q_1^3} - \frac{q_5}{q_1^2} \right) \frac{\partial q_1}{\partial y} \right] \tag{15}$$

$$\frac{\partial T}{\partial z} = (\gamma^2 - \gamma) M_{ref}^2 \left[\left(\frac{1}{q_1} \frac{\partial q_5}{\partial z} - \frac{q_4}{q_1^2} \frac{\partial q_4}{\partial z} - \frac{q_3}{q_1^2} \frac{\partial q_3}{\partial z} - \frac{q_2}{q_1^2} \frac{\partial q_2}{\partial z} \right) + \left(\frac{q_2^2}{q_1^3} + \frac{q_3^2}{q_1^3} + \frac{q_4^2}{q_1^3} - \frac{q_5}{q_1^2} \right) \frac{\partial q_1}{\partial z} \right] \tag{16}$$

The expanded viscous flux for 3D flow is as follows:

$$\mathbf{f}_1^v = \frac{1}{Re_\infty} \begin{bmatrix} 0 \\ \mu \left(2 \frac{\partial u}{\partial x} - \frac{2}{3} \left(\frac{\partial u}{\partial x} + \frac{\partial v}{\partial y} + \frac{\partial w}{\partial z} \right) \right) \\ \mu \left(\frac{\partial u}{\partial y} + \frac{\partial v}{\partial x} \right) \\ \mu \left(\frac{\partial u}{\partial z} + \frac{\partial w}{\partial x} \right) \\ \mu \left[\frac{q_2}{q_1} \left(\frac{4}{3} \frac{\partial u}{\partial x} - \frac{2}{3} \left(\frac{\partial v}{\partial y} + \frac{\partial w}{\partial z} \right) \right) + \frac{q_3}{q_1} \left(\frac{\partial u}{\partial y} + \frac{\partial v}{\partial x} \right) + \frac{q_4}{q_1} \left(\frac{\partial u}{\partial z} + \frac{\partial w}{\partial x} \right) \right] + \kappa \frac{\partial T}{\partial x} \end{bmatrix}$$

$$\mathbf{f}_2^v = \frac{1}{Re_\infty} \begin{bmatrix} 0 \\ \mu \left(\frac{\partial u}{\partial y} + \frac{\partial v}{\partial x} \right) \\ \mu \left(2 \frac{\partial v}{\partial y} - \frac{2}{3} \left(\frac{\partial u}{\partial x} + \frac{\partial v}{\partial y} + \frac{\partial w}{\partial z} \right) \right) \\ \mu \left(\frac{\partial v}{\partial z} + \frac{\partial w}{\partial y} \right) \\ \mu \left[\frac{q_2}{q_1} \left(\frac{\partial u}{\partial y} + \frac{\partial v}{\partial x} \right) + \frac{q_3}{q_1} \left(\frac{4}{3} \frac{\partial v}{\partial y} - \frac{2}{3} \left(\frac{\partial u}{\partial x} + \frac{\partial w}{\partial z} \right) \right) + \frac{q_4}{q_1} \left(\frac{\partial v}{\partial z} + \frac{\partial w}{\partial y} \right) \right] + \kappa \frac{\partial T}{\partial y} \end{bmatrix} \tag{17}$$

$$\mathbf{f}_3^v = \frac{1}{Re_\infty} \begin{bmatrix} 0 \\ \mu \left(\frac{\partial u}{\partial z} + \frac{\partial w}{\partial x} \right) \\ \mu \left(\frac{\partial v}{\partial z} + \frac{\partial w}{\partial y} \right) \\ \mu \left(2 \frac{\partial w}{\partial z} - \frac{2}{3} \left(\frac{\partial u}{\partial x} + \frac{\partial v}{\partial y} + \frac{\partial w}{\partial z} \right) \right) \\ \mu \left[\frac{q_2}{q_1} \left(\frac{\partial u}{\partial z} + \frac{\partial w}{\partial x} \right) + \frac{q_3}{q_1} \left(\frac{\partial v}{\partial z} + \frac{\partial w}{\partial y} \right) + \frac{q_4}{q_1} \left(\frac{4}{3} \frac{\partial w}{\partial z} - \frac{2}{3} \left(\frac{\partial u}{\partial x} + \frac{\partial v}{\partial y} \right) \right) \right] + \kappa \frac{\partial T}{\partial z} \end{bmatrix}$$

B. Disturbance analysis - linearized NS-equations

The compressible Navier-Stokes equations are expressed in HORSES3D code in conservative form as:

$$\frac{\partial \mathbf{q}}{\partial t} + \vec{\nabla} \cdot \left(\vec{\mathbf{f}}(\mathbf{q})^a - \vec{\mathbf{f}}(\mathbf{q})^v \right) = \mathbf{s}, \tag{18}$$

where all fluxes are expressed in conservative variables, as shown in Eqs. (11) and (17).

For disturbance analysis, the base flow and its disturbance need to be separated in the equation. The relation between the base flow and its disturbance with the conservative variables $\mathbf{q}$ is as follows:

$$\mathbf{q}(\mathbf{x}, t) = \bar{\mathbf{q}}(\mathbf{x}) + \epsilon \mathbf{q}'(\mathbf{x}, t), \tag{19}$$

where $\overline{\mathbf{q}}$ is the steady solution for simplicity, $\mathbf{q}'$ is the fluctuation or disturbance, and ϵ represents the order of the term to signify small fluctuations. Using Eq. (19), the fluxes are then split into the base flow and its fluctuation contributions.

Some algebraic manipulations and Taylor expansions that will be useful are:

- $\frac{1}{q_i} \rightarrow$

$$\begin{aligned}
\frac{1}{q_i} &= \frac{1}{\bar{q}_i + \epsilon q_i'} = \frac{1}{\bar{q}_i \left(1 + \epsilon \frac{q_i'}{\bar{q}_i}\right)} = \frac{1}{\bar{q}_i} \frac{1}{\left(1 + \epsilon \frac{q_i'}{\bar{q}_i}\right)} \\
&= \frac{1}{\bar{q}_i} \left(1 - \epsilon \frac{q_i'}{\bar{q}_i} + \left(\epsilon \frac{q_i'}{\bar{q}_i} \right)^2 - \left(\epsilon \frac{q_i'}{\bar{q}_i} \right)^3 + ... \right) \\
&= \frac{1}{\bar{q}_i} + \frac{1}{\bar{q}_i} \left(-\epsilon \frac{q_i'}{\bar{q}_i} + \left(\epsilon \frac{q_i'}{\bar{q}_i} \right)^2 - \left(\epsilon \frac{q_i'}{\bar{q}_i} \right)^3 + ... \right). \\
&= \frac{1}{\bar{q}_i} + \left(\epsilon \frac{1}{q_i} \right)' \\
&\approx \frac{1}{\bar{q}_i} + \left(-\epsilon \frac{q_i'}{\bar{q}_i^2} \right) \qquad \textit{Linearized}
\end{aligned} \tag{20}$$

  For linearized equation, higher-order terms of ϵ are neglected.

$$\left(\epsilon \frac{1}{q_i} \right)' = \frac{1}{\bar{q}_i + \epsilon q_i'} - \frac{1}{\bar{q}_i} \tag{21}$$

- $\frac{q_j}{q_i} \rightarrow$

$$\begin{aligned}
\frac{q_j}{q_i} &= \left(\bar{q_j} + \epsilon q_j'\right)\left(\frac{1}{\bar{q_i} + \epsilon q_i'}\right) \\
&= \left(\bar{q_j} + \epsilon q_j'\right)\left[\frac{1}{\bar{q_i}}\left(1 - \epsilon\frac{q_i'}{\bar{q_i}} + \left(\epsilon\frac{q_i'}{\bar{q_i}}\right)^2 - \left(\epsilon\frac{q_i'}{\bar{q_i}}\right)^3 + ...\right)\right] \\
&= \frac{\bar{q_j}}{\bar{q_i}} + \epsilon\frac{q_j'}{\bar{q_i}} + \left(\bar{q_j} + \epsilon q_j'\right)\left[\frac{1}{\bar{q_i}}\left(-\epsilon\frac{q_i'}{\bar{q_i}} + \left(\epsilon\frac{q_i'}{\bar{q_i}}\right)^2 - \left(\epsilon\frac{q_i'}{\bar{q_i}}\right)^3 + ...\right)\right] \quad , \quad j \neq i \qquad (22) \\
&= \frac{\bar{q_j}}{\bar{q_i}} + \left(\epsilon\frac{q_j}{q_i}\right)' \\
&\approx \frac{\bar{q_j}}{\bar{q_i}} + \epsilon\frac{q_j'}{\bar{q_i}} - \epsilon\frac{q_i'\bar{q_j}}{\bar{q_i}^2} \qquad \textit{Linearized}
\end{aligned}$$

- $\frac{q_j q_k}{q_i} \rightarrow$

$$\begin{aligned}
\frac{q_j q_k}{q_i} &= (\bar{q_k} + \epsilon q_k')\left[\frac{\bar{q_j}}{\bar{q_i}} + \left(\epsilon\frac{q_j}{q_i}\right)'\right] \\
&= \frac{\bar{q_j}\bar{q_k}}{\bar{q_i}} + \frac{\epsilon\bar{q_j}q_k'}{\bar{q_i}} + \epsilon\bar{q_k}\left(\frac{q_j}{q_i}\right)' + \epsilon^2 q_k'\left(\frac{q_j}{q_i}\right)' \\
&= \frac{\bar{q_j}\bar{q_k}}{\bar{q_i}} + \left(\epsilon\frac{q_j q_k}{q_i}\right)' \qquad , \quad j,k \neq i \qquad (23) \\
&\approx \frac{\bar{q_j}\bar{q_k}}{\bar{q_i}} + \epsilon\frac{q_j'\bar{q_k}}{\bar{q_i}} - \epsilon\frac{q_i'\bar{q_j}\bar{q_k}}{\bar{q_i}^2} + \epsilon\frac{\bar{q_j}q_k'}{\bar{q_i}} \qquad \textit{Linearized}
\end{aligned}$$

- $\frac{q_j}{q_i^2} \rightarrow$

$$\begin{aligned}
\frac{q_j}{q_i^2} &= \left[\frac{\bar{q_j}}{\bar{q_i}} + \left(\epsilon\frac{q_j}{q_i}\right)'\right]\left[\frac{1}{\bar{q_i}} + \left(\epsilon\frac{1}{q_i}\right)'\right] \\
&= \frac{\bar{q_j}}{\bar{q_i}^2} + \epsilon\frac{1}{\bar{q_i}}\left(\frac{q_j}{q_i}\right)' + \epsilon\frac{\bar{q_j}}{\bar{q_i}}\left(\frac{1}{q_i}\right)' + \epsilon^2\left(\frac{q_j}{q_i}\right)'\left(\frac{1}{q_i}\right)' \\
&= \frac{\bar{q_j}}{\bar{q_i}^2} + \left(\epsilon\frac{q_j}{q_i^2}\right)' \qquad , \quad j \neq i \qquad (24) \\
&\approx \frac{\bar{q_j}}{\bar{q_i}^2} + \epsilon\frac{q_j'}{\bar{q_i}^2} - 2\epsilon\frac{q_i'\bar{q_j}}{\bar{q_i}^3} \qquad \textit{Linearized}
\end{aligned}$$

- $\frac{q_j^2}{q_i^2} \rightarrow$

$$\begin{aligned}
\frac{q_j^2}{q_i^2} &= \left(\frac{\bar{q}_j}{\bar{q}_i} + \left(\epsilon\frac{q_j}{q_i}\right)'\right)^2 \\
&= \frac{\bar{q}_j{}^2}{\bar{q}_i{}^2} + 2\epsilon\frac{\bar{q}_j}{\bar{q}_i}\left(\epsilon\frac{q_j}{q_i}\right)' + \epsilon^2\left(\left(\epsilon\frac{q_j}{q_i}\right)'\right)^2 \qquad , \quad j \neq i \\
&= \frac{\bar{q}_j{}^2}{\bar{q}_i{}^2} + \left(\epsilon\frac{q_j^2}{q_i^2}\right)' \\
&\approx \frac{\bar{q}_j{}^2}{\bar{q}_i{}^2} + 2\epsilon\frac{q_j'\bar{q}_j}{\bar{q}_i{}^2} - 2\epsilon\frac{q_i'\bar{q}_j{}^2}{\bar{q}_i{}^3} \qquad \textit{Linearized}
\end{aligned} \tag{25}$$

- $\frac{q_j^2 q_k}{q_i^2} \rightarrow$

$$\begin{aligned}
\frac{q_j^2 q_k}{q_i^2} &= (\bar{q}_k + \epsilon q_k')\left[\frac{\bar{q}_j{}^2}{\bar{q}_i^2} + \left(\epsilon\frac{q_j^2}{q_i^2}\right)'\right] \\
&= \frac{\bar{q}_j{}^2\bar{q}_k}{\bar{q}_i{}^2} + \epsilon\frac{\bar{q}_j{}^2}{\bar{q}_i{}^2}q_k' + \epsilon\bar{q}_k\left(\frac{q_j^2}{q_i^2}\right)' + \epsilon^2 q_k'\left(\frac{q_j^2}{q_i^2}\right)' \qquad , \quad j,k \neq i \\
&= \frac{\bar{q}_j{}^2\bar{q}_k}{\bar{q}_i{}^2} + \left(\epsilon\frac{q_j^2 q_k}{q_i^2}\right)' \\
&\approx \frac{\bar{q}_j{}^2\bar{q}_k}{\bar{q}_i{}^2} + 2\epsilon\frac{q_j'\bar{q}_j\bar{q}_k}{\bar{q}_i{}^2} - 2\epsilon\frac{q_i'\bar{q}_j{}^2\bar{q}_k}{\bar{q}_i{}^3} + \epsilon\frac{\bar{q}_j{}^2 q_k'}{\bar{q}_i{}^2} \qquad \textit{Linearized}
\end{aligned} \tag{26}$$

- $\frac{q_j^2}{q_i^3} \rightarrow$

$$\begin{aligned}
\frac{q_j^2}{q_i^3} &= \left[\frac{\bar{q}_j{}^2}{\bar{q}_i{}^2} + \left(\epsilon\frac{q_j^2}{q_i^2}\right)'\right]\left[\frac{1}{\bar{q}_i} + \left(\epsilon\frac{1}{q_i}\right)'\right] \\
&= \frac{\bar{q}_j{}^2}{\bar{q}_i{}^3} + \epsilon\frac{1}{\bar{q}_i}\left(\frac{q_j^2}{q_i^2}\right)' + \epsilon\frac{\bar{q}_j{}^2}{\bar{q}_i{}^2}\left(\frac{1}{q_i}\right)' + \epsilon^2\left(\frac{q_j^2}{q_i^2}\right)'\left(\frac{1}{q_i}\right)' \qquad , \quad j \neq i \\
&= \frac{\bar{q}_j{}^2}{\bar{q}_i{}^3} + \left(\epsilon\frac{q_j^2}{q_i^3}\right)' \\
&\approx \frac{\bar{q}_j{}^2}{\bar{q}_i{}^3} + 2\epsilon\frac{q_j'\bar{q}_j}{\bar{q}_i{}^3} - 3\epsilon\frac{q_i'\bar{q}_j{}^2}{\bar{q}_i{}^4} \qquad \textit{Linearized}
\end{aligned} \tag{27}$$

- $\frac{\partial q_i}{\partial n} \rightarrow$

$$\begin{aligned}
\frac{\partial q_i}{\partial n} &= \frac{\partial\left(\bar{q}_i + q_i'\right)}{\partial n} \qquad , \quad n = x, y, z \\
&= \frac{\partial\bar{q}_i}{\partial n} + \frac{\partial q_i'}{\partial n}
\end{aligned} \tag{28}$$

- $\frac{\partial \frac{q_j}{q_i}}{\partial n} \rightarrow$

$$
\begin{aligned}
\frac{\partial\left(\frac{q_j}{q_i}\right)}{\partial n} &= \frac{1}{q_i}\frac{\partial q_j}{\partial n} - \frac{q_j}{q_i^2}\frac{\partial q_i}{\partial n} \\
&= \left(\frac{1}{\bar{q}_i} + \epsilon\left(\frac{1}{q_i}\right)'\right)\left(\frac{\partial \bar{q}_j}{\partial n} + \epsilon\frac{\partial q_j'}{\partial n}\right) - \left(\frac{\bar{q}_j}{\bar{q}_i{}^2} + \epsilon\left(\frac{q_j}{q_i^2}\right)'\right)\left(\frac{\partial \bar{q}_i}{\partial n} + \epsilon\frac{\partial q_i'}{\partial n}\right) \\
&= \left[\frac{1}{\bar{q}_i}\frac{\partial \bar{q}_j}{\partial n} - \frac{\bar{q}_j}{\bar{q}_i{}^2}\frac{\partial \bar{q}_i}{\partial n}\right] + \left[\epsilon\left(\frac{1}{q_i}\right)'\frac{\partial \bar{q}_j}{\partial n} + \left(\frac{1}{\bar{q}_i} + \epsilon\left(\frac{1}{q_i}\right)'\right)\epsilon\frac{\partial q_j'}{\partial n}\right. \\
&\qquad \left. - \epsilon\left(\frac{q_j}{q_i^2}\right)'\frac{\partial \bar{q}_i}{\partial n} - \left(\frac{\bar{q}_j}{\bar{q}_i{}^2} + \epsilon\left(\frac{q_j}{q_i^2}\right)'\right)\epsilon\frac{\partial q_i'}{\partial n}\right] \qquad , \quad n = x, y, z \\
&= \partial_n\left(\frac{\bar{q}_j}{\bar{q}_i}\right) + \epsilon\left(\partial_n\left(\frac{q_j}{q_i}\right)\right)' \\
&\approx \partial_n\left(\frac{\bar{q}_j}{\bar{q}_i}\right) - \epsilon\frac{q_i'}{\bar{q}_i{}^2}\frac{\partial \bar{q}_j}{\partial n} + \epsilon\frac{1}{\bar{q}_i}\frac{\partial q_j'}{\partial n} - \left(\epsilon\frac{q_j'}{\bar{q}_i{}^2} - 2\epsilon\frac{q_i'\bar{q}_j}{\bar{q}_i{}^3}\right)\frac{\partial \bar{q}_i}{\partial n} - \epsilon\frac{\bar{q}_j}{\bar{q}_i{}^2}\frac{\partial q_i'}{\partial n}
\end{aligned}
\tag{29}
$$

The above definitions simplify the notation for the disturbance equations by separating the contributions of the steady and fluctuating values.

B.1. Advection flux

Using the operation and notation described above, the advection/Euler flux can be expressed as:

$$\mathbf{f}_1^a = \begin{bmatrix} \bar{q_2} + \epsilon q_2' \\ \left(\frac{\bar{q_2}^2}{\bar{q_1}} + \left(\epsilon\frac{q_2^2}{q_1}\right)'\right) + (\gamma-1)\left[\bar{q_5} + \epsilon q_5' - \frac{1}{2}\left(\frac{\bar{q_2}^2}{\bar{q_1}} + \left(\epsilon\frac{q_2^2}{q_1}\right)' + \frac{\bar{q_3}^2}{\bar{q_1}} + \left(\epsilon\frac{q_3^2}{q_1}\right)' + \frac{\bar{q_4}^2}{\bar{q_1}} + \left(\epsilon\frac{q_4^2}{q_1}\right)'\right)\right] \\ \frac{\bar{q_2}\bar{q_3}}{\bar{q_1}} + \left(\epsilon\frac{q_2 q_3}{q_1}\right)' \\ \frac{\bar{q_2}\bar{q_4}}{\bar{q_1}} + \left(\epsilon\frac{q_2 q_4}{q_1}\right)' \\ \gamma\left(\frac{\bar{q_2}\bar{q_5}}{\bar{q_1}} + \left(\epsilon\frac{q_2 q_5}{q_1}\right)'\right) - \frac{(\gamma-1)}{2}\left(\frac{\bar{q_2}^3}{\bar{q_1}^2} + \left(\epsilon\frac{q_2^3}{q_1^2}\right)' + \frac{\bar{q_2}\bar{q_3}^2}{\bar{q_1}^2} + \left(\epsilon\frac{q_2 q_3^2}{q_1^2}\right)' + \frac{\bar{q_2}\bar{q_4}^2}{\bar{q_1}^2} + \left(\epsilon\frac{q_2 q_4^2}{q_1^2}\right)'\right) \end{bmatrix}$$

$$= \begin{bmatrix} \bar{q_2} \\ \frac{\bar{q_2}^2}{\bar{q_1}} + (\gamma-1)\left[\bar{q_5} + \frac{1}{2}\left(\frac{\bar{q_2}^2}{\bar{q_1}} + \frac{\bar{q_3}^2}{\bar{q_1}} + \frac{\bar{q_4}^2}{\bar{q_1}}\right)\right] \\ \frac{\bar{q_2}\bar{q_3}}{\bar{q_1}} \\ \frac{\bar{q_2}\bar{q_4}}{\bar{q_1}} \\ \frac{\bar{q_2}}{\bar{q_1}}\left[\gamma\ \bar{q_5} - \frac{(\gamma-1)}{2}\left(\frac{\bar{q_2}^2}{\bar{q_1}} + \frac{\bar{q_3}^2}{\bar{q_1}} + \frac{\bar{q_4}^2}{\bar{q_1}}\right)\right] \end{bmatrix} + \begin{bmatrix} \epsilon q_2' \\ \left(\epsilon\frac{q_2^2}{q_1}\right)' + (\gamma-1)\left[\epsilon q_5' - \frac{1}{2}\left(\left(\epsilon\frac{q_2^2}{q_1}\right)' + \left(\epsilon\frac{q_3^2}{q_1}\right)' + \left(\epsilon\frac{q_4^2}{q_1}\right)'\right)\right] \\ \left(\epsilon\frac{q_2 q_3}{q_1}\right)' \\ \left(\epsilon\frac{q_2 q_4}{q_1}\right)' \\ \gamma\left(\epsilon\frac{q_2 q_5}{q_1}\right)' - \frac{(\gamma-1)}{2}\left(\left(\epsilon\frac{q_2^3}{q_1^2}\right)' + \left(\epsilon\frac{q_2 q_3^2}{q_1^2}\right)' + \left(\epsilon\frac{q_2 q_4^2}{q_1^2}\right)'\right) \end{bmatrix} \tag{30}$$

The advection/Euler flux can be expressed more concisely as:

$$\mathbf{f}_1^a = \bar{\mathbf{f}}_1^a + \epsilon \mathbf{f'}_1^a \tag{31}$$

Using a similar process, $\mathbf{f}_2^a$ and $\mathbf{f}_3^a$ can also be expressed as:

$$\mathbf{f}_2^a = \bar{\mathbf{f}}_2^a + \epsilon \mathbf{f'}_2^a \tag{32}$$

$$\mathbf{f}_3^a = \bar{\mathbf{f}}_3^a + \epsilon \mathbf{f'}_3^a \tag{33}$$

Hence, the advection flux is given by:

$$\vec{\nabla} \cdot \vec{\mathbf{f}}(\mathbf{q})^a = \vec{\bar{\nabla}} \cdot \vec{\bar{\mathbf{f}}}(\mathbf{q})^{\mathbf{a}} + \tilde{\nabla} \cdot \epsilon \tilde{\mathbf{f}'}(\mathbf{q})^{\mathbf{a}} \tag{34}$$

$$\mathbf{f}_2^a = \begin{bmatrix} \bar{q_3} \\ \frac{\bar{q_2}\bar{q_3}}{\bar{q_1}} \\ \frac{\bar{q_3}^2}{\bar{q_1}} + (\gamma-1)\left[\bar{q_5} + \frac{1}{2}\left(\frac{\bar{q_2}^2}{\bar{q_1}} + \frac{\bar{q_3}^2}{\bar{q_1}} + \frac{\bar{q_4}^2}{\bar{q_1}}\right)\right] \\ \frac{\bar{q_3}\bar{q_4}}{\bar{q_1}} \\ \frac{\bar{q_3}}{\bar{q_1}}\left[\gamma\ \bar{q_5} - \frac{(\gamma-1)}{2}\left(\frac{\bar{q_2}^2}{\bar{q_1}} + \frac{\bar{q_3}^2}{\bar{q_1}} + \frac{\bar{q_4}^2}{\bar{q_1}}\right)\right] \end{bmatrix} + \begin{bmatrix} \epsilon q_3' \\ \left(\epsilon\frac{q_2 q_3}{q_1}\right)' \\ \left(\epsilon\frac{q_3^2}{q_1}\right)' + (\gamma-1)\left[\epsilon q_5' - \frac{1}{2}\left(\left(\epsilon\frac{q_2^2}{q_1}\right)' + \left(\epsilon\frac{q_3^2}{q_1}\right)' + \left(\epsilon\frac{q_4^2}{q_1}\right)'\right)\right] \\ \left(\epsilon\frac{q_3 q_4}{q_1}\right)' \\ \gamma\left(\epsilon\frac{q_3 q_5}{q_1}\right)' - \frac{(\gamma-1)}{2}\left(\left(\epsilon\frac{q_2^3}{q_1^2}\right)' + \left(\epsilon\frac{q_2 q_3^2}{q_1^2}\right)' + \left(\epsilon\frac{q_2 q_4^2}{q_1^2}\right)'\right) \end{bmatrix} \tag{35}$$

$$\mathbf{f}_3^a = \begin{bmatrix} \bar{q_4} \\ \frac{\bar{q_2}\bar{q_4}}{\bar{q_1}} \\ \frac{\bar{q_3}\bar{q_4}}{\bar{q_1}} \\ \frac{\bar{q_4}^2}{\bar{q_1}} + (\gamma-1)\left[\bar{q_5} + \frac{1}{2}\left(\frac{\bar{q_2}^2}{\bar{q_1}} + \frac{\bar{q_3}^2}{\bar{q_1}} + \frac{\bar{q_4}^2}{\bar{q_1}}\right)\right] \\ \frac{\bar{q_4}}{\bar{q_1}}\left[\gamma\ \bar{q_5} - \frac{(\gamma-1)}{2}\left(\frac{\bar{q_2}^2}{\bar{q_1}} + \frac{\bar{q_3}^2}{\bar{q_1}} + \frac{\bar{q_4}^2}{\bar{q_1}}\right)\right] \end{bmatrix} + \begin{bmatrix} \epsilon q_4' \\ \left(\epsilon\frac{q_2 q_4}{q_1}\right)' \\ \left(\epsilon\frac{q_3 q_4}{q_1}\right)' \\ \left(\epsilon\frac{q_4^2}{q_1}\right)' + (\gamma-1)\left[\epsilon q_5' - \frac{1}{2}\left(\left(\epsilon\frac{q_2^2}{q_1}\right)' + \left(\epsilon\frac{q_3^2}{q_1}\right)' + \left(\epsilon\frac{q_4^2}{q_1}\right)'\right)\right] \\ \gamma\left(\epsilon\frac{q_4 q_5}{q_1}\right)' - \frac{(\gamma-1)}{2}\left(\left(\epsilon\frac{q_2^3}{q_1^2}\right)' + \left(\epsilon\frac{q_2 q_3^2}{q_1^2}\right)' + \left(\epsilon\frac{q_2 q_4^2}{q_1^2}\right)'\right) \end{bmatrix} \tag{36}$$

B.2. Viscous flux

Some external expressions are needed to be defined in order to separate viscosity, μ, into its steady and fluctuation contribution. The equation for temperature can be divided as

$$\begin{aligned} T &= (\gamma^2-\gamma)M_{ref}^2\left[\frac{q_5}{q_1}-\frac{1}{2}\left(\frac{q_2^2}{q_1^2}+\frac{q_3^2}{q_1^2}+\frac{q_4^2}{q_1^2}\right)\right] \\ &= (\gamma^2-\gamma)M_{ref}^2\left[\frac{\bar{q_5}}{\bar{q_1}}-\frac{1}{2}\left(\frac{\bar{q_2}^2}{\bar{q_1}^2}+\frac{\bar{q_3}^2}{\bar{q_1}^2}+\frac{\bar{q_4}^2}{\bar{q_1}^2}\right)\right] \\ &\qquad + (\gamma^2-\gamma)M_{ref}^2\left[\left(\frac{q_5}{q_1}\right)'-\frac{1}{2}\left(\left(\frac{q_2^2}{q_1^2}\right)'+\left(\frac{q_3^2}{q_1^2}\right)'+\left(\frac{q_4^2}{q_1^2}\right)'\right)\right] \\ &= \bar{T}+\epsilon T' \end{aligned} \tag{37}$$

With above expression the viscosity can be written as

$$\mu = \frac{1+T_{suth}/T_\infty}{\left(\bar{T}+\epsilon T'\right)+T_{suth}/T_\infty}\left(\bar{T}+\epsilon T'\right)^{\frac{3}{2}} \tag{38}$$

The term $\left(\bar{T}+\epsilon T'\right)^{\frac{3}{2}}$ can be divided into the steady and fluctuation such as $\left(\bar{T}+\epsilon T'\right)^{\frac{3}{2}} = \bar{T}^{\frac{3}{2}}+\left(\epsilon\left(\bar{T}+T'\right)^{\frac{3}{2}}\right)'$. For Linearized equation, it can be approximated with steady and linear relation such as $\left(\bar{T}+\epsilon T'\right)^{\frac{3}{2}} \approx \bar{T}^{\frac{3}{2}}+\epsilon\frac{3}{2}T'\bar{T}^{\frac{1}{2}}$. Hence, equation (2.21) can be modified into

$$\begin{aligned} \mu &= \left(\frac{1+T_{suth}/T_\infty}{\bar{T}+T_{suth}/T_\infty}\right)\left[\frac{1}{1+\epsilon\frac{T'}{\bar{T}+T_{suth}/T_\infty}}\right]\left(\bar{T}+\epsilon T'\right)^{\frac{3}{2}} \\ &= \left(\frac{1+T_{suth}/T_\infty}{\bar{T}+T_{suth}/T_\infty}\right)\left[1-\epsilon\frac{T'}{\bar{T}+T_{suth}/T_\infty}+\left(\epsilon\frac{T'}{\bar{T}+T_{suth}/T_\infty}\right)^2-...\right]\left(\bar{T}+\epsilon T'\right)^{\frac{3}{2}} \\ &= \bar{\mu}+\epsilon\mu' \\ &\approx \left(\frac{1+T_{suth}/T_\infty}{\bar{T}+T_{suth}/T_\infty}\right)\bar{T}^{\frac{3}{2}}+\left(\frac{1+T_{suth}/T_\infty}{\bar{T}+T_{suth}/T_\infty}\right)\left(\epsilon\frac{3}{2}T'\bar{T}^{\frac{1}{2}}-\epsilon\frac{T'\bar{T}^{\frac{3}{2}}}{\bar{T}+T_{suth}/T_\infty}\right) \end{aligned} \tag{39}$$

Equation (2.22) is approximate it as Linearized equation. The fluctuation value for non-Linearized equation can be obtained with similar idea of equation (2.4), $\epsilon\mu' = \mu(\bar{T}+\epsilon T')-\mu(\bar{T})$. The non-dimensional thermal conductivity can be expressed as

$$\begin{aligned} \kappa &= \frac{\bar{\mu}}{(\gamma-1)\,Pr\;M_{ref}}+\epsilon\frac{\mu'}{(\gamma-1)\,Pr\;M_{ref}} \\ &= \bar{\kappa}+\epsilon\kappa' \end{aligned} \tag{40}$$

The gradient of temperature in x-direction can be expressed as

$$\begin{aligned}\frac{\partial T}{\partial x} = (\gamma^2-\gamma)M_{ref}^2\Bigg[&\left(\frac{1}{\bar{q_1}}+\epsilon\left(\frac{1}{q_1}\right)'\right)\left(\frac{\partial \bar{q_5}}{\partial x}+\epsilon\frac{\partial q_5'}{\partial x}\right)-\left(\frac{\bar{q_4}}{\bar{q_1^2}}+\epsilon\left(\frac{q_4}{{q_1}^2}\right)'\right)\left(\frac{\partial \bar{q_4}}{\partial x}+\epsilon\frac{\partial q_4'}{\partial x}\right)\\ &-\left(\frac{\bar{q_3}}{\bar{q_1^2}}+\epsilon\left(\frac{q_3}{{q_1}^2}\right)'\right)\left(\frac{\partial \bar{q_3}}{\partial x}+\epsilon\frac{\partial q_3'}{\partial x}\right)-\left(\frac{\bar{q_2}}{\bar{q_1^2}}+\epsilon\left(\frac{q_2}{{q_1}^2}\right)'\right)\left(\frac{\partial \bar{q_2}}{\partial x}+\epsilon\frac{\partial q_2'}{\partial x}\right)\\ &+\Bigg[\frac{\bar{q_2}^2}{\bar{q_1}^3}+\epsilon\left(\frac{q_2^2}{q_1^3}\right)'+\frac{\bar{q_3}^2}{\bar{q_1}^3}+\epsilon\left(\frac{q_3^2}{q_1^3}\right)'+\frac{\bar{q_4}^2}{\bar{q_1}^3}+\epsilon\left(\frac{q_4^2}{q_1^3}\right)'\\ &-\frac{\bar{q_5}}{\bar{q_1}^2}-\epsilon\left(\frac{q_5}{q_1^2}\right)'\Bigg]\left(\frac{\partial \bar{q_1}}{\partial x}+\epsilon\frac{\partial q_1'}{\partial x}\right)\Bigg]\end{aligned} \tag{41}$$

The steady and fluctuation components are then separated into:

$$\begin{aligned}\frac{\partial T}{\partial x} = (\gamma^2-\gamma)M_{ref}^2&\left[\left(\frac{1}{\bar{q_1}}\frac{\partial \bar{q_5}}{\partial x}-\frac{\bar{q_4}}{\bar{q_1}^2}\frac{\partial \bar{q_4}}{\partial x}-\frac{\bar{q_3}}{\bar{q_1}^2}\frac{\partial \bar{q_3}}{\partial x}-\frac{\bar{q_2}}{\bar{q_1}^2}\frac{\partial \bar{q_2}}{\partial x}\right)+\left(\frac{\bar{q_2}^2}{\bar{q_1}^3}+\frac{\bar{q_3}^2}{\bar{q_1}^3}+\frac{\bar{q_4}^2}{\bar{q_1}^3}-\frac{\bar{q_5}}{\bar{q_1}^2}\right)\frac{\partial \bar{q_1}}{\partial x}\right]\\ &+(\gamma^2-\gamma)M_{ref}^2\Bigg[\epsilon\left(\frac{1}{q_1}\right)'\frac{\partial \bar{q_5}}{\partial x}+\epsilon\left(\frac{1}{\bar{q_1}}+\epsilon\left(\frac{1}{q_1}\right)'\right)\frac{\partial q_5'}{\partial x}-\epsilon\left(\frac{q_4}{{q_1}^2}\right)'\frac{\partial \bar{q_4}}{\partial x}\\ &-\epsilon\left(\frac{\bar{q_4}}{\bar{q_1^2}}+\epsilon\left(\frac{q_4}{{q_1}^2}\right)'\right)\frac{\partial q_4'}{\partial x}-\epsilon\left(\frac{q_3}{{q_1}^2}\right)'\frac{\partial \bar{q_3}}{\partial x}-\epsilon\left(\frac{\bar{q_3}}{\bar{q_1^2}}+\epsilon\left(\frac{q_3}{{q_1}^2}\right)'\right)\frac{\partial q_3'}{\partial x}\\ &-\epsilon\left(\frac{q_2}{{q_1}^2}\right)'\frac{\partial \bar{q_2}}{\partial x}-\epsilon\left(\frac{\bar{q_2}}{\bar{q_1^2}}+\epsilon\left(\frac{q_2}{{q_1}^2}\right)'\right)\frac{\partial q_2'}{\partial x}+\epsilon\left(\frac{q_2^2}{q_1^3}\right)'\frac{\partial \bar{q_1}}{\partial x}+\epsilon\left(\frac{q_3^2}{q_1^3}\right)'\frac{\partial \bar{q_1}}{\partial x}\\ &+\epsilon\left(\frac{q_4^2}{q_1^3}\right)'\frac{\partial \bar{q_1}}{\partial x}-\epsilon\left(\frac{q_5}{q_1^2}\right)'\frac{\partial \bar{q_1}}{\partial x}+\Bigg[\frac{\bar{q_2}^2}{\bar{q_1}^3}+\epsilon\left(\frac{q_2^2}{q_1^3}\right)'+\frac{\bar{q_3}^2}{\bar{q_1}^3}+\epsilon\left(\frac{q_3^2}{q_1^3}\right)'+\frac{\bar{q_4}^2}{\bar{q_1}^3}\\ &+\epsilon\left(\frac{q_4^2}{q_1^3}\right)'-\frac{\bar{q_5}}{\bar{q_1}^2}-\epsilon\left(\frac{q_5}{q_1^2}\right)'\Bigg]\epsilon\frac{\partial q_1'}{\partial x}\Bigg]\end{aligned}$$

$$\frac{\partial T}{\partial x} = \frac{\partial \bar{T}}{\partial x}+\epsilon\left(\frac{\partial T}{\partial x}\right)' \tag{42}$$

With above equations, the viscous flux components can be written by separating the steady and fluctuation variables. The viscous flux components written below omit the $\frac{1}{Re_\infty}$ term for

simplification. Defining the stress tensor component without viscosity such as,

$$\begin{aligned}
\tau_{xx} &= 2\ \partial_x\left(\frac{q_2}{q_1}\right) - \frac{2}{3}\left[\partial_x\left(\frac{q_2}{q_1}\right) + \partial_y\left(\frac{q_3}{q_1}\right) + \partial_z\left(\frac{q_4}{q_1}\right)\right] \\
&= \bar{\tau}_{xx} + \epsilon\tau'_{xx} \\
\tau_{yy} &= 2\ \partial_y\left(\frac{q_3}{q_1}\right) - \frac{2}{3}\left[\partial_x\left(\frac{q_2}{q_1}\right) + \partial_y\left(\frac{q_3}{q_1}\right) + \partial_z\left(\frac{q_4}{q_1}\right)\right] \\
&= \bar{\tau}_{yy} + \epsilon\tau'_{yy} \\
\tau_{zz} &= 2\ \partial_z\left(\frac{q_4}{q_1}\right) - \frac{2}{3}\left[\partial_x\left(\frac{q_2}{q_1}\right) + \partial_y\left(\frac{q_3}{q_1}\right) + \partial_z\left(\frac{q_4}{q_1}\right)\right] \\
&= \bar{\tau}_{zz} + \epsilon\tau'_{zz}
\end{aligned} \tag{43}$$

$$\begin{aligned}
\tau_{xy} = \tau_{yx} &= \partial_y\left(\frac{q_2}{q_1}\right) + \partial_x\left(\frac{q_3}{q_1}\right) \\
&= \bar{\tau}_{xy} + \epsilon\tau'_{xy} \\
\tau_{xz} = \tau_{zx} &= \partial_z\left(\frac{q_2}{q_1}\right) + \partial_x\left(\frac{q_4}{q_1}\right) \\
&= \bar{\tau}_{xz} + \epsilon\tau'_{xz} \\
\tau_{yz} = \tau_{yz} &= \partial_z\left(\frac{q_3}{q_1}\right) + \partial_y\left(\frac{q_4}{q_1}\right) \\
&= \bar{\tau}_{yz} + \epsilon\tau'_{yz}
\end{aligned} \tag{44}$$

- x-direction

$$f^v_{11} = 0 \tag{45}$$

$$\begin{aligned}
f^v_{12} &\approx (\bar{\mu} + \epsilon\mu')\left[\frac{4}{3}\partial_x\left(\frac{\bar{q_2}}{\bar{q_1}}\right) + \frac{4}{3}\epsilon\left(\partial_x\left(\frac{q_2}{q_1}\right)\right)' - \frac{2}{3}\left[\partial_y\left(\frac{\bar{q_3}}{\bar{q_1}}\right) + \epsilon\left(\partial_y\left(\frac{q_3}{q_1}\right)\right)'\right.\right. \\
&\qquad \left.\left. + \partial_z\left(\frac{\bar{q_4}}{\bar{q_1}}\right) + \epsilon\left(\partial_z\left(\frac{q_4}{q_1}\right)\right)'\right]\right] \\
&\approx \bar{\mu}\left[\frac{4}{3}\partial_x\left(\frac{\bar{q_2}}{\bar{q_1}}\right) - \frac{2}{3}\left[\partial_y\left(\frac{\bar{q_3}}{\bar{q_1}}\right) + \partial_z\left(\frac{\bar{q_4}}{\bar{q_1}}\right)\right]\right] + \epsilon\bar{\mu}\left[\frac{4}{3}\left(\partial_x\left(\frac{q_2}{q_1}\right)\right)'\right. \\
&\qquad \left. - \frac{2}{3}\left[\left(\partial_y\left(\frac{q_3}{q_1}\right)\right)' + \left(\partial_z\left(\frac{q_4}{q_1}\right)\right)'\right]\right] + \epsilon\mu'\left[\frac{4}{3}\partial_x\left(\frac{\bar{q_2}}{\bar{q_1}}\right) + \frac{4}{3}\epsilon\left(\partial_x\left(\frac{q_2}{q_1}\right)\right)'\right. \\
&\qquad \left. - \frac{2}{3}\left[\partial_y\left(\frac{\bar{q_3}}{\bar{q_1}}\right) + \epsilon\left(\partial_y\left(\frac{q_3}{q_1}\right)\right)' + \partial_z\left(\frac{\bar{q_4}}{\bar{q_1}}\right) + \epsilon\left(\partial_z\left(\frac{q_4}{q_1}\right)\right)'\right]\right] \\
&\approx \bar{f^v_{12}} + \epsilon f'^v_{12}
\end{aligned} \tag{46}$$

$$
\begin{aligned}
f_{13}^{v} &\approx (\bar{\mu}+\epsilon\mu')\left[\partial_y\left(\frac{\bar{q}_2}{\bar{q}_1}\right)+\epsilon\left(\partial_y\left(\frac{q_2}{q_1}\right)\right)'+\partial_x\left(\frac{\bar{q}_3}{\bar{q}_1}\right)+\epsilon\left(\partial_x\left(\frac{q_3}{q_1}\right)\right)'\right] \\
&\approx \bar{\mu}\left[\partial_y\left(\frac{\bar{q}_2}{\bar{q}_1}\right)+\partial_x\left(\frac{\bar{q}_3}{\bar{q}_1}\right)\right]+\epsilon\bar{\mu}\left[\left(\partial_y\left(\frac{q_2}{q_1}\right)\right)'+\left(\partial_x\left(\frac{q_3}{q_1}\right)\right)'\right] \\
&\qquad +\epsilon\mu'\left[\partial_y\left(\frac{\bar{q}_2}{\bar{q}_1}\right)+\epsilon\left(\partial_y\left(\frac{q_2}{q_1}\right)\right)'+\partial_x\left(\frac{\bar{q}_3}{\bar{q}_1}\right)+\epsilon\left(\partial_x\left(\frac{q_3}{q_1}\right)\right)'\right] \\
&\approx \bar{f}_{13}^{v}+\epsilon f_{13}^{\prime v}
\end{aligned} \tag{47}
$$

$$
\begin{aligned}
f_{14}^{v} &\approx (\bar{\mu}+\epsilon\mu')\left[\partial_z\left(\frac{\bar{q}_2}{\bar{q}_1}\right)+\epsilon\left(\partial_z\left(\frac{q_2}{q_1}\right)\right)'+\partial_x\left(\frac{\bar{q}_4}{\bar{q}_1}\right)+\epsilon\left(\partial_x\left(\frac{q_4}{q_1}\right)\right)'\right] \\
&\approx \bar{\mu}\left[\partial_z\left(\frac{\bar{q}_2}{\bar{q}_1}\right)+\partial_x\left(\frac{\bar{q}_4}{\bar{q}_1}\right)\right]+\epsilon\bar{\mu}\left[\left(\partial_z\left(\frac{q_2}{q_1}\right)\right)'+\left(\partial_x\left(\frac{q_4}{q_1}\right)\right)'\right] \\
&\qquad +\epsilon\mu'\left[\partial_z\left(\frac{\bar{q}_2}{\bar{q}_1}\right)+\epsilon\left(\partial_z\left(\frac{q_2}{q_1}\right)\right)'+\partial_x\left(\frac{\bar{q}_4}{\bar{q}_1}\right)+\epsilon\left(\partial_x\left(\frac{q_4}{q_1}\right)\right)'\right] \\
&\approx \bar{f}_{14}^{v}+\epsilon f_{14}^{\prime v}
\end{aligned} \tag{48}
$$

$$
\begin{aligned}
f_{15}^{v} &\approx (\bar{\mu}+\epsilon\mu')\left[\left(\frac{\bar{q}_2}{\bar{q}_1}+\epsilon\left(\frac{q_2}{q_1}\right)'\right)(\bar{\tau}_{xx}+\epsilon\tau'_{xx})+\left(\frac{\bar{q}_3}{\bar{q}_1}+\epsilon\left(\frac{q_3}{q_1}\right)'\right)\left(\bar{\tau}_{xy}+\epsilon\tau'_{xy}\right)\right. \\
&\qquad \left.+\left(\frac{\bar{q}_4}{\bar{q}_1}+\epsilon\left(\frac{q_4}{q_1}\right)'\right)(\bar{\tau}_{xz}+\epsilon\tau'_{xz})\right]+(\bar{\kappa}+\epsilon\kappa')\left[\frac{\partial\bar{T}}{\partial x}+\epsilon\left(\frac{\partial T}{\partial x}\right)'\right] \\
&\approx \left[\bar{\mu}\left(\frac{\bar{q}_2}{\bar{q}_1}\bar{\tau}_{xx}+\frac{\bar{q}_3}{\bar{q}_1}\bar{\tau}_{xy}+\frac{\bar{q}_4}{\bar{q}_1}\bar{\tau}_{xz}\right)+\bar{\kappa}\frac{\partial\bar{T}}{\partial x}\right]+\epsilon\left[(\bar{\mu}+\epsilon\mu')\left[\left(\frac{q_2}{q_1}\right)'\bar{\tau}_{xx}\right.\right. \\
&\qquad +\left(\frac{\bar{q}_2}{\bar{q}_1}+\epsilon\left(\frac{q_2}{q_1}\right)'\right)\tau'_{xx}+\left(\frac{q_3}{q_1}\right)'\bar{\tau}_{xy}+\left(\frac{\bar{q}_3}{\bar{q}_1}+\epsilon\left(\frac{q_3}{q_1}\right)'\right)\tau'_{xy} \\
&\qquad \left.+\left(\frac{q_4}{q_1}\right)'\bar{\tau}_{xz}+\left(\frac{\bar{q}_4}{\bar{q}_1}+\epsilon\left(\frac{q_4}{q_1}\right)'\right)\tau'_{xz}\right] \\
&\qquad +\mu'\left[\left(\frac{\bar{q}_2}{\bar{q}_1}+\epsilon\left(\frac{q_2}{q_1}\right)'\right)(\bar{\tau}_{xx}+\epsilon\tau'_{xx})+\left(\frac{\bar{q}_3}{\bar{q}_1}+\epsilon\left(\frac{q_3}{q_1}\right)'\right)\left(\bar{\tau}_{xy}+\epsilon\tau'_{xy}\right)\right. \\
&\qquad \left.\left.+\left(\frac{\bar{q}_4}{\bar{q}_1}+\epsilon\left(\frac{q_4}{q_1}\right)'\right)(\bar{\tau}_{xz}+\epsilon\tau'_{xz})\right]+\bar{\kappa}\left(\frac{\partial T}{\partial x}\right)'+\kappa'\left(\frac{\partial\bar{T}}{\partial x}+\epsilon\left(\frac{\partial T}{\partial x}\right)'\right)\right] \\
&\approx \bar{f}_{15}^{v}+\epsilon f_{15}^{\prime v}
\end{aligned} \tag{49}
$$

Similar with advection flux, it can be expressed in shorter notation as

$$\mathbf{f}_1^v \approx \bar{\mathbf{f}}_1^v + \epsilon \mathbf{f}'^v_1 \tag{50}$$

With similar process $\mathbf{f}_2^v$ and $\mathbf{f}_3^v$ also can be expressed as

$$\mathbf{f}_2^v \approx \bar{\mathbf{f}}_2^v + \epsilon \mathbf{f}'^v_2 \tag{51}$$

$$\mathbf{f}_3^v \approx \bar{\mathbf{f}}_3^v + \epsilon \mathbf{f'}_3^v \tag{52}$$

Hence, the viscous flux in equation (2.1) can be expressed as

$$\vec{\nabla} \cdot \vec{\mathbf{f}}(\mathbf{q})^v = \vec{\nabla} \cdot \bar{\vec{\mathbf{f}}}(\mathbf{q})^{\mathbf{v}} + \tilde{\nabla} \cdot \epsilon \tilde{\mathbf{f}'}(\mathbf{q})^{\mathbf{v}} \tag{53}$$

- y-direction

$$f_{21}^v = 0 \tag{54}$$

$$\begin{aligned} f_{22}^v &= f_{13}^v \\ &\approx \bar{f_{13}^v} + \epsilon f_{13}'^v \\ &\approx \bar{f_{23}^v} + \epsilon f_{23}'^v \end{aligned} \tag{55}$$

$$\begin{aligned} f_{23}^v \approx (\bar{\mu} + \epsilon\mu') &\left[\frac{4}{3}\partial_y\left(\frac{\bar{q_3}}{\bar{q_1}}\right) + \frac{4}{3}\epsilon\left(\partial_y\left(\frac{q_3}{q_1}\right)\right)' - \frac{2}{3}\left[\partial_x\left(\frac{\bar{q_2}}{\bar{q_1}}\right) + \epsilon\left(\partial_x\left(\frac{q_2}{q_1}\right)\right)'\right.\right. \\ &\left.\left. + \partial_z\left(\frac{\bar{q_4}}{\bar{q_1}}\right) + \epsilon\left(\partial_z\left(\frac{q_4}{q_1}\right)\right)'\right]\right] \\ \approx \bar{\mu}&\left[\frac{4}{3}\partial_y\left(\frac{\bar{q_3}}{\bar{q_1}}\right) - \frac{2}{3}\left[\partial_x\left(\frac{\bar{q_2}}{\bar{q_1}}\right) + \partial_z\left(\frac{\bar{q_4}}{\bar{q_1}}\right)\right]\right] + \epsilon\bar{\mu}\left[\frac{4}{3}\left(\partial_y\left(\frac{q_3}{q_1}\right)\right)'\right. \\ &\left. - \frac{2}{3}\left[\left(\partial_x\left(\frac{q_2}{q_1}\right)\right)' + \left(\partial_z\left(\frac{q_4}{q_1}\right)\right)'\right]\right] + \epsilon\mu'\left[\frac{4}{3}\partial_y\left(\frac{\bar{q_3}}{\bar{q_1}}\right) + \frac{4}{3}\epsilon\left(\partial_y\left(\frac{q_3}{q_1}\right)\right)'\right. \\ &\left. - \frac{2}{3}\left[\partial_x\left(\frac{\bar{q_2}}{\bar{q_1}}\right) + \epsilon\left(\partial_x\left(\frac{q_2}{q_1}\right)\right)' + \partial_z\left(\frac{\bar{q_4}}{\bar{q_1}}\right) + \epsilon\left(\partial_z\left(\frac{q_4}{q_1}\right)\right)'\right]\right] \\ \approx \bar{f_{23}^v} &+ \epsilon f_{23}'^v \end{aligned} \tag{56}$$

$$\begin{aligned} f_{24}^v \approx \bar{\mu}&\left[\partial_z\left(\frac{\bar{q_3}}{\bar{q_1}}\right) + \partial_y\left(\frac{\bar{q_4}}{\bar{q_1}}\right)\right] + \epsilon\bar{\mu}\left[\left(\partial_z\left(\frac{q_3}{q_1}\right)\right)' + \left(\partial_y\left(\frac{q_4}{q_1}\right)\right)'\right] \\ &+ \epsilon\mu'\left[\partial_z\left(\frac{\bar{q_3}}{\bar{q_1}}\right) + \epsilon\left(\partial_z\left(\frac{q_3}{q_1}\right)\right)' + \partial_y\left(\frac{\bar{q_4}}{\bar{q_1}}\right) + \epsilon\left(\partial_y\left(\frac{q_4}{q_1}\right)\right)'\right] \\ \approx \bar{f_{24}^v} &+ \epsilon f_{24}'^v \end{aligned} \tag{57}$$

$$
\begin{aligned}
f_{25}^{v} &\approx (\bar{\mu}+\epsilon\mu')\left[\left(\frac{\bar{q_2}}{\bar{q_1}}+\epsilon\left(\frac{q_2}{q_1}\right)'\right)\left(\bar{\tau}_{yx}+\epsilon\tau'_{yx}\right)+\left(\frac{\bar{q_3}}{\bar{q_1}}+\epsilon\left(\frac{q_3}{q_1}\right)'\right)\left(\bar{\tau}_{yy}+\epsilon\tau'_{yy}\right)\right.\\
&\qquad\left.+\left(\frac{\bar{q_4}}{\bar{q_1}}+\epsilon\left(\frac{q_4}{q_1}\right)'\right)\left(\bar{\tau}_{yz}+\epsilon\tau'_{yz}\right)\right]+(\bar{\kappa}+\epsilon\kappa')\left[\frac{\partial\bar{T}}{\partial y}+\epsilon\left(\frac{\partial T}{\partial y}\right)'\right]\\
&\approx \left[\bar{\mu}\left(\frac{\bar{q_2}}{\bar{q_1}}\bar{\tau}_{yx}+\frac{\bar{q_3}}{\bar{q_1}}\bar{\tau}_{yy}+\frac{\bar{q_4}}{\bar{q_1}}\bar{\tau}_{yz}\right)+\bar{\kappa}\frac{\partial\bar{T}}{\partial x}\right]+\epsilon\left[(\bar{\mu}+\epsilon\mu')\left[\left(\frac{q_2}{q_1}\right)'\bar{\tau}_{yx}\right.\right.\\
&\qquad+\left(\frac{\bar{q_2}}{\bar{q_1}}+\epsilon\left(\frac{q_2}{q_1}\right)'\right)\tau'_{yx}+\left(\frac{q_3}{q_1}\right)'\bar{\tau}_{yy}+\left(\frac{\bar{q_3}}{\bar{q_1}}+\epsilon\left(\frac{q_3}{q_1}\right)'\right)\tau'_{yy}\\
&\qquad\left.+\left(\frac{q_4}{q_1}\right)'\bar{\tau}_{yz}+\left(\frac{\bar{q_4}}{\bar{q_1}}+\epsilon\left(\frac{q_4}{q_1}\right)'\right)\tau'_{yz}\right]\\
&\qquad+\mu'\left[\left(\frac{\bar{q_2}}{\bar{q_1}}+\epsilon\left(\frac{q_2}{q_1}\right)'\right)\left(\bar{\tau}_{yx}+\epsilon\tau'_{yx}\right)+\left(\frac{\bar{q_3}}{\bar{q_1}}+\epsilon\left(\frac{q_3}{q_1}\right)'\right)\left(\bar{\tau}_{yy}+\epsilon\tau'_{yy}\right)\right.\\
&\qquad\left.\left.+\left(\frac{\bar{q_4}}{\bar{q_1}}+\epsilon\left(\frac{q_4}{q_1}\right)'\right)\left(\bar{\tau}_{yz}+\epsilon\tau'_{yz}\right)\right]+\bar{\kappa}\left(\frac{\partial T}{\partial y}\right)'+\kappa'\left(\frac{\partial\bar{T}}{\partial y}+\epsilon\left(\frac{\partial T}{\partial y}\right)'\right)\right]\\
&\approx \bar{f_{25}^{v}}+\epsilon f_{25}^{\prime v}
\end{aligned}
\tag{58}
$$

- z-direction

$$
f_{31}^{v}=0 \tag{59}
$$

$$
\begin{aligned}
f_{32}^{v} &= f_{14}^{v}\\
&\approx \bar{f_{14}^{v}}+\epsilon f_{14}^{\prime v}\\
&\approx \bar{f_{32}^{v}}+\epsilon f_{32}^{\prime v}
\end{aligned}
\tag{60}
$$

$$
\begin{aligned}
f_{33}^{v} &= f_{24}^{v}\\
&\approx \bar{f_{24}^{v}}+\epsilon f_{24}^{\prime v}\\
&\approx \bar{f_{33}^{v}}+\epsilon f_{33}^{\prime v}
\end{aligned}
\tag{61}
$$

$$
\begin{aligned}
f_{34}^{v} \approx\ & (\bar{\mu}+\epsilon\mu')\left[\frac{4}{3}\partial_z\left(\frac{\bar{q_4}}{\bar{q_1}}\right)+\frac{4}{3}\epsilon\left(\partial_z\left(\frac{q_4}{q_1}\right)\right)'-\frac{2}{3}\left[\partial_x\left(\frac{\bar{q_2}}{\bar{q_1}}\right)+\epsilon\left(\partial_x\left(\frac{q_2}{q_1}\right)\right)'\right.\right.\\
&\left.\left.+\partial_y\left(\frac{\bar{q_3}}{\bar{q_1}}\right)+\epsilon\left(\partial_y\left(\frac{q_3}{q_1}\right)\right)'\right]\right]\\
\approx\ & \bar{\mu}\left[\frac{4}{3}\partial_z\left(\frac{\bar{q_4}}{\bar{q_1}}\right)-\frac{2}{3}\left[\partial_x\left(\frac{\bar{q_2}}{\bar{q_1}}\right)+\partial_y\left(\frac{\bar{q_3}}{\bar{q_1}}\right)\right]\right]+\epsilon\bar{\mu}\left[\frac{4}{3}\left(\partial_z\left(\frac{q_4}{q_1}\right)\right)'\right.\\
&\left.-\frac{2}{3}\left[\left(\partial_x\left(\frac{q_2}{q_1}\right)\right)'+\left(\partial_y\left(\frac{q_3}{q_1}\right)\right)'\right]\right]+\epsilon\mu'\left[\frac{4}{3}\partial_z\left(\frac{\bar{q_4}}{\bar{q_1}}\right)+\frac{4}{3}\epsilon\left(\partial_z\left(\frac{q_4}{q_1}\right)\right)'\right.\\
&\left.-\frac{2}{3}\left[\partial_x\left(\frac{\bar{q_2}}{\bar{q_1}}\right)+\epsilon\left(\partial_x\left(\frac{q_2}{q_1}\right)\right)'+\partial_y\left(\frac{\bar{q_3}}{\bar{q_1}}\right)+\epsilon\left(\partial_y\left(\frac{q_3}{q_1}\right)\right)'\right]\right]\\
\approx\ & \bar{f_{34}^{v}}+\epsilon f_{34}^{\prime v}
\end{aligned}
\tag{62}
$$

$$
\begin{aligned}
f_{35}^{v} \approx\ & (\bar{\mu}+\epsilon\mu')\left[\left(\frac{\bar{q_2}}{\bar{q_1}}+\epsilon\left(\frac{q_2}{q_1}\right)'\right)(\bar{\tau}_{zx}+\epsilon\tau'_{zx})+\left(\frac{\bar{q_3}}{\bar{q_1}}+\epsilon\left(\frac{q_3}{q_1}\right)'\right)\left(\bar{\tau}_{zy}+\epsilon\tau'_{zy}\right)\right.\\
&\left.+\left(\frac{\bar{q_4}}{\bar{q_1}}+\epsilon\left(\frac{q_4}{q_1}\right)'\right)(\bar{\tau}_{zz}+\epsilon\tau'_{zz})\right]+(\bar{\kappa}+\epsilon\kappa')\left[\frac{\partial\bar{T}}{\partial z}+\epsilon\left(\frac{\partial T}{\partial z}\right)'\right]\\
\approx\ & \left[\bar{\mu}\left(\frac{\bar{q_2}}{\bar{q_1}}\bar{\tau}_{zx}+\frac{\bar{q_3}}{\bar{q_1}}\bar{\tau}_{zy}+\frac{\bar{q_4}}{\bar{q_1}}\bar{\tau}_{zz}\right)+\bar{\kappa}\frac{\partial\bar{T}}{\partial x}\right]+\epsilon\left[(\bar{\mu}+\epsilon\mu')\left[\left(\frac{q_2}{q_1}\right)'\bar{\tau}_{zx}\right.\right.\\
&+\left(\frac{\bar{q_2}}{\bar{q_1}}+\epsilon\left(\frac{q_2}{q_1}\right)'\right)\tau'_{zx}+\left(\frac{q_3}{q_1}\right)'\bar{\tau}_{zy}+\left(\frac{\bar{q_3}}{\bar{q_1}}+\epsilon\left(\frac{q_3}{q_1}\right)'\right)\tau'_{zy}\\
&\left.+\left(\frac{q_4}{q_1}\right)'\bar{\tau}_{zz}+\left(\frac{\bar{q_4}}{\bar{q_1}}+\epsilon\left(\frac{q_4}{q_1}\right)'\right)\tau'_{zz}\right]\\
&+\mu'\left[\left(\frac{\bar{q_2}}{\bar{q_1}}+\epsilon\left(\frac{q_2}{q_1}\right)'\right)(\bar{\tau}_{zx}+\epsilon\tau'_{zx})+\left(\frac{\bar{q_3}}{\bar{q_1}}+\epsilon\left(\frac{q_3}{q_1}\right)'\right)\left(\bar{\tau}_{zy}+\epsilon\tau'_{zy}\right)\right.\\
&\left.\left.+\left(\frac{\bar{q_4}}{\bar{q_1}}+\epsilon\left(\frac{q_4}{q_1}\right)'\right)(\bar{\tau}_{zz}+\epsilon\tau'_{zz})\right]+\bar{\kappa}\left(\frac{\partial T}{\partial z}\right)'+\kappa'\left(\frac{\partial\bar{T}}{\partial z}+\epsilon\left(\frac{\partial T}{\partial z}\right)'\right)\right]\\
\approx\ & \bar{f_{35}^{v}}+\epsilon f_{35}^{\prime v}
\end{aligned}
\tag{63}
$$

This page is intentionally left blank

C. Empirical Filter Bandwidth

Algorithm 4 Empirical bandwidth

INITIALIZE ($N \leftarrow length(\omega), \{\omega_{left}\} \leftarrow \omega_{max}, \{\omega_{right}\} \leftarrow 0, r_{tonal}, i_{old} \leftarrow 1, n$)

Compute $\{\hat{X}\} \leftarrow |\text{FFT}(\{X\})|_{one-sided}$
Extract local maxima $\{\hat{X}_{loc}\}$ and its index location $\{i_{loc}\}$ within $\omega[i-n:i+n]$ from the spectrum $\{\hat{X}\}$
Remove false maxima in broadband peaks
For consecutive maxima with $R > r_{tonal}$, add minima:
for $i = 1 : length(\hat{X}_{loc}) - 1$ **do**
  $R \leftarrow \frac{max(\hat{X}_{loc}[i], \hat{X}_{loc}[i+1])}{min(\hat{X}_{loc}[i], \hat{X}_{loc}[i+1])}$
  if $R > r_{tonal}$ **then**
    if any ($\hat{X}_{loc}[i]$ **or** $\hat{X}_{loc}[i+1]$) is narrowband **then**
      $\hat{X}_{loc} \leftarrow \hat{X}_{loc} \cup \hat{X}[i_{loc}[i]+1]$ and / or $\hat{X}_{loc} \leftarrow \hat{X}_{loc} \cup \hat{X}[i_{loc}[i+1]-1]$ with index in i_{loc}
    else
      $\hat{X}_{loc} \leftarrow \hat{X}_{loc} \cup \min\left(\hat{X}[i_{loc}[i]+1 : i_{loc}[i+1]-1]\right)$ with index in i_{loc}
    end if
  end if
end for
SORT $\{\hat{X}_{loc}\}$ and i_{loc} by index location i_{loc}

UPDATE $\{\omega_{left}\}$ and $\{\omega_{right}\}$:
for $i = 1 : length(\hat{X}_{loc})$ **do**
  if $\hat{X}_{loc}[i]$ is a maxima **and** $i_{loc}[i] > i_{old}$ **then**
    for $j = i+1 : length(\hat{X}_{loc})$ **do**
      $R \leftarrow \frac{\hat{X}_{loc}[i]}{\hat{X}_{loc}[j]}$
      if $R < 1$ **then**
        break
      else if $R > r_{tonal}$ **then**
        $i_{new} \leftarrow i_{loc}[j]$
        $\omega_{right}[i_{old} : i_{new} - 1] \leftarrow \omega[i_{new}]$
        $i_{old} \leftarrow i_{new}$
        break
      end if

end for
for $j = max(i-1, 1) : -1 : 1$ **do**
$R \leftarrow \frac{\hat{X}_{loc}[i]}{\hat{X}_{loc}[j]}$
if $R < 1$ **then**
break
else if $R > r_{tonal}$ **then**
$i_{new} \leftarrow i_{loc}[j]$
$\omega_{left}[min(i_{new}, N) : N] \leftarrow \omega[i_{new}]$
break
end if
end for
end if
end for
COMPUTE $\{\omega_{band}\}$:
$\omega_{band} \leftarrow \frac{1}{2\ min(|\omega_{\hat{X}} - \omega_{down}|, |\omega_{\hat{X}} - \omega_{up}|) \times (\omega_{\hat{X}}(2) - \omega_{\hat{X}}(1))}$

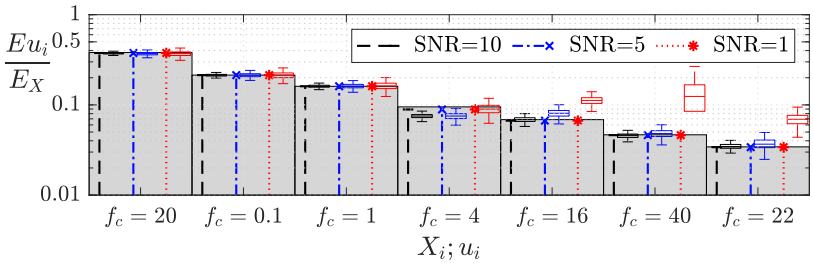

(a) noise level SNR

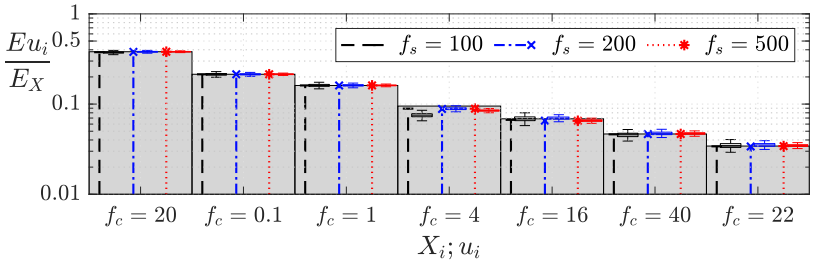

(b) sampling frequency f_s

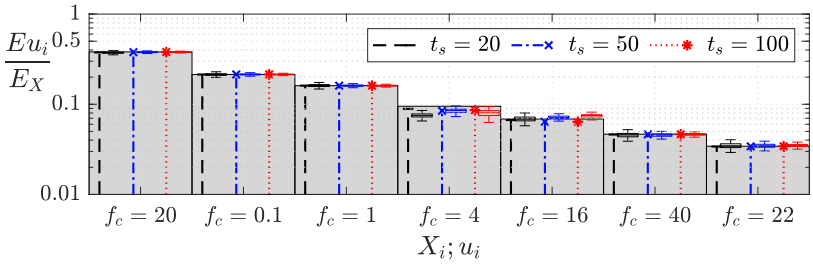

(c) sampling time t_s

Figure 1: Energy sensitivity of POVMD modes with different level of noise, sampling frequency, and sampling time; without (vertical lines) and with noise (boxplot)

D. Simulations considering the NASA hump

To demonstrate the generality of the physical phenomena with respect to other wall-bounded bump geometries, an analogous study is conducted on a wall-mounted modified Glauert hump model (Greenblatt, Paschal, Yao, Harris, et al., 2006; Seifert and Pack, 2002), often referred to in the literature as the NASA hump. The setup of the simulation is shown in Fig. 2. The domain of the simulation is $(13 \times 0.909 \times 0.5)$ m in the longitudinal, normal, and spanwise directions, respectively. A scaling of the hump geometry allows the reference chord length of the model, L_{Ref} to be unity. The ratio of the hump height to the channel height is identical to Greenblatt, Paschal, Yao, Harris, et al., 2006, which is 0.1407. The domain is discretized into 77,616 high-order elements and simulated with 3^{rd}-order polynomial (4,967,424 DOFs). The fringe region starts from $x_{start} = 3$ m with $\Delta_{rise} = 2$ m and $\overline{\lambda} = 400$.

The boundary conditions of the domain are nearly identical to the aforementioned study but a free-slip condition is imposed at the upper boundary. In the harmonic inflow cases, the total pressure variation with time follows Eq.(6.1), with $p_{t,steady} = 102143$ Pa. Simulations are conducted with the inflow air density $\rho = 1.184$ kg/m^3, and the dynamic viscosity $\mu = 1.366 \times 10^{-3}$ Pa.s. In these conditions, the flow has a characteristic Reynolds $Re = 30,000$ and Mach 0.1 at the inlet for the steady inflow. The Reynolds number based on the maximum height of the recirculation region and respectively the length of the separated region are $Re_h \approx 3840$ and $Re_{L_s} = 37380$. These numbers are comparable with those of the simulations presented in the paper. The Reynolds number based on the boundary layer momentum thickness at the separation point is $Re_{\theta_s} = 171$. Based on the proposed scaling on Hasan, 1992 and Sigurdson, 1995, the natural frequency of shedding of the KH vortices is $f^*_{KH} \approx 2.1$ and the vortex cluster shedding frequency is $f^*_{shed} \approx 0.6 - 0.7$.

Table 1 summarizes the cases simulated, showing the harmonic inflow parameters, the mean and oscillation amplitude of the streamwise velocity at a reference point, $(x, y, z) = (0, 0.9, 0.25)$ m, the time-averaged length of the separated flow region and its reduction with respect to the steady inflow. The instantaneous spanwise vorticity for the harmonic inflow cases ($A_{in} = 0.005$, $f^*_{in} = 0.25$) and ($A_{in} = 0.05$, $f^*_{in} = 0.5$) are presented in Figs. 3 and 4, respectively. The first case recovers scenario (i), dominated by KH vortices, while the second one shows the phased-locked formation and release of the vortex cluster, characteristic of scenario (iii). The classification of the cases for the NASA hump geometry is given in Table 2 along with the minimum value of the acceleration parameter components computed at the wall-normal

coordinate $y = 2.778h$. This coordinate is the same used for the computation of K in Section 6.3.

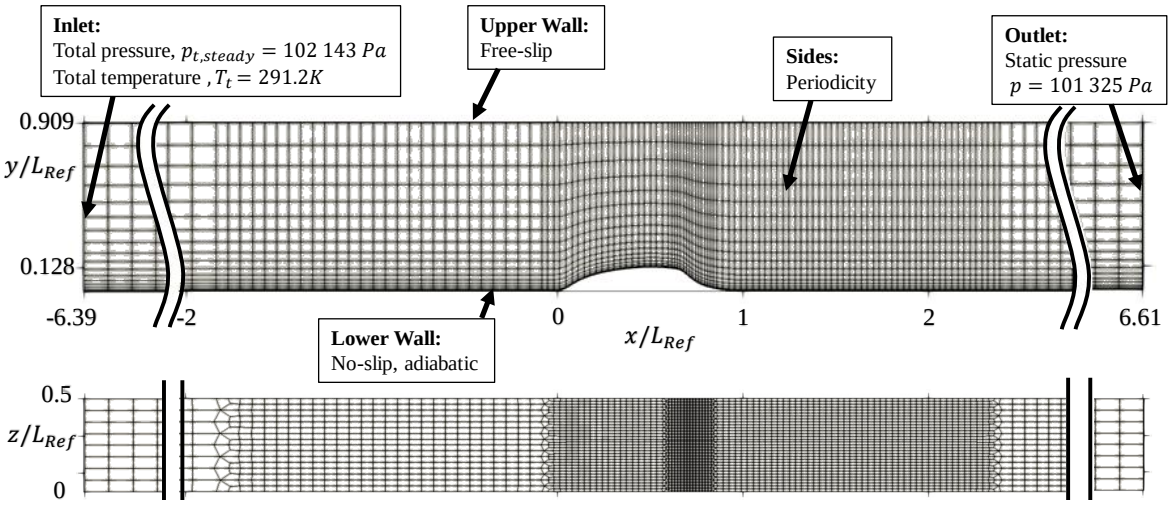

Figure 2: Computational domain, representative mesh, and boundary conditions for NASA Hump cases .

Table 1: Summary of the cases simulated for the NASA hump, including the definition of the inlet pressure condition and the characterization of time-averaged and phase-dependent values of the reference streamwise velocity and the length of the recirculation region L_s.

t^*_{data}	A_{in}	f^*_{in}	$\bar{u}^*_{@Ref}$	$\Delta u^*_{@Ref}$	L_s [m]	ΔL_s [m]
27	-	-	1.0958	-	1.2460	-
16	0.005	0.25	1.0974	0.0339	1.2284	-0.0176
16	0.005	0.5	1.0967	0.0348	1.0012	-0.2448
16	0.025	0.25	1.0953	0.1699	0.8610	-0.3850
12	0.025	0.5	1.0932	0.1744	0.4531	-0.7929
12	0.05	0.5	1.0887	0.3498	0.4079	-0.8381

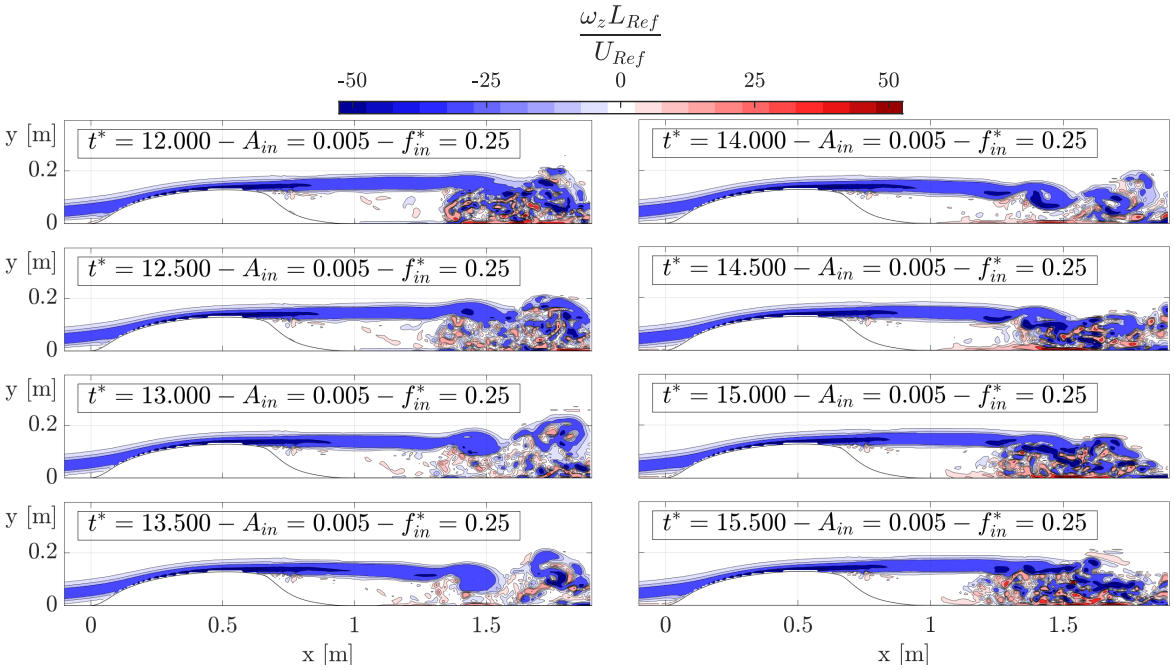

Figure 3: Instantaneous spanwise vorticity for the NASA hump. $A_{in} = 0.005$ and $f^*_{in} = 0.25$.

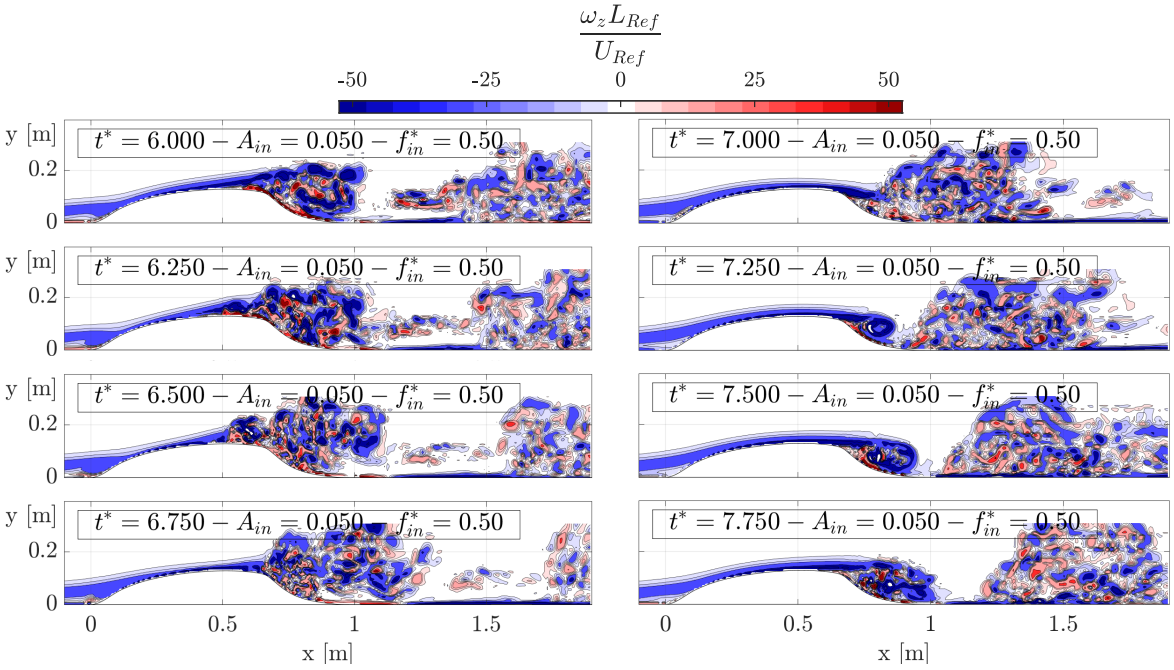

Figure 4: Instantaneous spanwise vorticity for the NASA hump. $A_{in} = 0.05$ and $f^*_{in} = 0.5$.

Table 2: Classification of the cases for the NASA hump geometry. Minimum values of the time-averaged and phase-averaged streamwise acceleration parameter. The first row corresponds to the steady inflow case

A_{in}	f^*_{in}	$A_{in}f^*_{in}$	$\overline{K}_{min}$ $\times 10^{-6}$	$< K >_{min}$ $\times 10^{-6}$	$< K_{\partial u/\partial x} >_{min}$ $\times 10^{-6}$	$< K_{\partial u/\partial t} >_{min}$ $\times 10^{-6}$	Scenario
-	-	-	-6.05	-6.05	-6.05	-	(i)
0.005	0.25	0.00125	-6.78	-15.24	-15.28	-0.18	(i)
0.005	0.5	0.0025	-8.51	-19.61	-19.85	-0.27	(ii)
0.025	0.25	0.00625	-9.15	-20.53	-20.40	-0.28	(ii)
0.025	0.5	0.0125	-10.02	-24.48	-25.29	-3.66	(ii)
0.05	0.5	0.025	-16.70	-42.77	-43.74	-8.33	(iii)

E. Appendix to 2D Synthetic Jet Results

E.1. Shedding mode: laminar and turbulent inflow - without control

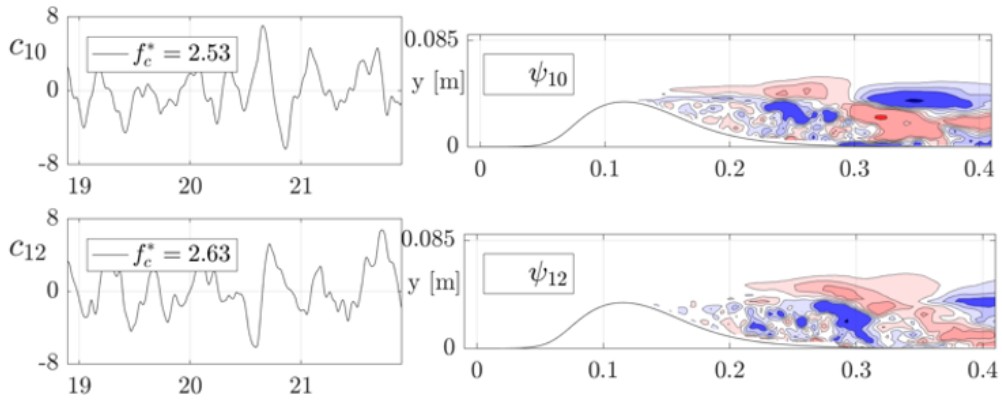

Figure 5: OVMD modes correspond to the shedding mode - Bump with laminar inflow without control - decompose with instantaneous data

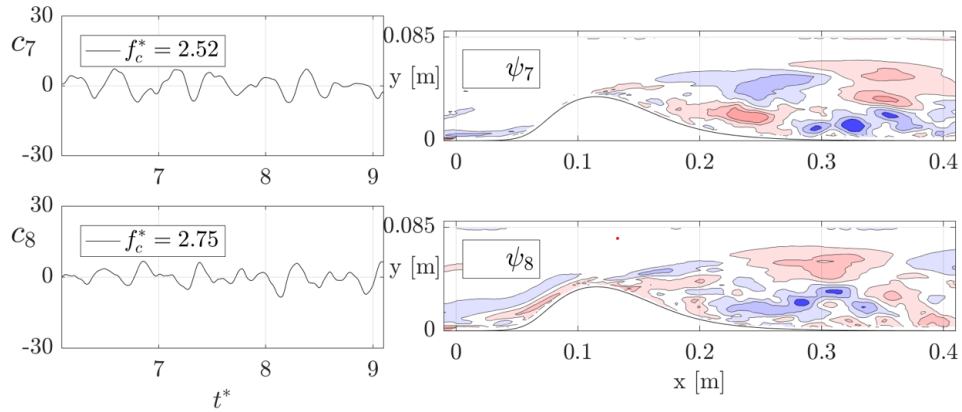

Figure 6: OVMD modes correspond to the shedding mode - Bump with turbulent inflow without control - decomposewith instantaneous data

E.2. Instantaneous flow field: turbulent inflow

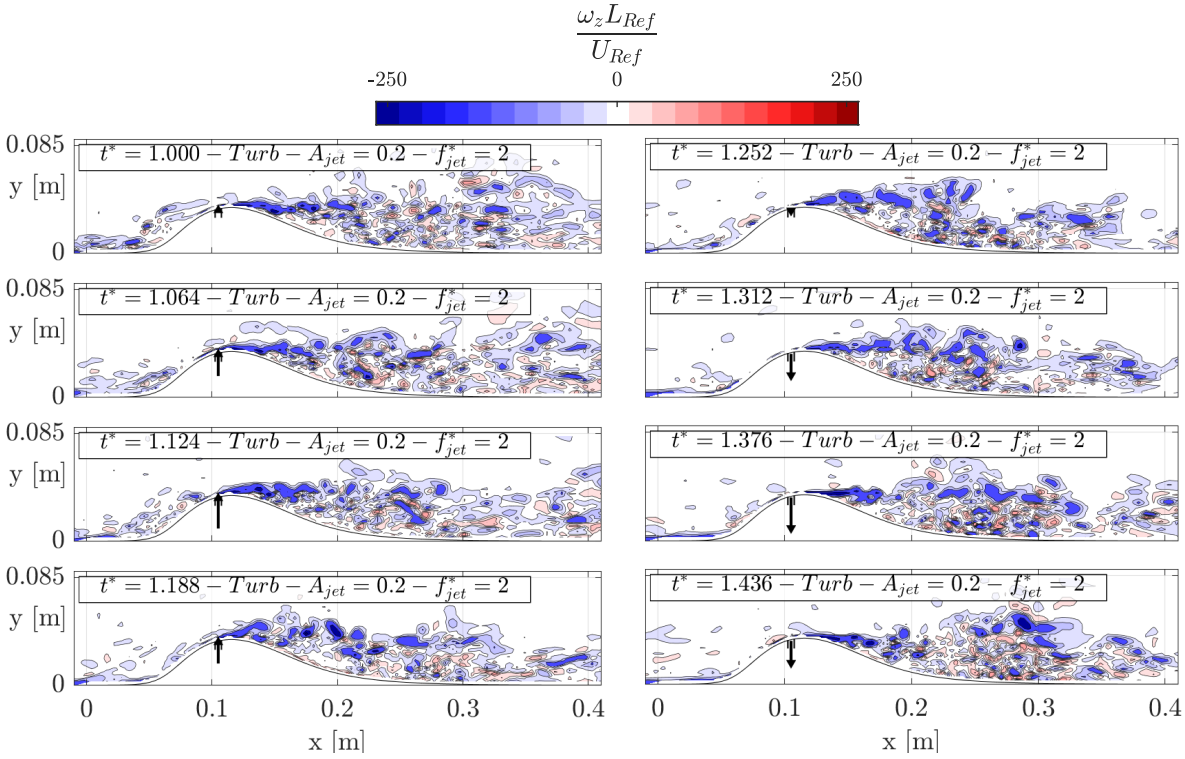

Figure 7: Instantaneous spanwise vorticity. Turbulent boundary layer, $A_{jet} = 0.2 - f^*_{jet} = 2$

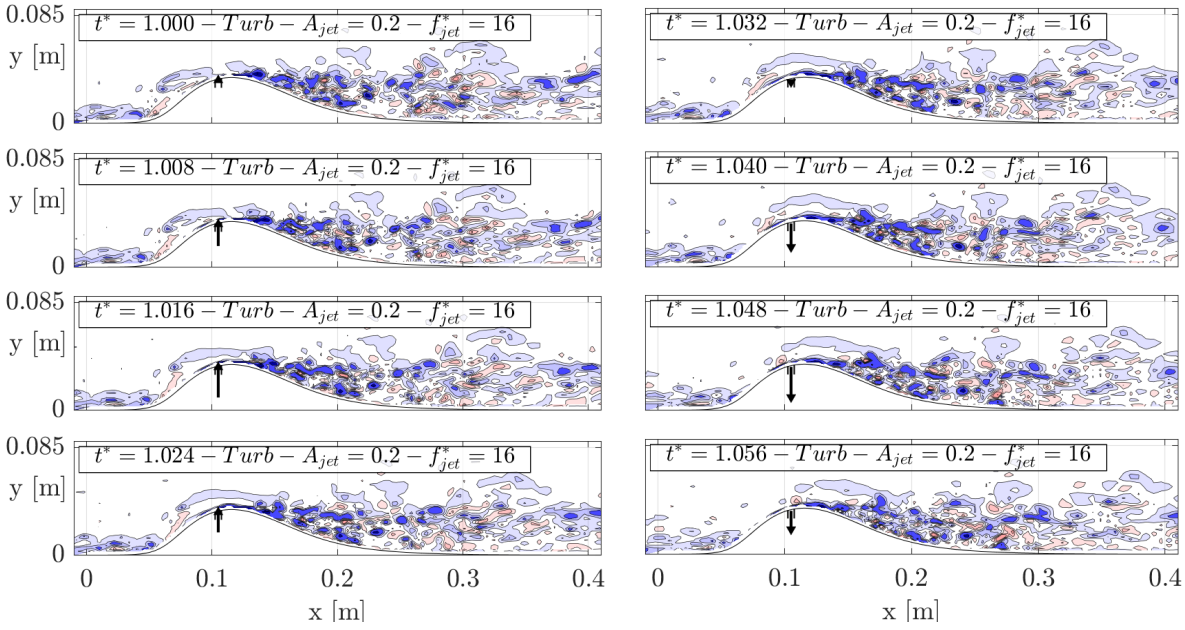

Figure 8: Instantaneous spanwise vorticity. Turbulent boundary layer, $A_{jet} = 0.2 - f^*_{jet} = 16$

E.3. Mode Decomposition: turbulent inflow with actuation Strategy I

In this section, the corresponding OVMD modes in the control case with Strategy I and with turbulent inflow are presented. The decompositions were performed using instantaneous flow field data as input.

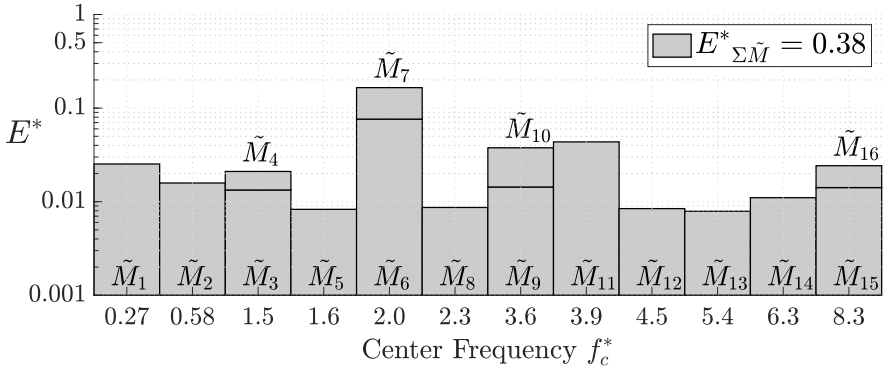

Figure 9: Energy ratio of modes - turbulent - $A_{jet} = 0.2 - f^*_{jet} = 2$

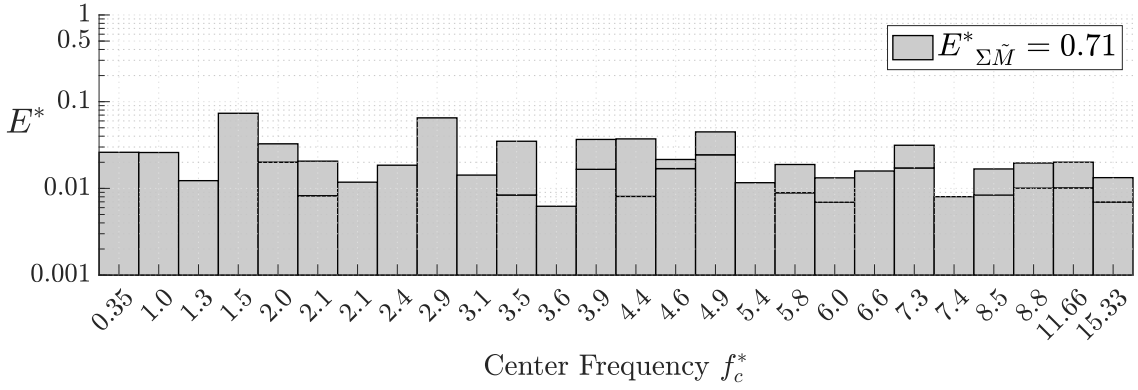

Figure 10: Energy ratio of modes - turbulent - $A_{jet} = 0.2 - f^*_{jet} = 16$

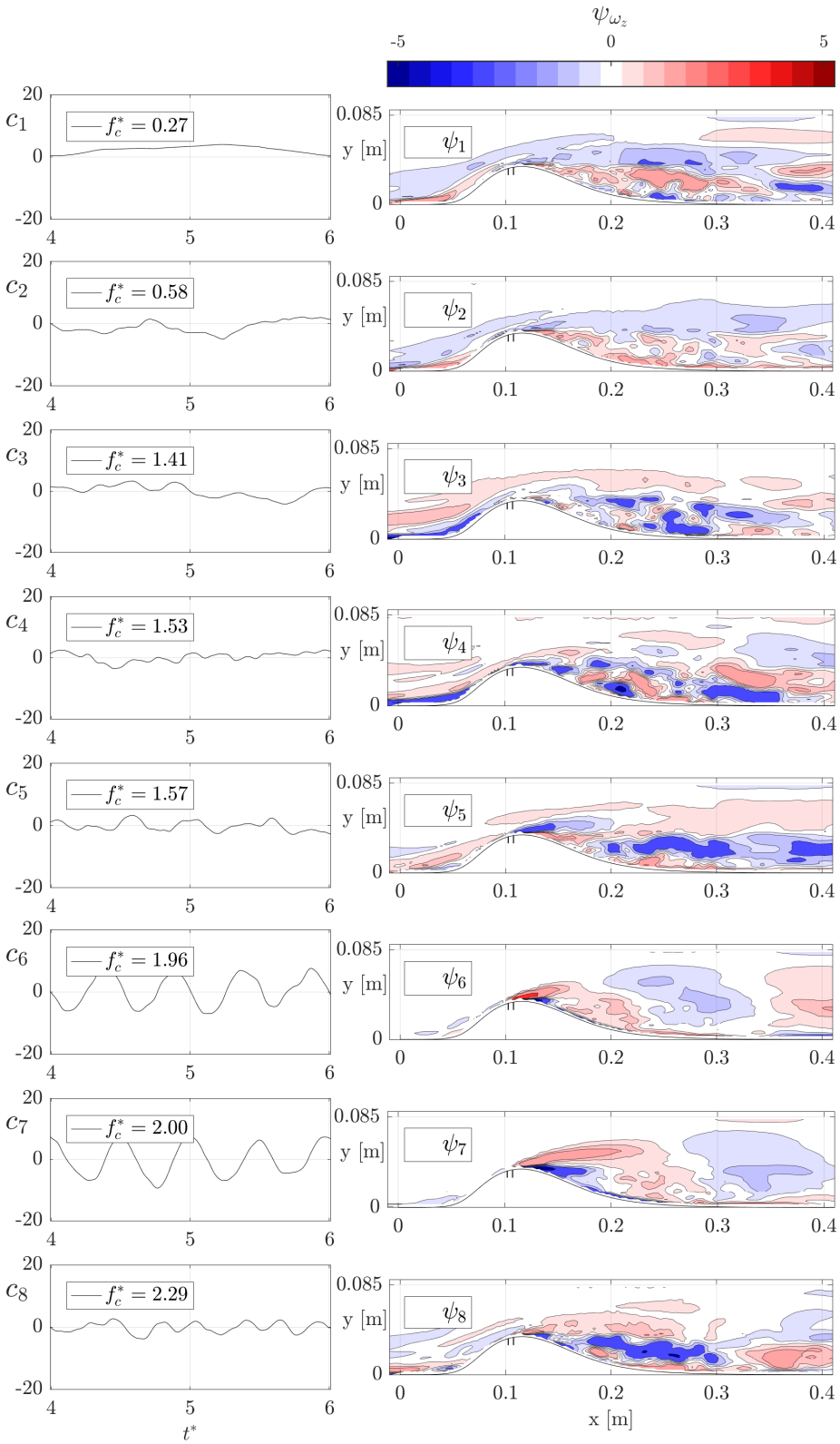

Figure 11: OVMD modes 1-8, represented by spanwise vorticity, for the Bump with turbulent boundary layer and $A_{jet} = 0.2 - f^*_{jet} = 2$

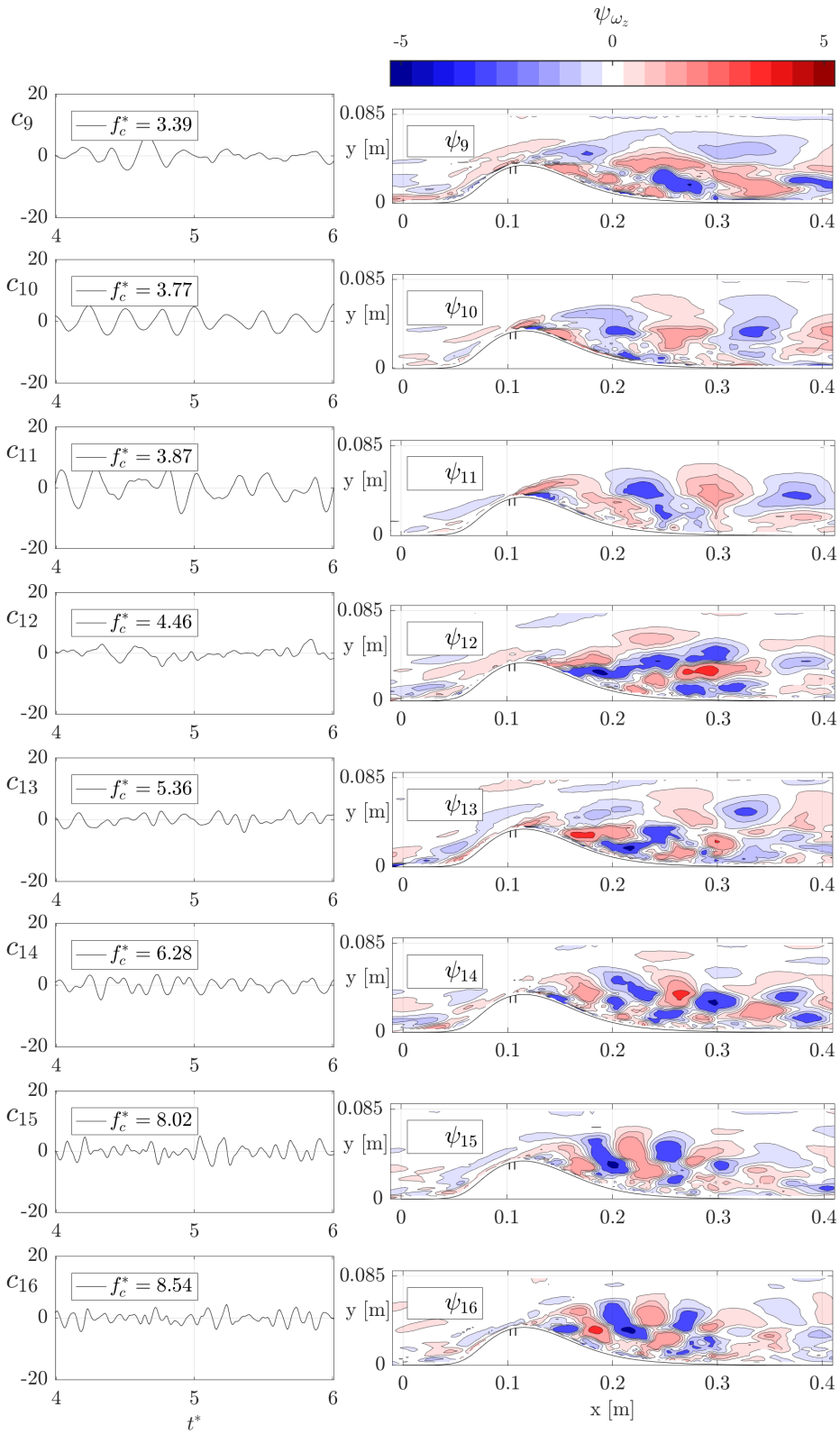

Figure 12: OVMD modes 9-16, represented by spanwise vorticity, for the Bump with turbulent boundary layer and $A_{jet} = 0.2 - f^*_{jet} = 2$

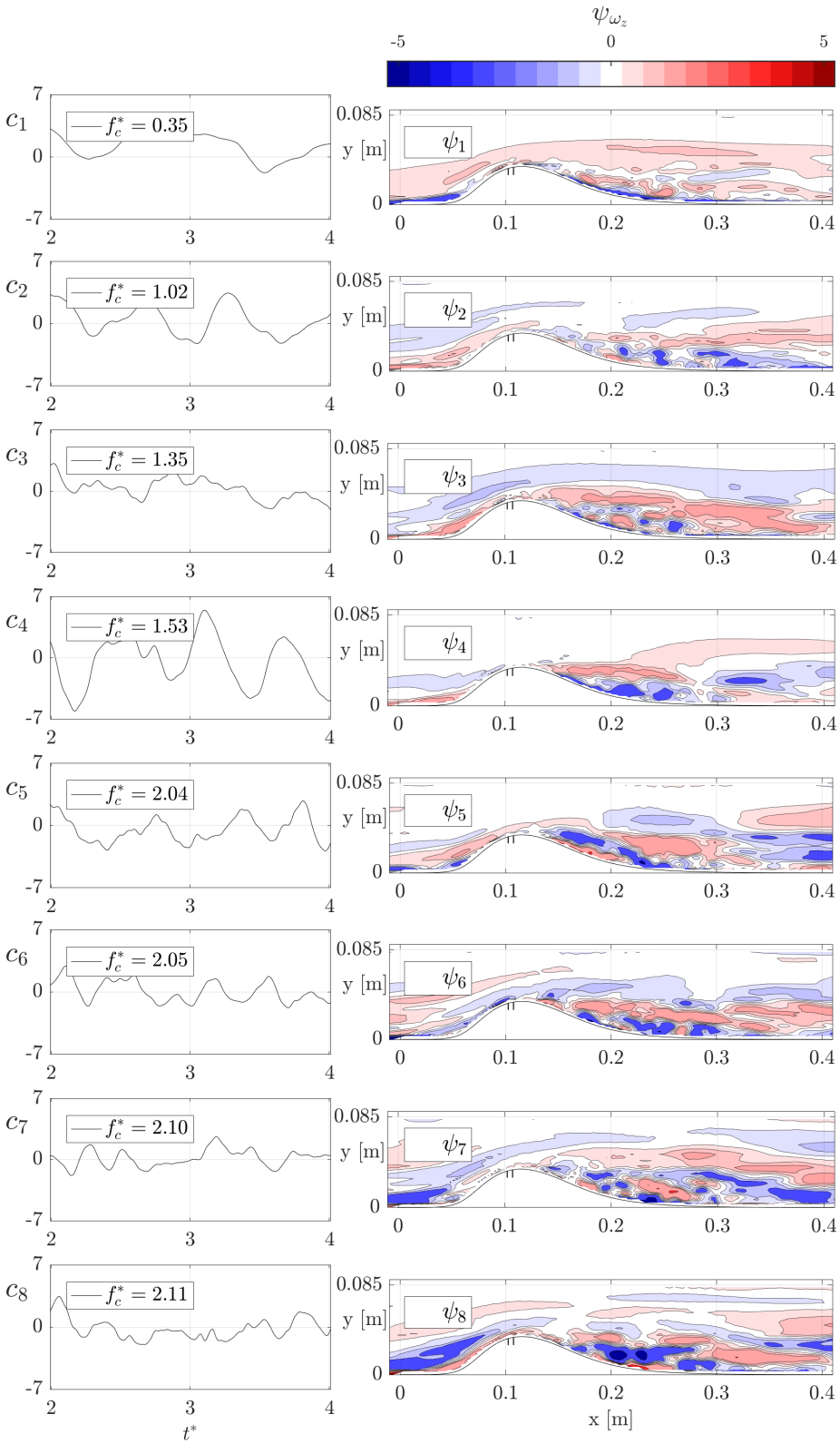

Figure 13: OVMD modes 1-8, represented by spanwise vorticity, for the Bump with turbulent boundary layer and $A_{jet} = 0.2 - f^*_{jet} = 16$

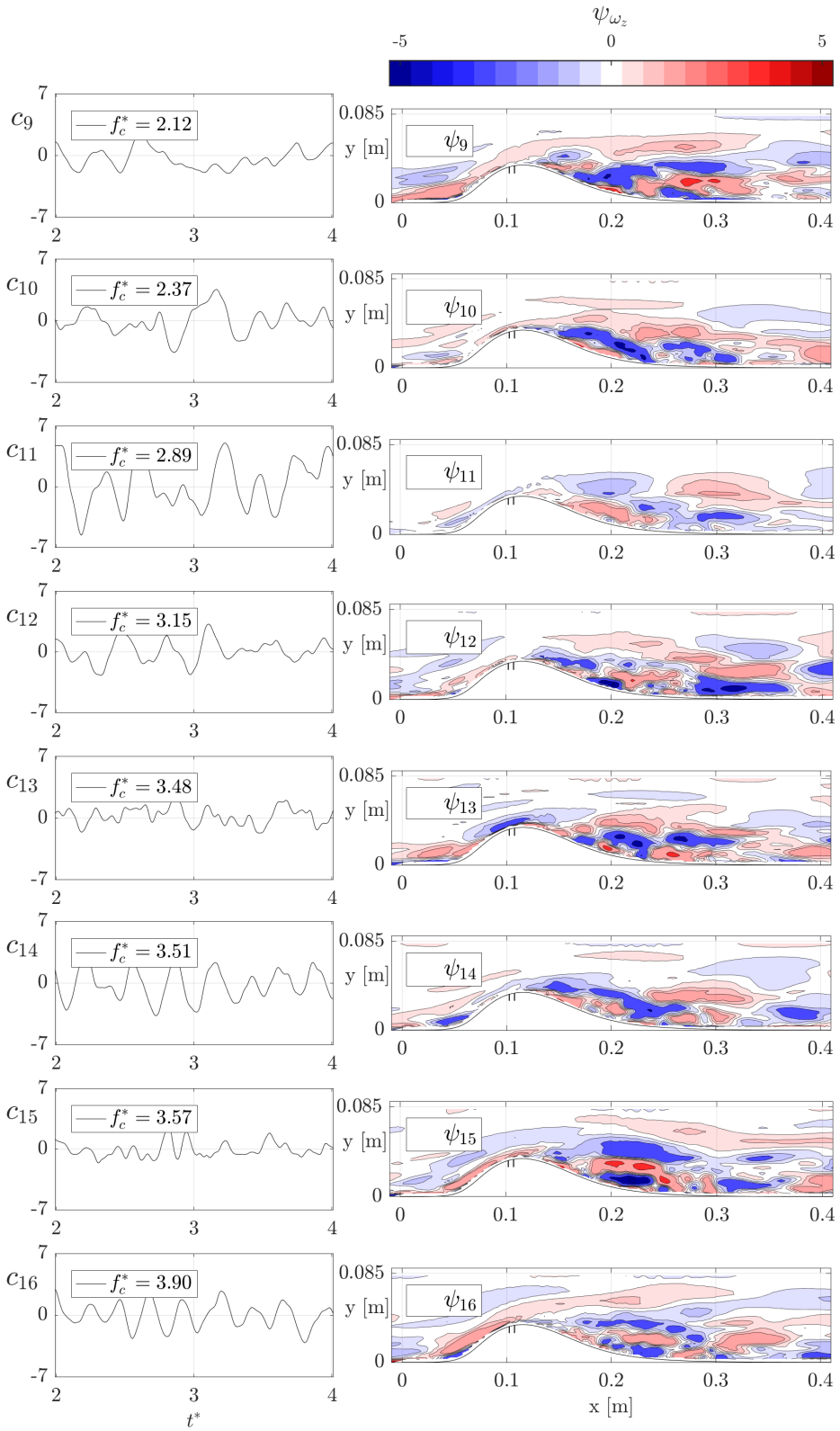

Figure 14: OVMD modes 9-16, represented by spanwise vorticity, for the Bump with turbulent boundary layer and $A_{jet} = 0.2 - f^*_{jet} = 16$

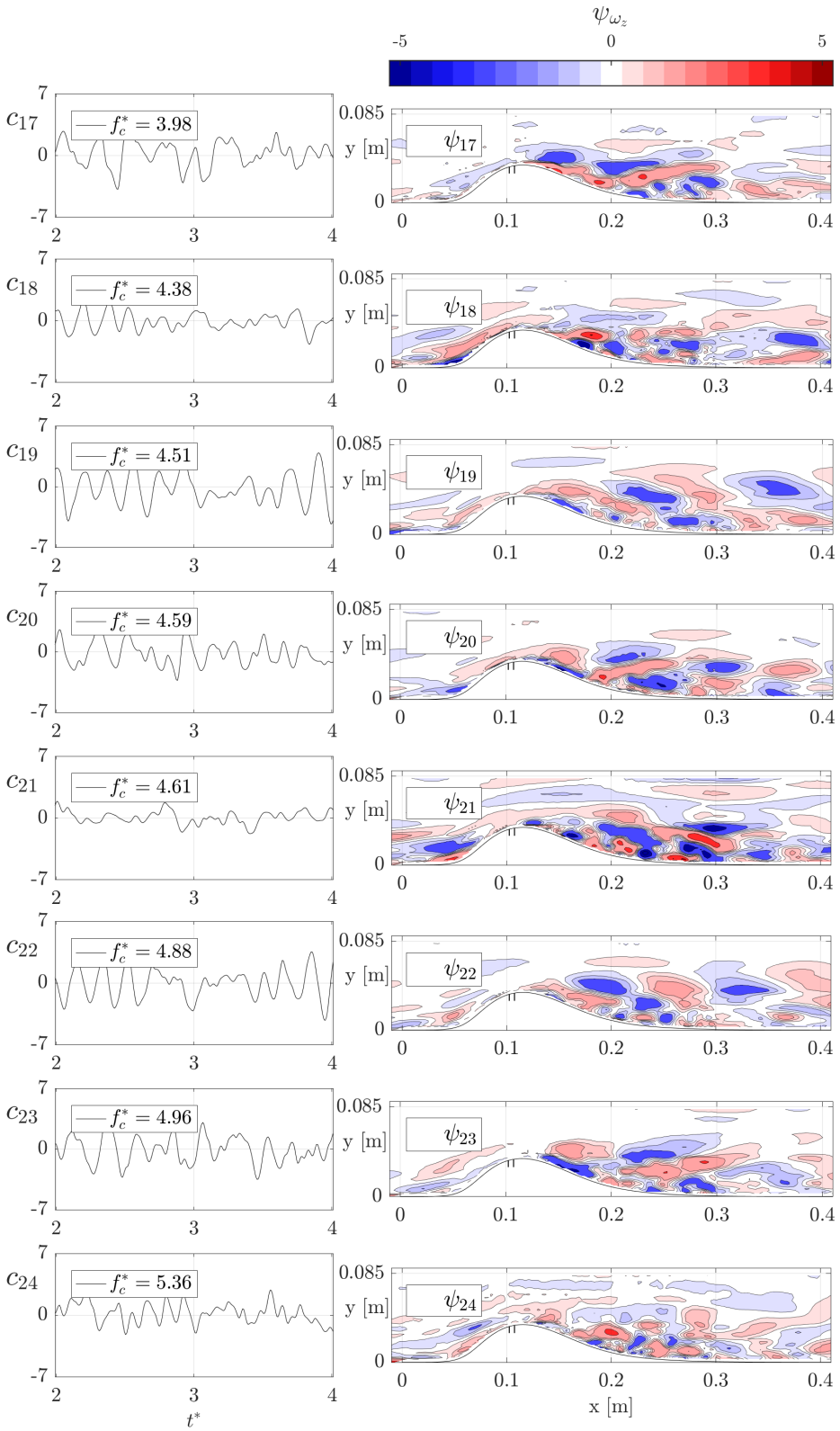

Figure 15: OVMD modes 17-24, represented by spanwise vorticity, for the Bump with turbulent boundary layer and $A_{jet} = 0.2 - f^*_{jet} = 16$

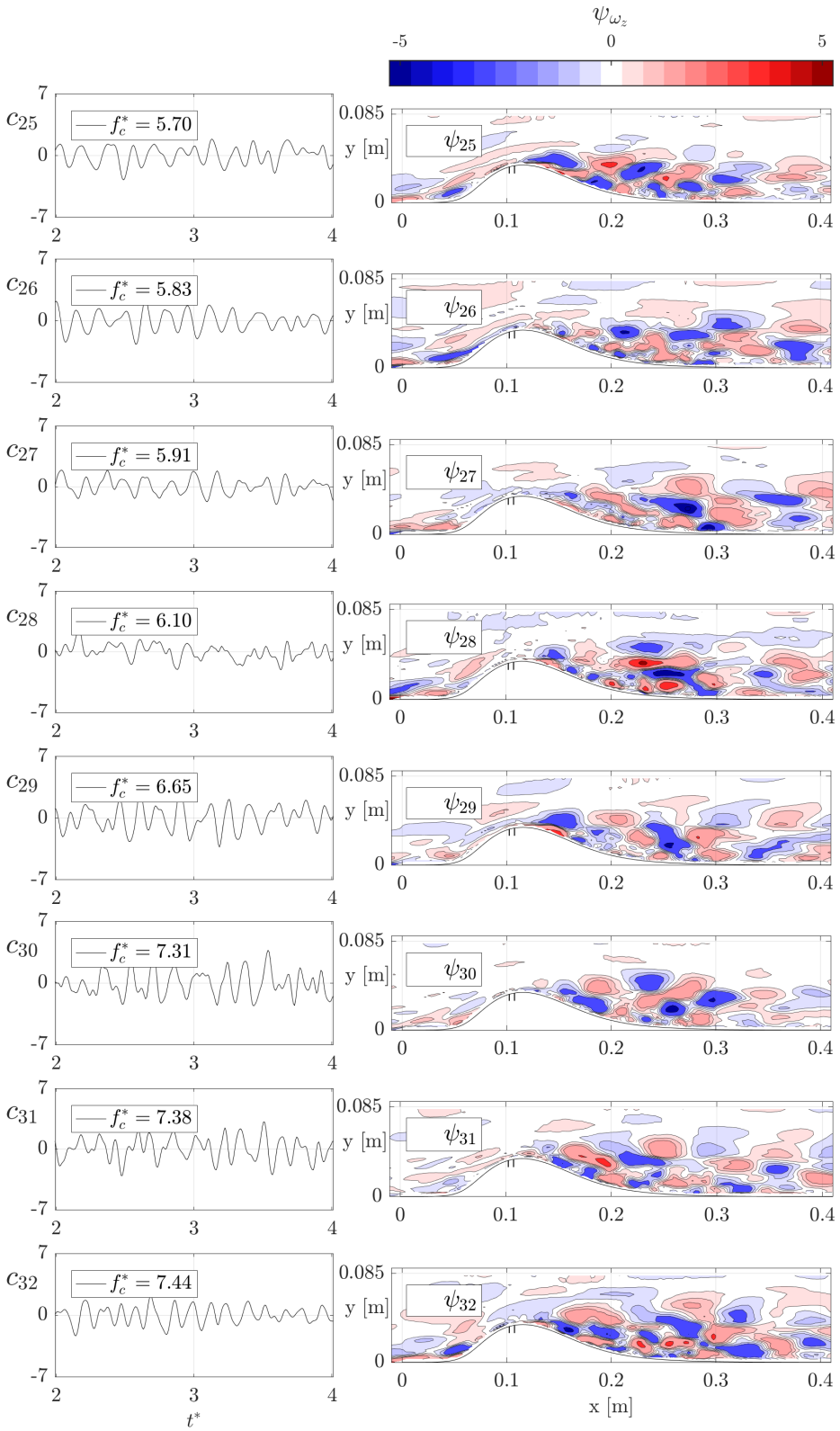

Figure 16: OVMD modes 25-32, represented by spanwise vorticity, for the Bump with turbulent boundary layer and $A_{jet} = 0.2 - f^*_{jet} = 16$

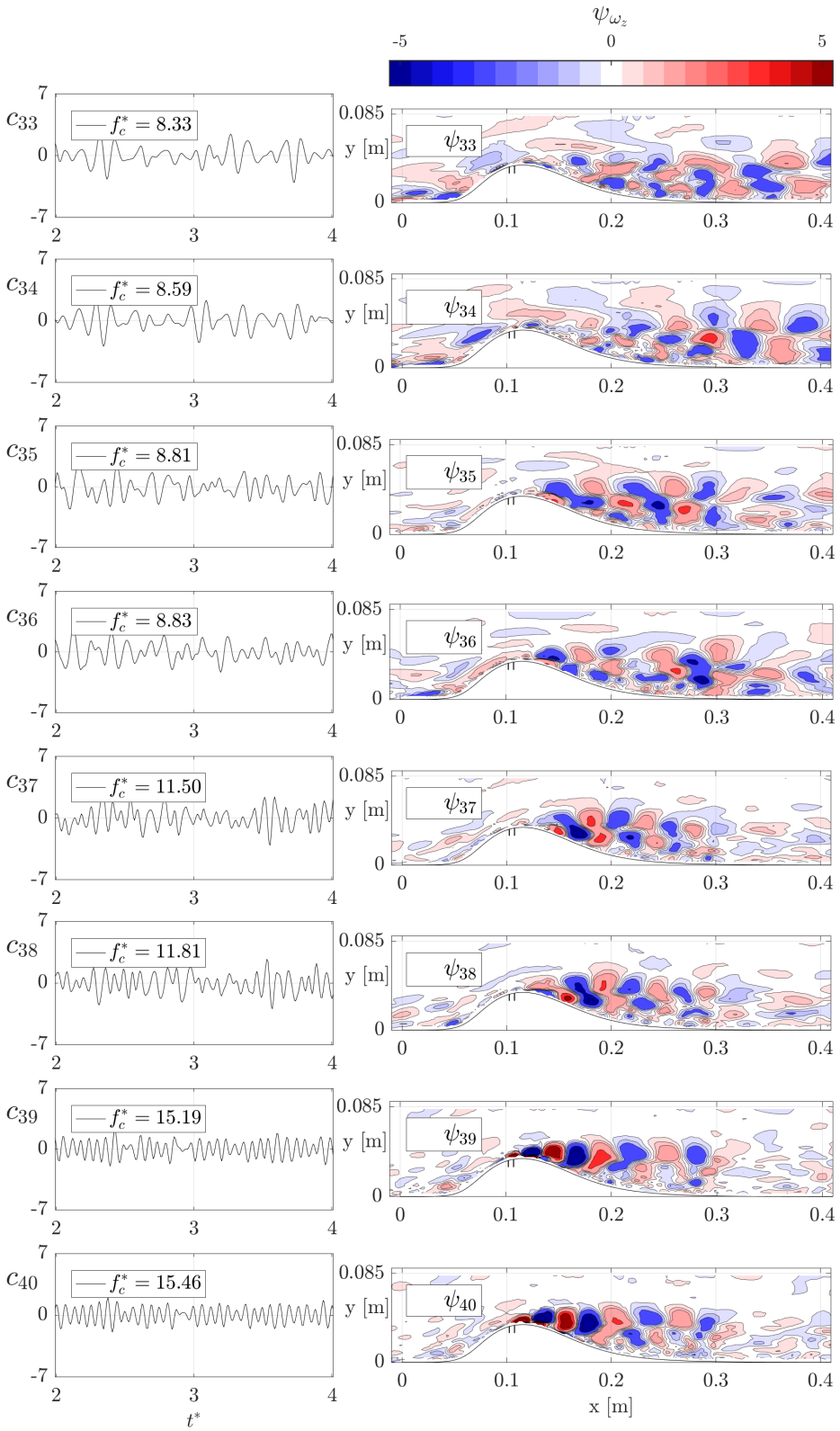

Figure 17: OVMD modes 33-40, represented by spanwise vorticity, for the Bump with turbulent boundary layer and $A_{jet} = 0.2 - f^*_{jet} = 16$

This page is intentionally left blank